

Fundamentals of Applied Electromagnetics 6e  
by  
Fawwaz T. Ulaby, Eric Michielssen, and Umberto Ravaioli

Figures

# Chapters

Chapter 1 Introduction: Waves and Phasors

Chapter 2 Transmission Lines

Chapter 3 Vector Analysis

Chapter 4 Electrostatics

Chapter 5 Magnetostatics

Chapter 6 Maxwell's Equations for Time-Varying Fields

Chapter 7 Plane-Wave Propagation

Chapter 8 Wave Reflection and Transmission

Chapter 9 Radiation and Antennas

Chapter 10 Satellite Communication Systems and Radar Sensors

## Chapter 1 Figures

Figure 1-1 2-D LCD array.

Figure 1-2 Electromagnetics is at the heart of numerous systems and applications.

Figure 1-3 Gravitational forces between two masses.

Figure 1-4 Gravitational field  $\Psi_1$  induced by a mass  $m_1$ .

Figure 1-5 Electric forces on two positive point charges in free space.

Figure 1-6 Electric field  $\mathbf{E}$  due to charge  $q$ .

Figure 1-7 Polarization of the atoms of a dielectric material by a positive charge  $q$ .

Figure 1-8 Pattern of magnetic field lines around a bar magnet.

Figure 1-9 The magnetic field induced by a steady current flowing in the  $z$ -direction.

Figure 1-10 A one-dimensional wave traveling on a string.

Figure 1-11 Examples of two-dimensional and three-dimensional waves.

Figure 1-12 Plots of  $y(x, t) = A \cos \left( \frac{2\pi t}{T} - \frac{2\pi x}{\lambda} \right)$  as a function of (a)  $x$  at  $t = 0$  and (b)  $t$  at  $x = 0$ .

Figure 1-13 Plots of  $y(x, t) = A \cos \left( \frac{2\pi t}{T} - \frac{2\pi x}{\lambda} \right)$

Figure 1-14 Plots of  $y(0, t) = A \cos \left[ \left( \frac{2\pi t}{T} \right) + \phi_0 \right]$  for three different values of the reference phase  $\phi_0$ .

Figure 1-15 Plot of  $y(x) = (10e^{-0.2x} \cos \pi x)$  meters.

Figure 1-16 The electromagnetic spectrum.

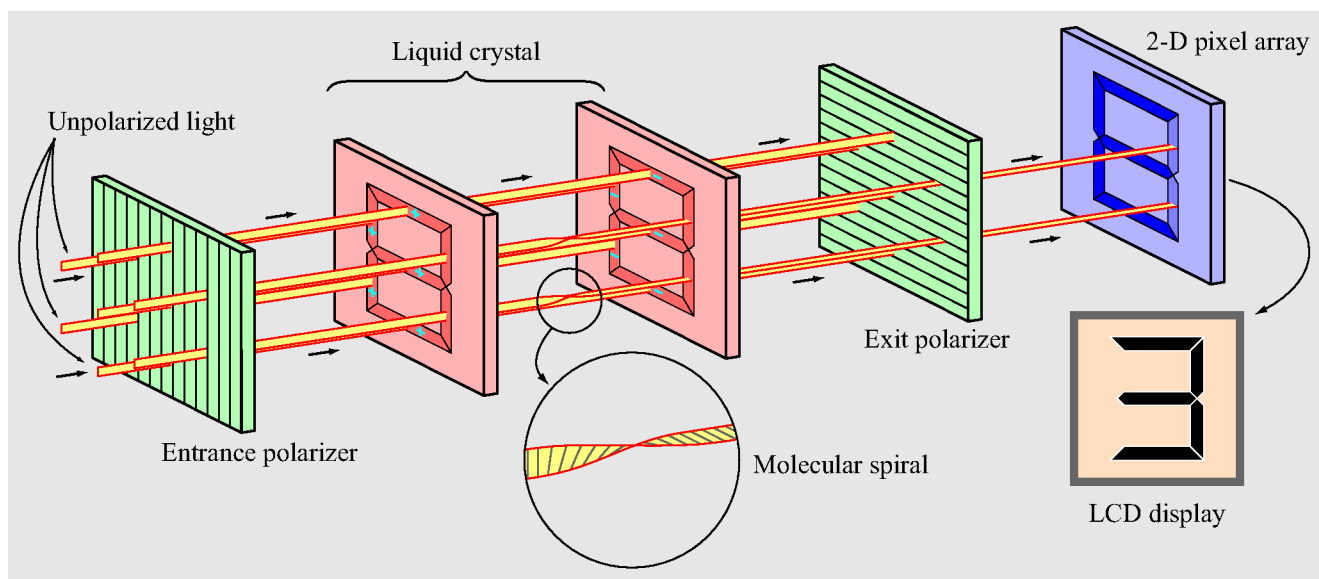
Figure 1-17 Individual bands of the radio spectrum and their primary allocations in the US.

Figure 1-18 Relation between rectangular and polar representations of a complex number.

Figure 1-19 Complex numbers  $V$  and  $I$  in the complex plane.

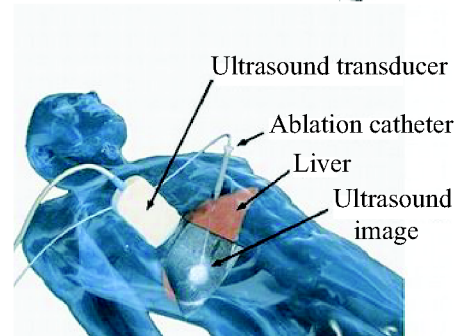
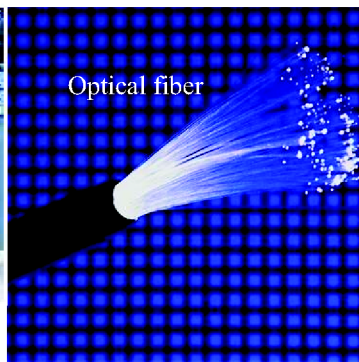
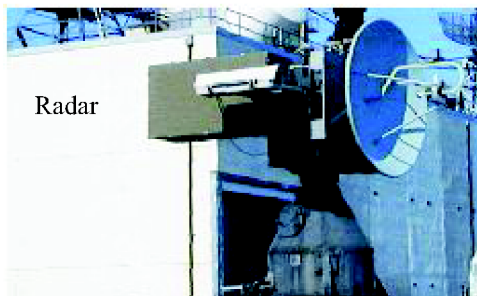
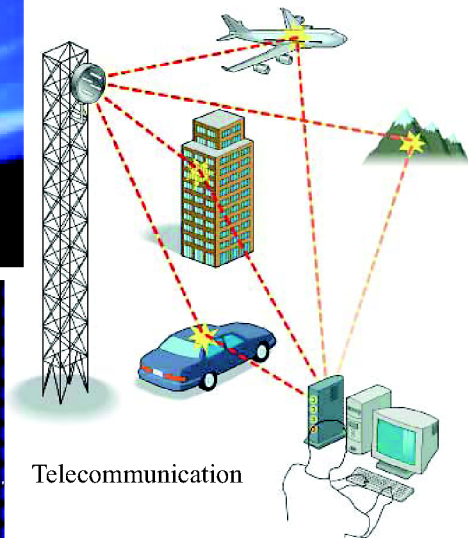
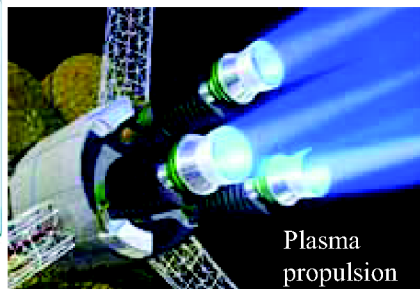
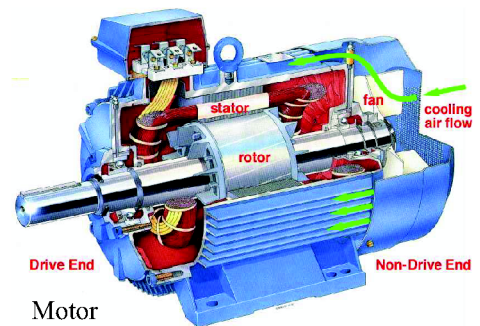
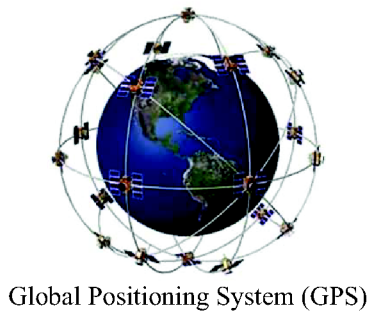
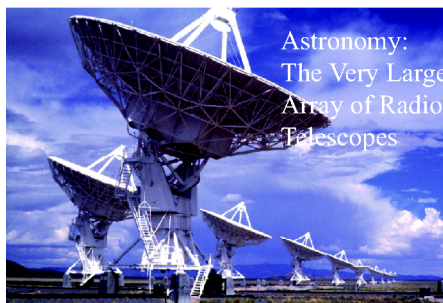
Figure 1-20  $RC$  circuit connected to a voltage source.

Figure 1-21  $RL$  circuit.



**Figure 1-1:** 2-D LCD array.





Microwave ablation for  
liver cancer treatment

**Figure 1-2:** Electromagnetics is at the heart of numerous systems and applications.

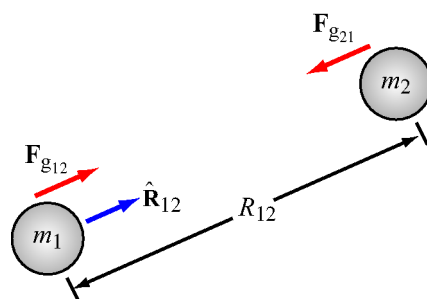


**Figure 1-3:** Gravitational forces between two masses.

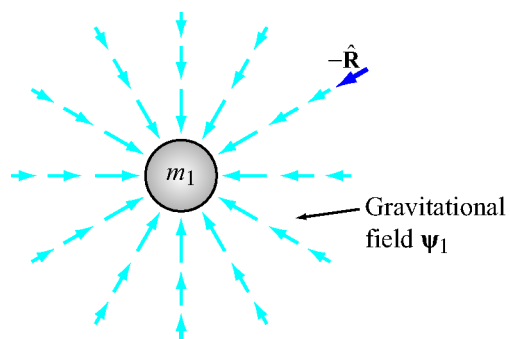


**Figure 1-4:** Gravitational field  $\boldsymbol{\psi}_1$  induced by a mass  $m_1$ .

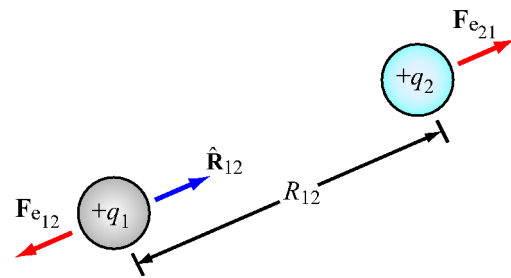


**Figure 1-5:** Electric forces on two positive point charges in free space.

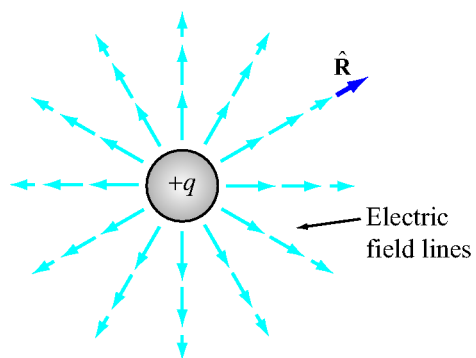


**Figure 1-6:** Electric field  $\mathbf{E}$  due to charge  $q$ .

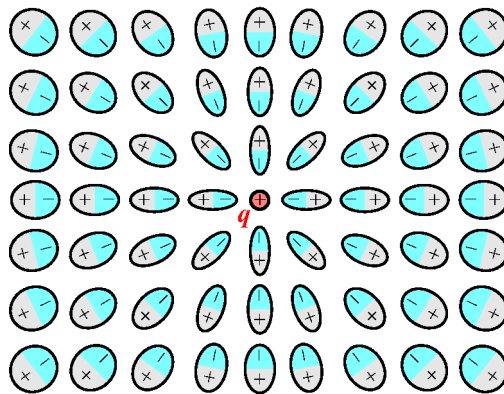


**Figure 1-7:** Polarization of the atoms of a dielectric material by a positive charge  $q$ .

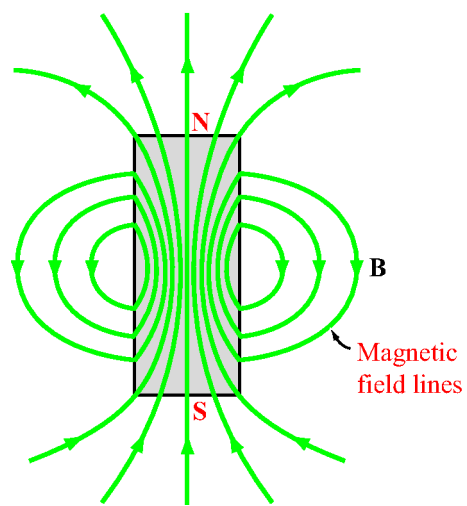


**Figure 1-8:** Pattern of magnetic field lines around a bar magnet.

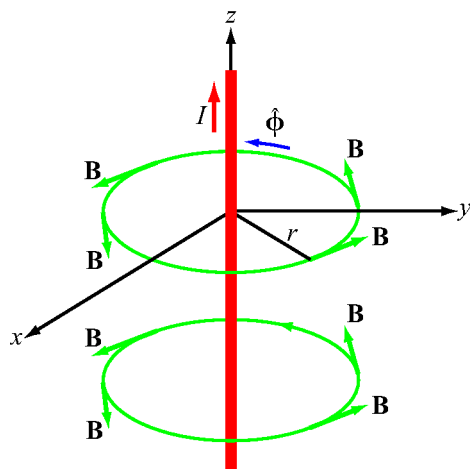


**Figure 1-9:** The magnetic field induced by a steady current flowing in the  $z$ -direction.



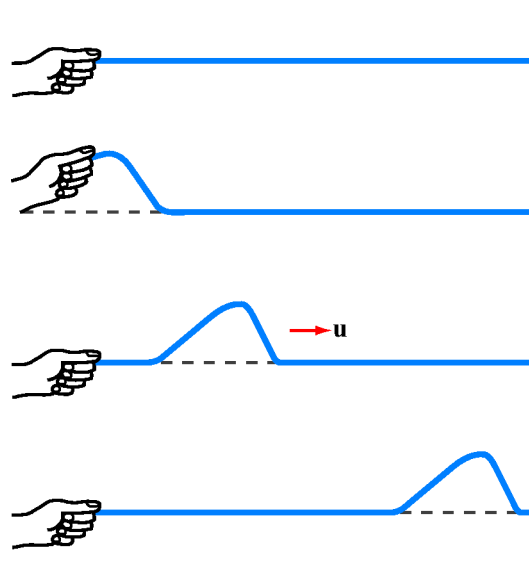


**Figure 1-10:** A one-dimensional wave traveling on a string.

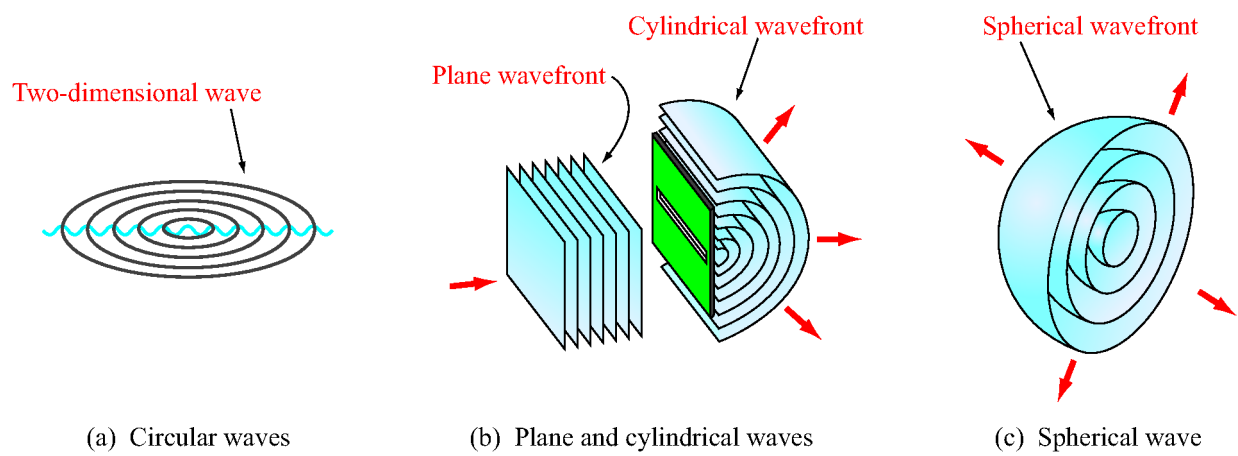
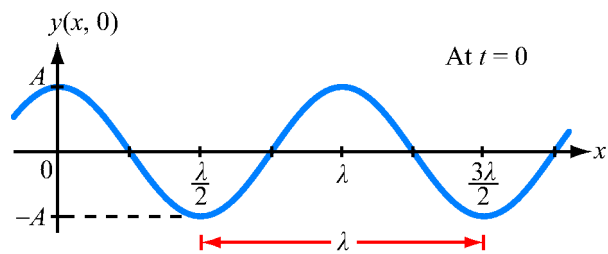
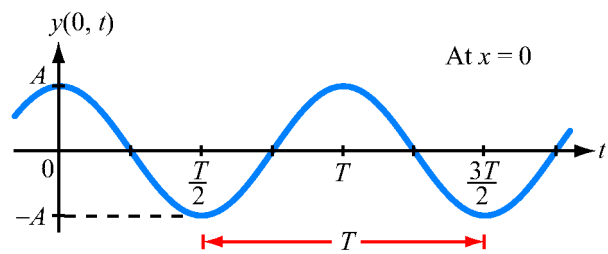


**Figure 1-11:** Examples of two-dimensional and three-dimensional waves: (a) circular waves on a pond, (b) a plane light wave exciting a cylindrical light wave through the use of a long narrow slit in an opaque screen, and (c) a sliced section of a spherical wave.



(a)  $y(x, t)$  versus  $x$  at  $t = 0$



(b)  $y(x, t)$  versus  $t$  at  $x = 0$

**Figure 1-12:** Plots of  $y(x, t) = A \cos \left( \frac{2\pi t}{T} - \frac{2\pi x}{\lambda} \right)$  as a function of (a)  $x$  at  $t = 0$  and (b)  $t$  at  $x = 0$ .

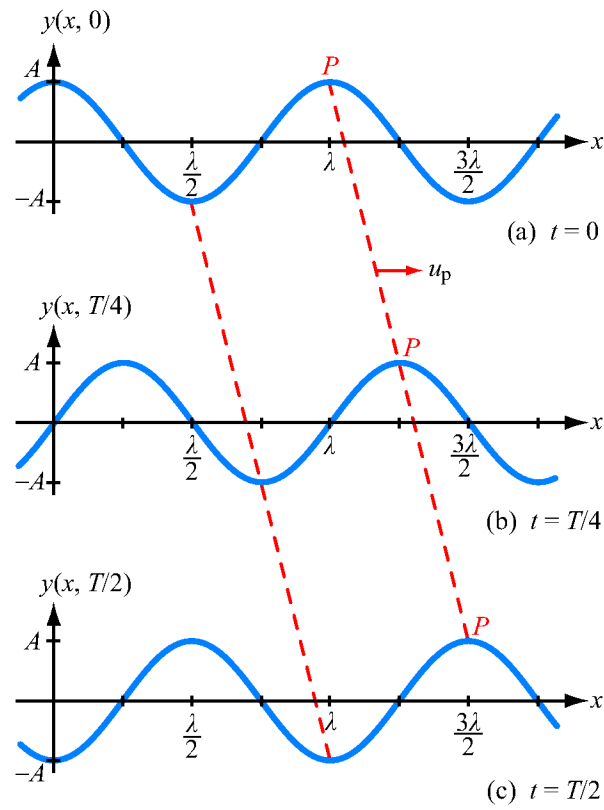


**Figure 1-13:** Plots of  $y(x, t) = A \cos\left(\frac{2\pi t}{T} - \frac{2\pi x}{\lambda}\right)$  as a function of  $x$  at (a)  $t = 0$ , (b)  $t = T/4$ , and (c)  $t = T/2$ . Note that the wave moves in the  $+x$ -direction with a velocity  $u_p = \lambda/T$ .

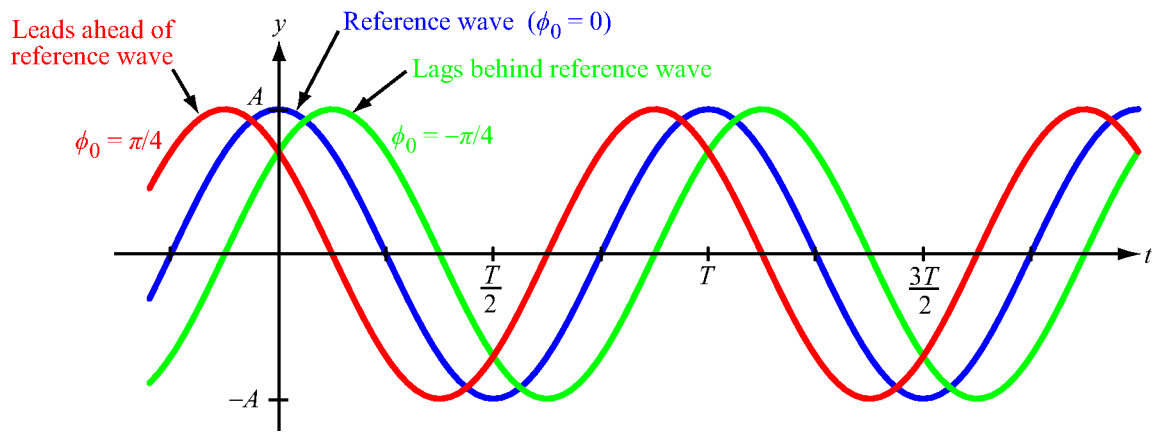


**Figure 1-14:** Plots of  $y(0, t) = A \cos[(2\pi t/T) + \phi_0]$  for three different values of the reference phase  $\phi_0$ .

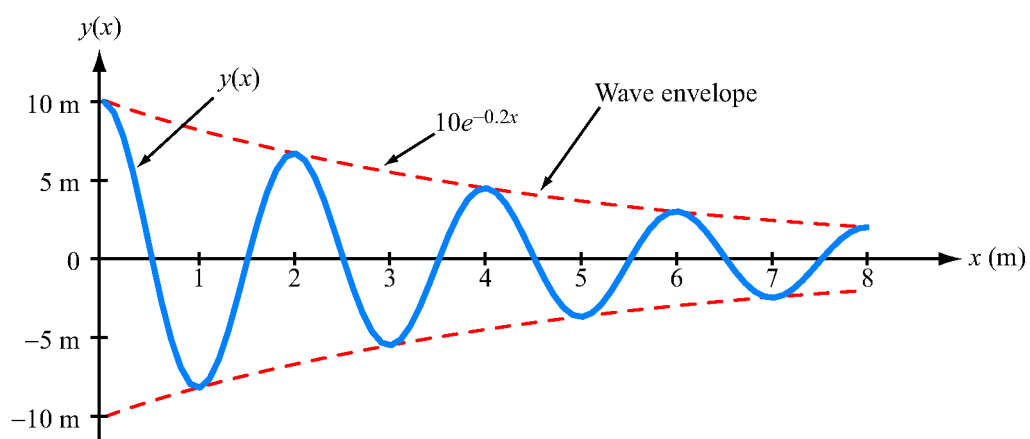


**Figure 1-15:** Plot of  $y(x) = (10e^{-0.2x} \cos \pi x)$  meters. Note that the envelope is bounded between the curve given by  $10e^{-0.2x}$  and its mirror image.

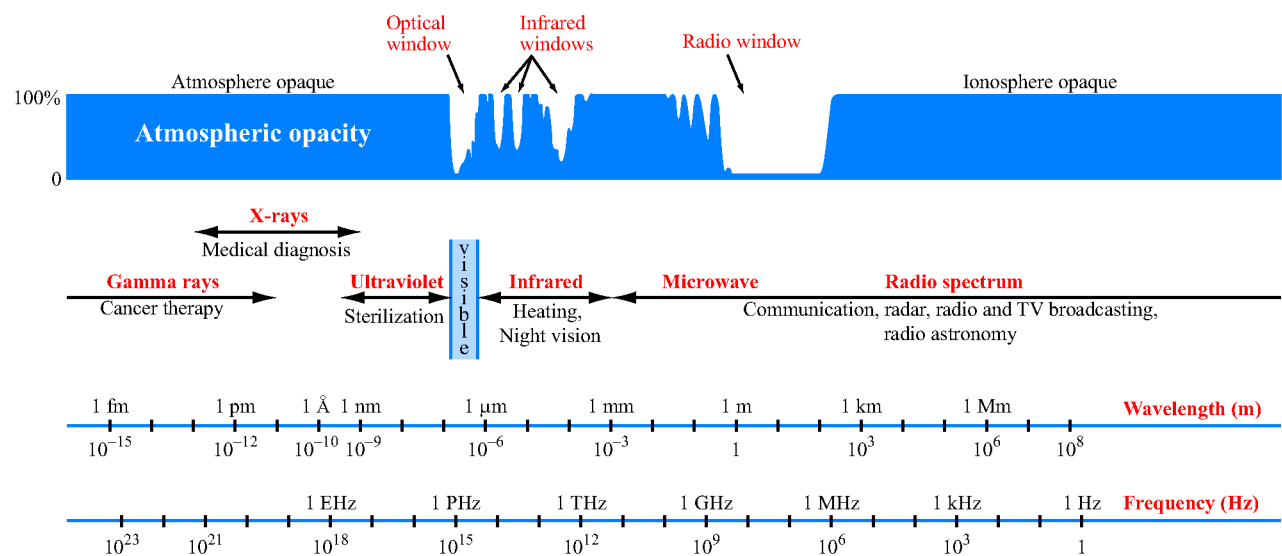


**Figure 1-16:** The electromagnetic spectrum.

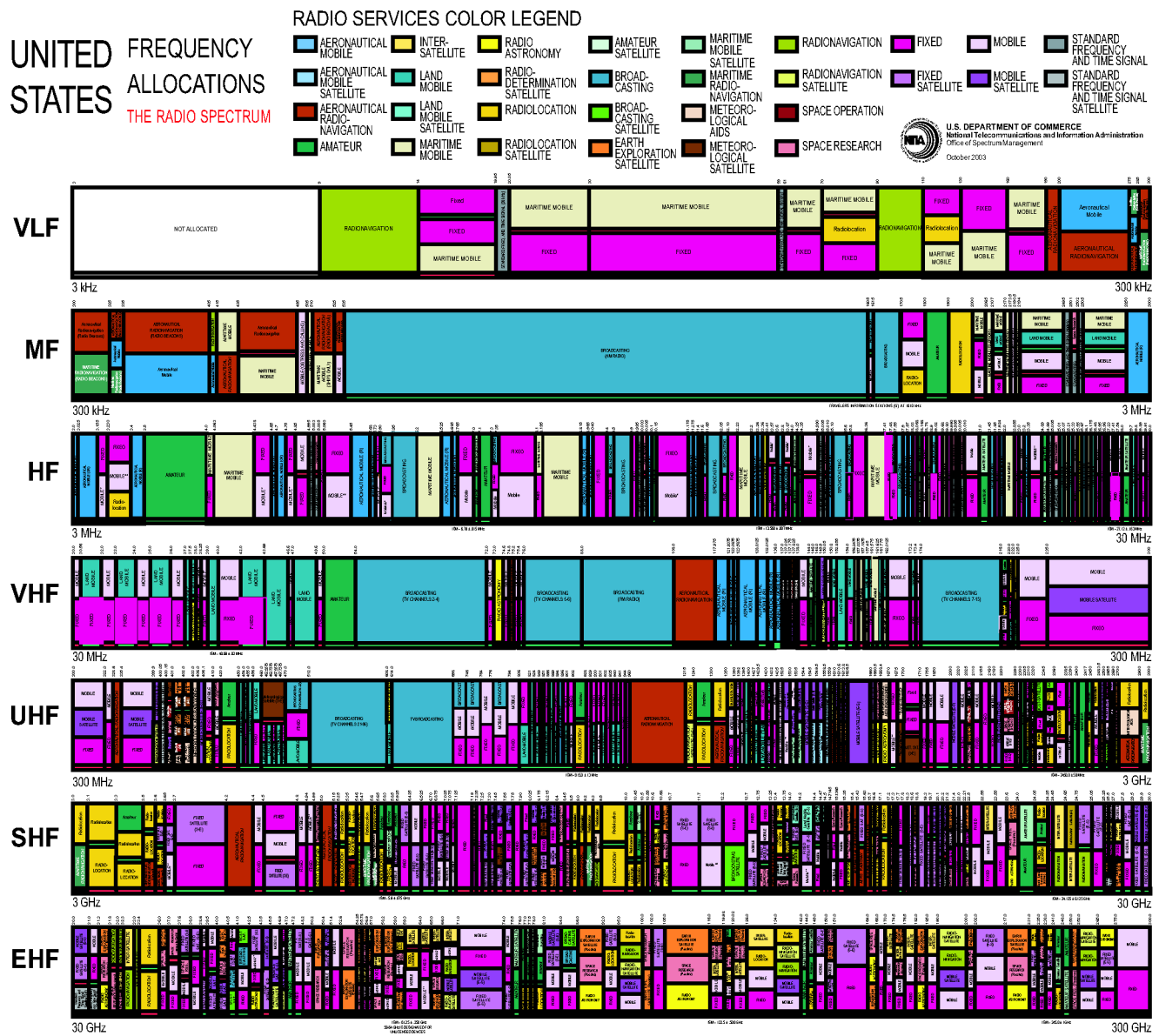


**Figure 1-17:** Individual bands of the radio spectrum and their primary allocations in the US. [See expandable version on CD.]



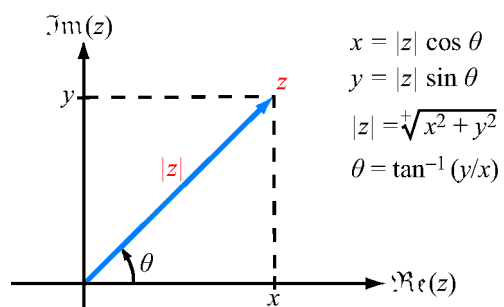


**Figure 1-18:** Relation between rectangular and polar representations of a complex number  $z = x + jy = |z|e^{j\theta}$ .

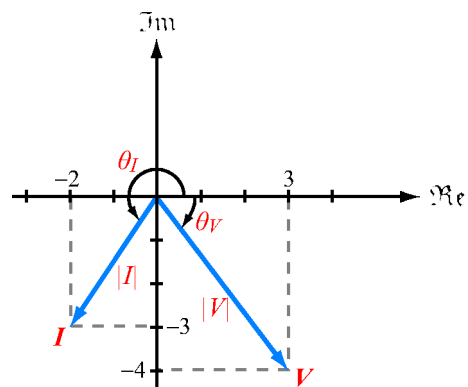


**Figure 1-19:** Complex numbers  $V$  and  $I$  in the complex plane (Example 1-3).

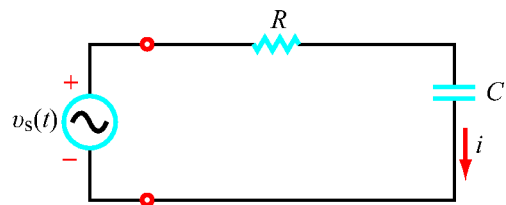


**Figure 1-20:**  $RC$  circuit connected to a voltage source  $v_s(t)$ .

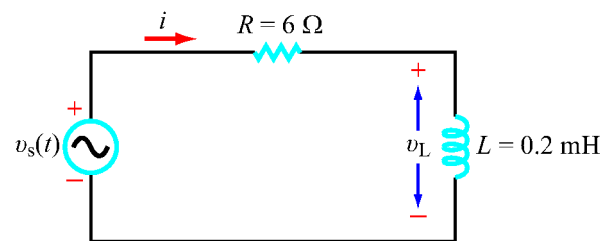


**Figure 1-21:**  $RL$  circuit (Example 1-4).

## Chapter 2 Figures

**Figure 2-1** A transmission line is a two-port network connecting a generator circuit at the sending end to a load at the receiving end.

**Figure 2-2** Generator connected to an  $RC$  circuit through a transmission line of length  $l$ .

**Figure 2-3** A dispersionless line does not distort signals passing through it regardless of its length, whereas a dispersive line distorts the shape of the input pulses because the different frequency components propagate at different velocities. The degree of distortion is proportional to the length of the dispersive line.

**Figure 2-4** A few examples of transverse electromagnetic (TEM) and higher-order transmission lines.

**Figure 2-5** In a coaxial line, the electric field is in the radial direction between the inner and outer conductors, and the magnetic field forms circles around the inner conductor.

**Figure 2-6** Regardless of its cross-sectional shape, a TEM transmission line is represented by the parallel-wire configuration shown in (a). To obtain equations relating voltages and currents, the line is subdivided into small differential sections (b), each of which is then represented by an equivalent circuit (c).

**Figure 2-7** Cross-section of a coaxial line with inner conductor of radius  $a$  and outer conductor of radius  $b$ . The conductors have magnetic permeability  $\mu_c$ , and conductivity  $\sigma_c$ , and the spacing material between the conductors has permittivity  $\epsilon$ , permeability  $\mu$ , and conductivity  $\sigma$ .

**Figure 2-8** Equivalent circuit of a two-conductor transmission line of differential length  $\Delta z$ .

**Figure 2-9** In general, a transmission line can support two traveling waves, an incident wave (with voltage and current amplitudes  $(V_0^+, I_0^+)$ ) traveling along the  $+z$ -direction (towards the load) and a reflected wave (with  $(V_0^-, I_0^-)$ ) traveling along the  $-z$ -direction (towards the source).

**Figure 2-10** Microstrip line: (a) longitudinal view, (b) cross-sectional view, and (c) circuit example. (Courtesy of Prof. Gabriel Rebeiz, U. California at San Diego.)

**Figure 2-11** Plots of  $Z_0$  as a function of  $s$  for various types of dielectric materials.

**Figure 2-12** Transmission line of length  $l$  connected on one end to a generator circuit and on the other end to a load  $Z_L$ . The load is located at  $z = 0$  and the generator terminals are at  $z = -l$ . Coordinate  $d$  is defined as  $d = -z$ .

**Figure 2-13** RC load (Example 2-3).

**Figure 2-14** Standing-wave pattern for (a)  $|\tilde{V}(d)|$  and (b)  $|\tilde{I}(d)|$  for a lossless transmission line of characteristic impedance  $Z_0 = 50 \Omega$ , terminated in a load with a reflection coefficient  $\Gamma = 0.3e^{j30^\circ}$ . The magnitude of the incident wave  $|V_0^+| = 1 \text{ V}$ . The standing-wave ratio is  $S = |\tilde{V}|_{\max}/|\tilde{V}|_{\min} = 1.3/0.7 = 1.86$ .

**Figure 2-15** Voltage standing-wave patterns for (a) a matched load, (b) a short-circuited line, and (c) an open-circuited line.

**Figure 2-16** Slotted coaxial line (Example 2-6).

**Figure 2-17** The segment to the right of terminals  $BB'$  can be replaced with a discrete impedance equal to the wave impedance  $Z(d)$ .

**Figure 2-18** At the generator end, the terminated transmission line can be replaced with the input impedance of the line  $Z_{\text{in}}$ .

**Figure 2-19** Transmission line terminated in a short circuit: (a) schematic representation, (b) normalized voltage on the line, (c) normalized current, and (d) normalized input impedance.

**Figure 2-20** Shorted line as equivalent capacitor (Example 2-8).

**Figure 2-21** Transmission line terminated in an open circuit: (a) schematic representation, (b) normalized voltage on the line, (c) normalized current, and (d) normalized input impedance.

**Figure 2-22** Configuration for Example 2-10.

**Figure 2-23** The time-average power reflected by a load connected to a lossless transmission line is equal to the incident power multiplied by  $|\Gamma|^2$ .

**Figure 2-24** The complex  $\Gamma$  plane. Point A is at  $\Gamma_A = 0.3 + j0.4 = 0.5e^{j53^\circ}$ , and point B is at  $\Gamma_B = -0.5 - j0.2 = 0.54e^{j202^\circ}$ . The unit circle corresponds to  $|\Gamma| = 1$ . At point C,  $\Gamma = 1$ ,

corresponding to an open-circuit load, and at point  $D$ ,  $\Gamma = -1$ , corresponding to a short circuit.

**Figure 2-25** Families of  $r_L$  and  $x_L$  circles within the domain  $|\Gamma| \leq 1$ .

**Figure 2-26** Point  $P$  represents a normalized load impedance  $z_L = 2 - j1$ . The reflection coefficient has a magnitude  $|\Gamma| = \overline{OP}/\overline{OR} = 0.45$  and an angle  $\theta_r = -26.6^\circ$ . Point  $R$  is an arbitrary point on the  $r_L = 0$  circle (which also is the  $|\Gamma| = 1$  circle).

**Figure 2-27** Point  $A$  represents a normalized load  $z_L = 2 - j1$  at  $0.287\lambda$  on the WTG scale. Point  $B$  represents the line input at  $d = 0.1\lambda$  from the load. At  $B$ ,  $z(d) = 0.6 - j0.66$ .

**Figure 2-28** Point  $A$  represents a normalized load with  $z_L = 2 + j1$ . The standing wave ratio is  $S = 2.6$  (at  $P_{\max}$ ), the distance between the load and the first voltage maximum is  $d_{\max} = (0.25 - 0.213)\lambda = 0.037\lambda$ , and the distance between the load and the first voltage minimum is  $d_{\min} = (0.037 + 0.25)\lambda = 0.287\lambda$ .

**Figure 2-29** Point  $A$  represents a normalized load  $z_L = 0.6 + j1.4$ . Its corresponding normalized admittance is  $y_L = 0.25 - j0.6$ , and it is at point  $B$ .

**Figure 2-30** Solution for Example 2-11. Point  $A$  represents a normalized load  $z_L = 0.5 + j1$  at  $0.135\lambda$  on the WTG scale. At  $A$ ,  $\theta_r = 83^\circ$  and  $|\Gamma| = \overline{OA}/\overline{OO'} = 0.62$ . At  $B$ , the standing-wave ratio is  $S = 4.26$ . The distance from  $A$  to  $B$  gives  $d_{\max} = 0.115\lambda$  and from  $A$  to  $C$  gives  $d_{\min} = 0.365\lambda$ . Point  $D$  represents the normalized input impedance  $z_{in} = 0.28 - j0.40$ , and point  $E$  represents the normalized input admittance  $y_{in} = 1.15 + j1.7$ .

**Figure 2-31** Solution for Example 2-12. Point  $A$  denotes that  $S = 3$ , point  $B$  represents the location of the voltage minimum, and point  $C$  represents the load at  $0.125\lambda$  on the WTL scale from point  $B$ . At  $C$ ,  $z_L = 0.6 - j0.8$ .

**Figure 2-32** The function of a matching network is to transform the load impedance  $Z_L$  such that the input impedance  $Z_{in}$  looking into the network is equal to  $Z_0$  of the transmission line.

**Figure 2-33** Five examples of in-series and in-parallel matching networks.

**Figure 2-34** Inserting a reactive element with admittance  $Y_s$  at  $MM'$  modifies  $Y_d$  to  $Y_{in}$ .

**Figure 2-35** Solutions for Example 2-13.

**Figure 2-36** Solution for point  $C$  of Examples 2-13 and 2-14. Point  $A$  is the normalized load with  $z_L = 0.5 - j1$ ; point  $B$  is  $y_L = 0.4 + j0.8$ . Point  $C$  is the intersection of the SWR circle with the  $g_L = 1$  circle. The distance from  $B$  to  $C$  is  $d_1 = 0.063\lambda$ . The length of the shorted stub ( $E$  to  $F$ ) is  $l_1 = 0.09\lambda$  (Example 2-14).

**Figure 2-37** Solution for point  $D$  of Examples 2-13 and 2-14. Point  $D$  is the second point of intersection of the SWR circle and the  $g_L = 1$  circle. The distance  $B$  to  $D$  gives  $d_2 = 0.207\lambda$ , and the distance  $E$  to  $G$  gives  $l_2 = 0.410\lambda$  (Example 2-14).

**Figure 2-38** Shorted-stub matching network.

**Figure 2-39** A rectangular pulse  $V(t)$  of duration  $\tau$  can be represented as the sum of two step functions of opposite polarities displaced by  $\tau$  relative to each other.

**Figure 2-40** At  $t = 0^+$ , immediately after closing the switch in the circuit in (a), the circuit can be represented by the equivalent circuit in (b).

**Figure 2-41** Voltage and current distributions on a lossless transmission line at  $t = T/2$ ,  $t = 3T/2$ , and  $t = 5T/2$ , due to a unit step voltage applied to a circuit with  $R_g = 4Z_0$  and  $R_L = 2Z_0$ . The corresponding reflection coefficients are  $\Gamma_L = 1/3$  and  $\Gamma_g = 3/5$ .

**Figure 2-42** Bounce diagrams for (a) voltage and (b) current. In (c), the voltage variation with time at  $z = l/4$  for a circuit with  $\Gamma_g = 3/5$  and  $\Gamma_L = 1/3$  is deduced from the vertical dashed line at  $l/4$  in (a).

**Figure 2-43** Example 2-15.

**Figure 2-44** Time-domain reflectometer of Example 2-16.



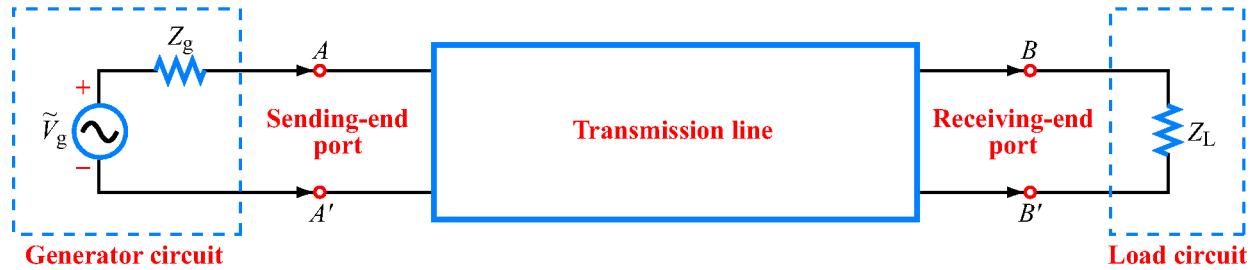


**Figure 2-1:** A transmission line is a two-port network connecting a generator circuit at the sending end to a load at the receiving end.

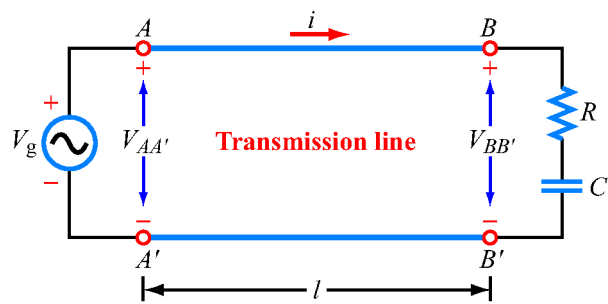


**Figure 2-2:** Generator connected to an  $RC$  circuit through a transmission line of length  $l$ .

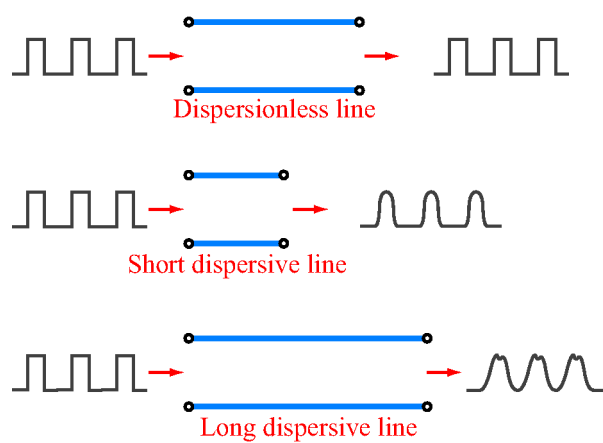
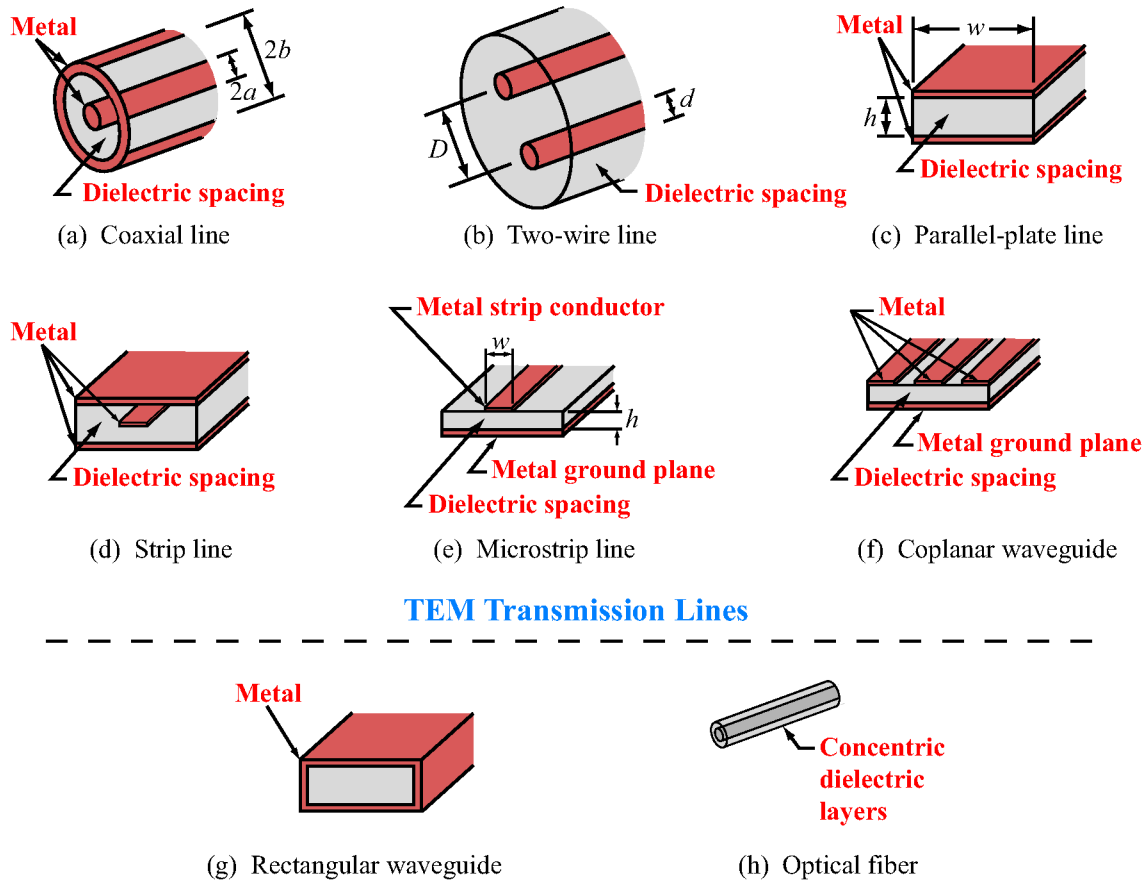


**Figure 2-3:** A dispersionless line does not distort signals passing through it regardless of its length, whereas a dispersive line distorts the shape of the input pulses because the different frequency components propagate at different velocities. The degree of distortion is proportional to the length of the dispersive line.



### TEM Transmission Lines

### Higher-Order Transmission Lines

**Figure 2-4:** A few examples of transverse electromagnetic (TEM) and higher-order transmission lines.

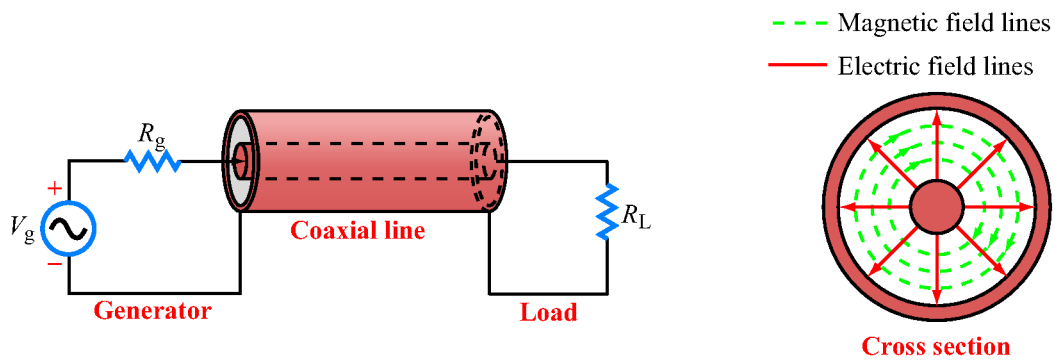


**Figure 2-5:** In a coaxial line, the electric field is in the radial direction between the inner and outer conductors, and the magnetic field forms circles around the inner conductor.

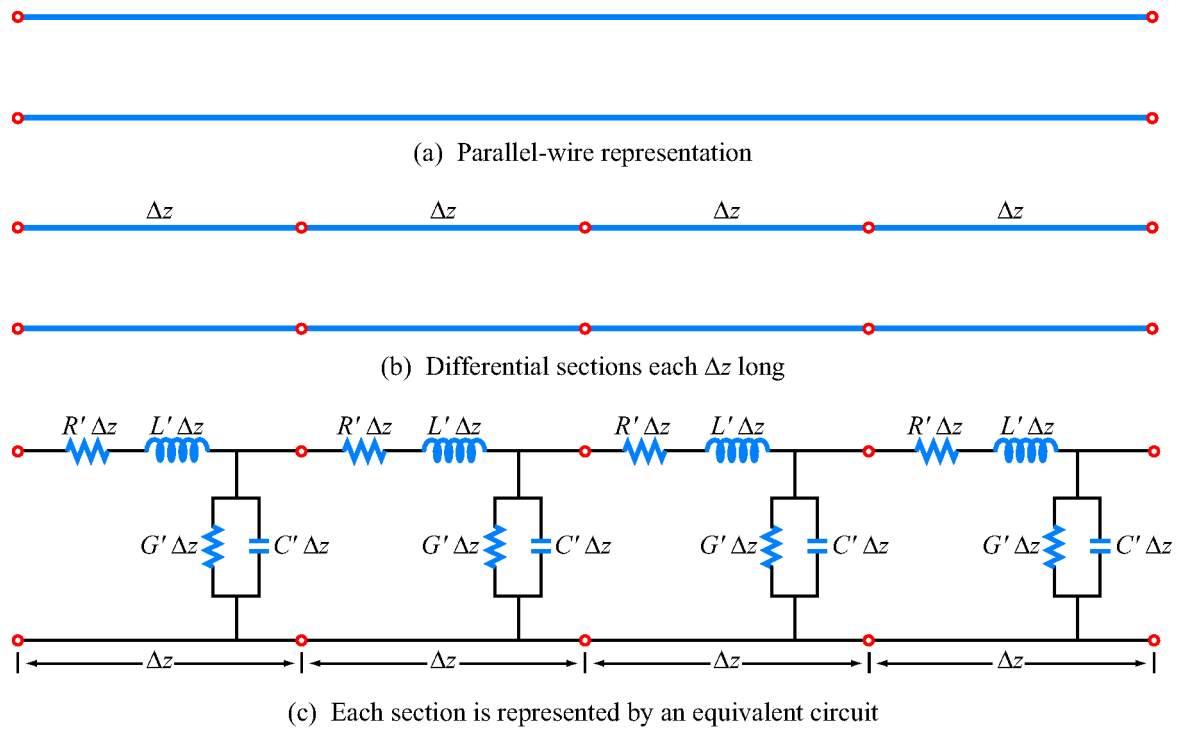


**Figure 2-6:** Regardless of its cross-sectional shape, a TEM transmission line is represented by the parallel-wire configuration shown in (a). To obtain equations relating voltages and currents, the line is subdivided into small differential sections (b), each of which is then represented by an equivalent circuit (c).

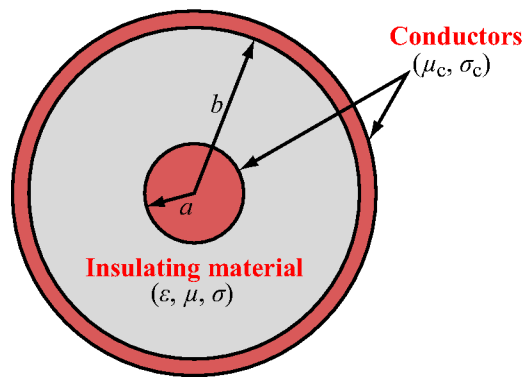


**Figure 2-7:** Cross-section of a coaxial line with inner conductor of radius  $a$  and outer conductor of radius  $b$ . The conductors have magnetic permeability  $\mu_c$ , and conductivity  $\sigma_c$ , and the spacing material between the conductors has permittivity  $\epsilon$ , permeability  $\mu$ , and conductivity  $\sigma$ .

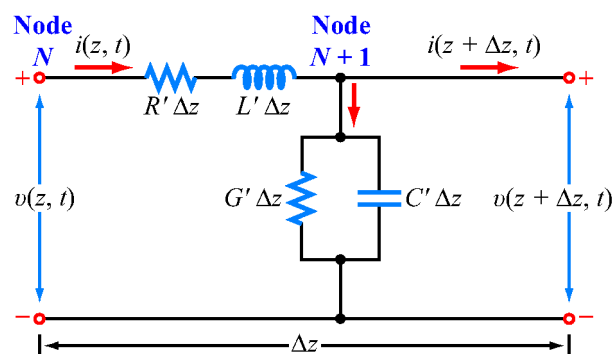


**Figure 2-8:** Equivalent circuit of a two-conductor transmission line of differential length  $\Delta z$ .



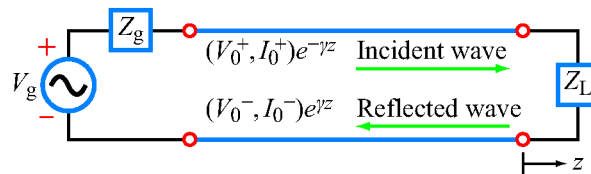
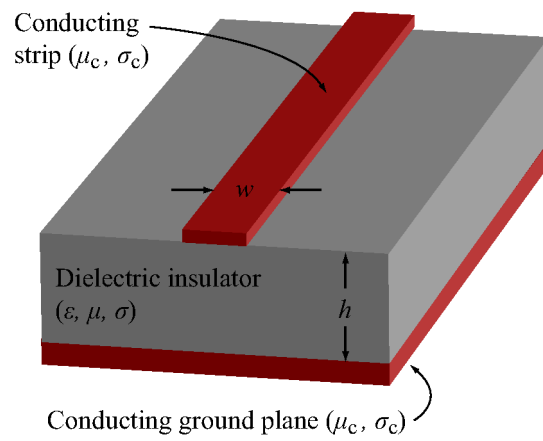
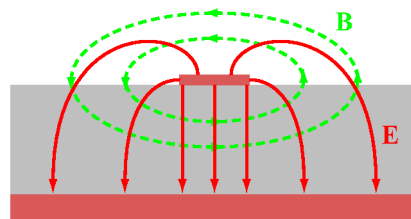


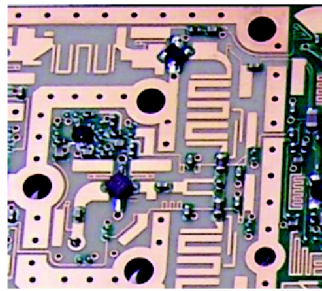
**Figure 2-9:** In general, a transmission line can support two traveling waves, an incident wave (with voltage and current amplitudes  $(V_0^+, I_0^+)$ ) traveling along the  $+z$ -direction (towards the load) and a reflected wave (with  $(V_0^-, I_0^-)$ ) traveling along the  $-z$ -direction (towards the source).



(a) Longitudinal view



(b) Cross-sectional view with **E** and **B** field lines



(c) Microwave circuit

**Figure 2-10:** Microstrip line: (a) longitudinal view, (b) cross-sectional view, and (c) circuit example. (Courtesy of Prof. Gabriel Rebeiz, U. California at San Diego.)

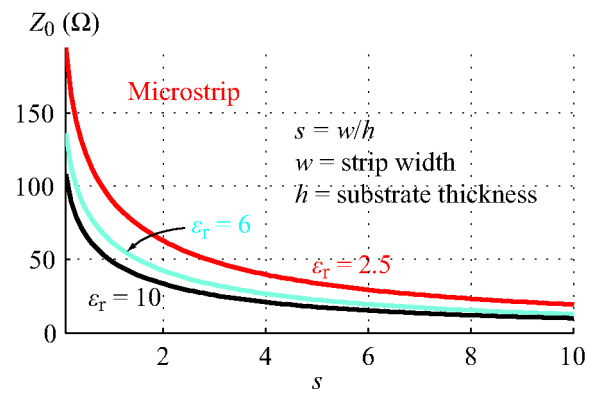


**Figure 2-11:** Plots of  $Z_0$  as a function of  $s$  for various types of dielectric materials.

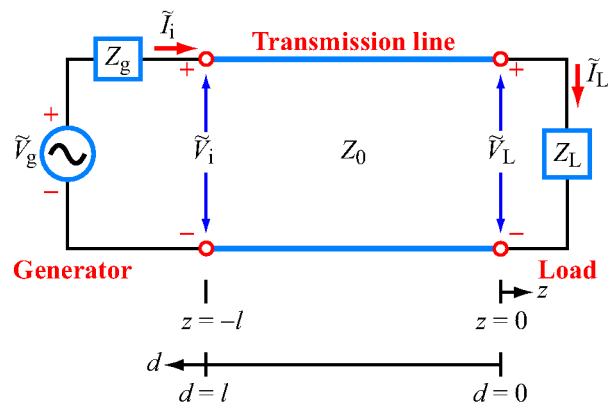


**Figure 2-12:** Transmission line of length  $l$  connected on one end to a generator circuit and on the other end to a load  $Z_L$ . The load is located at  $z = 0$  and the generator terminals are at  $z = -l$ . Coordinate  $d$  is defined as  $d = -z$ .

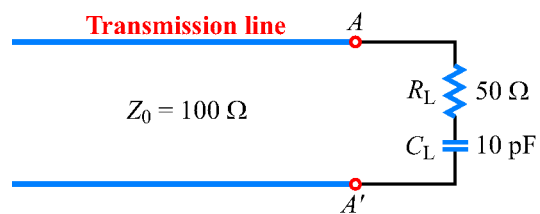


**Figure 2-13:** RC load (Example 2-3).

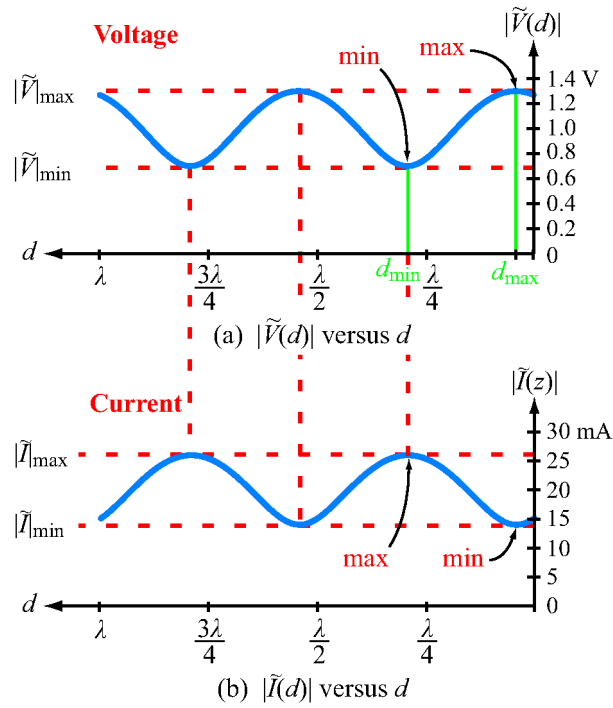


**Figure 2-14:** Standing-wave pattern for (a)  $|\tilde{V}(d)|$  and (b)  $|\tilde{I}(d)|$  for a lossless transmission line of characteristic impedance  $Z_0 = 50 \, \Omega$ , terminated in a load with a reflection coefficient  $\Gamma = 0.3e^{j30^\circ}$ . The magnitude of the incident wave  $|V_0^+| = 1 \, \text{V}$ . The standing-wave ratio is  $S = |\tilde{V}|_{\text{max}}/|\tilde{V}|_{\text{min}} = 1.3/0.7 = 1.86$ .

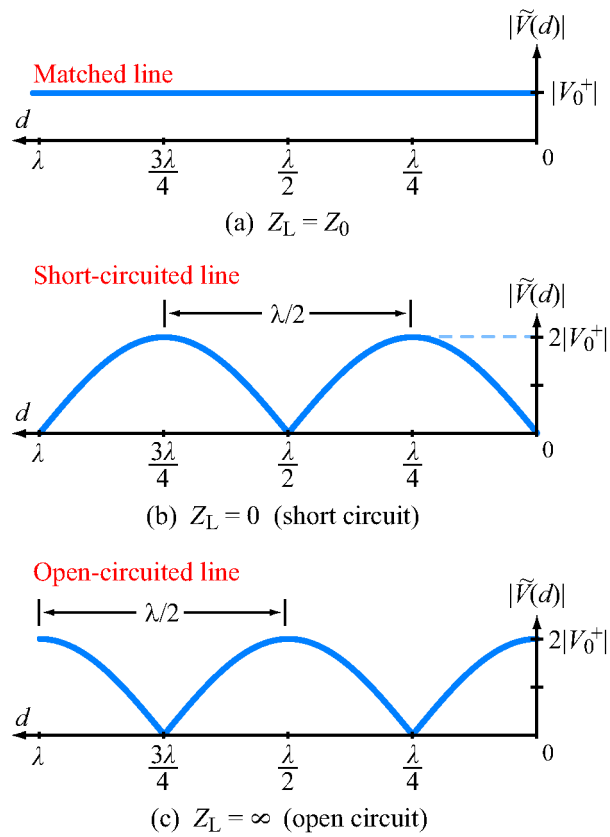


**Figure 2-15:** Voltage standing-wave patterns for (a) a matched load, (b) a short-circuited line, and (c) an open-circuited line.

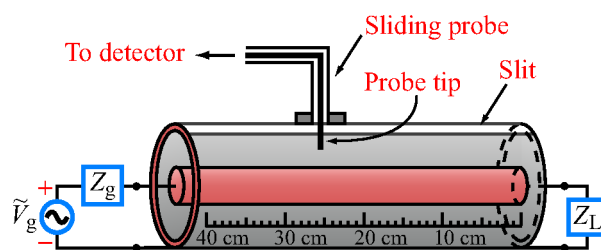
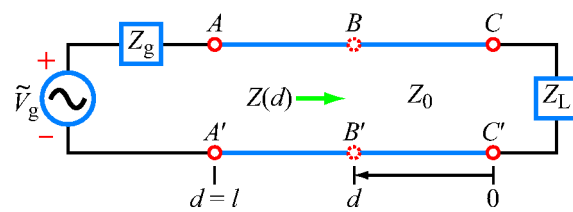
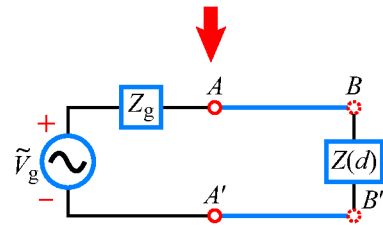


**Figure 2-16:** Slotted coaxial line (Example 2-6).





(a) Actual circuit



(b) Equivalent circuit

**Figure 2-17:** The segment to the right of terminals  $BB'$  can be replaced with a discrete impedance equal to the wave impedance  $Z(d)$ .

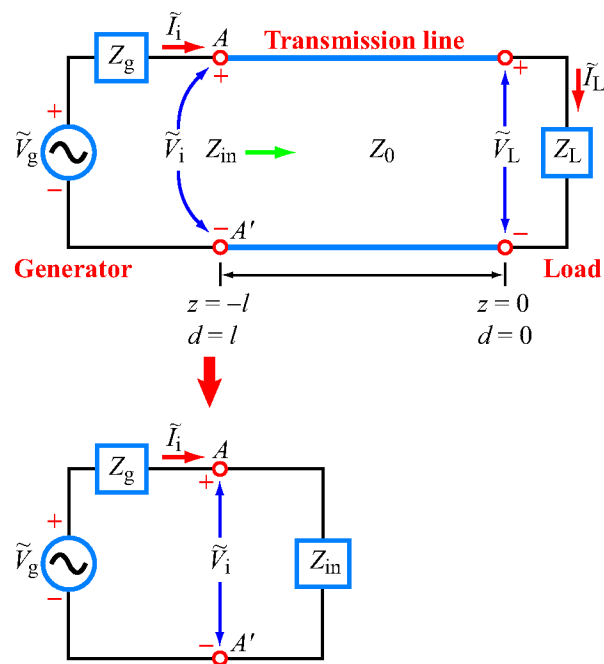


**Figure 2-18:** At the generator end, the terminated transmission line can be replaced with the input impedance of the line  $Z_{in}$ .

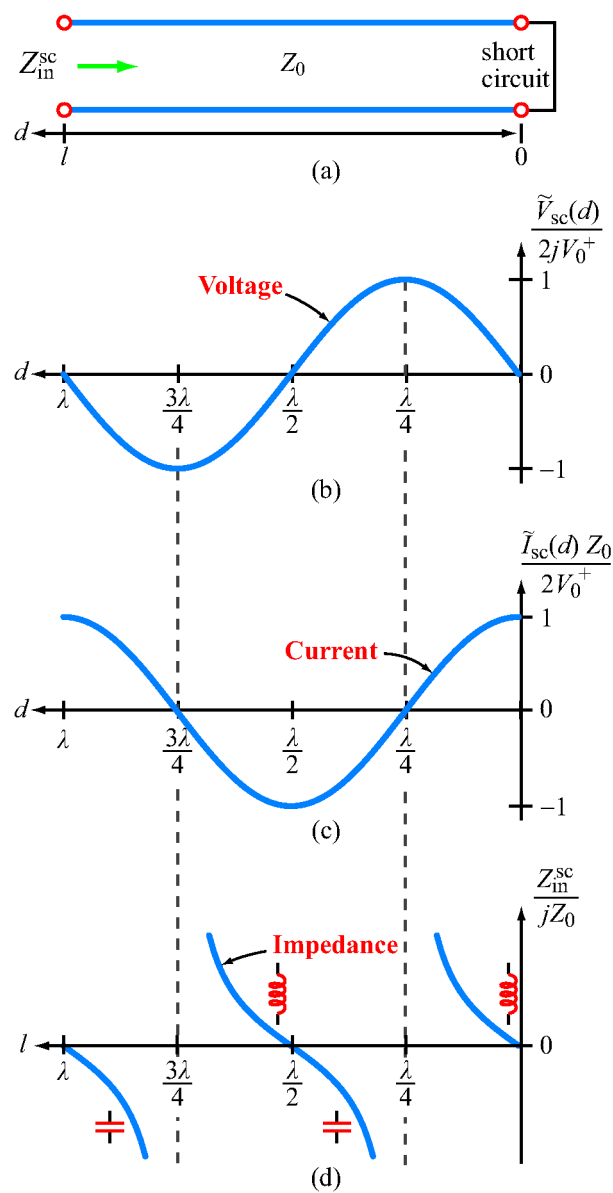


**Figure 2-19:** Transmission line terminated in a short circuit: (a) schematic representation, (b) normalized voltage on the line, (c) normalized current, and (d) normalized input impedance.

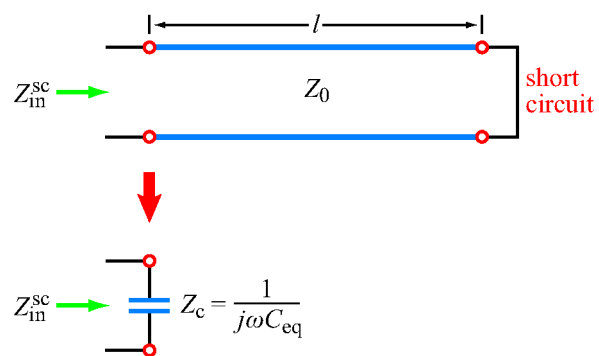


**Figure 2-20:** Shorted line as equivalent capacitor (Example 2-8).

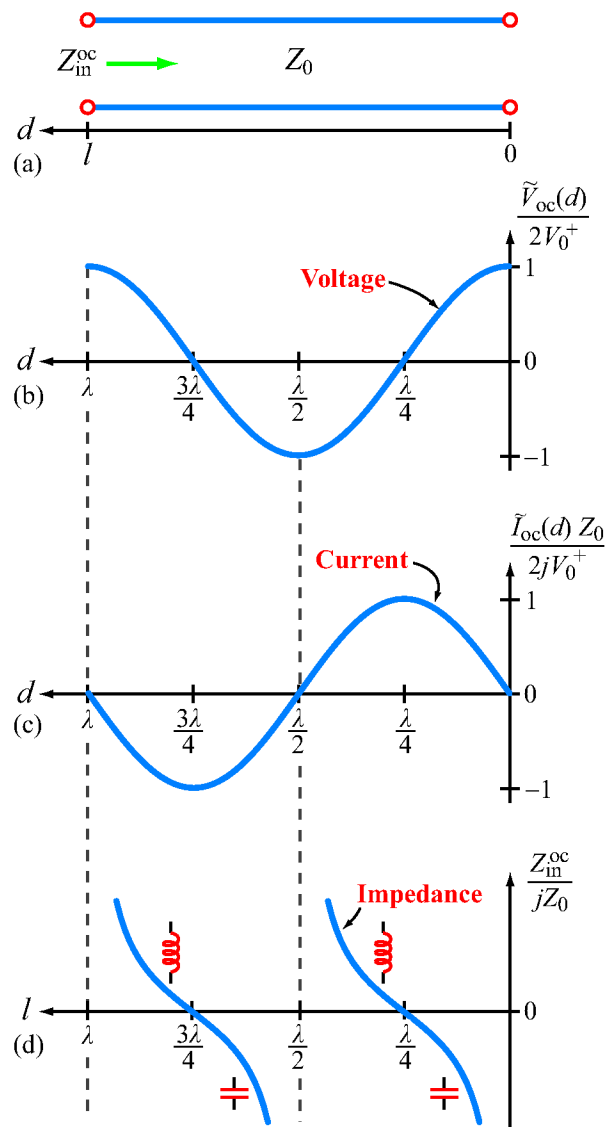


**Figure 2-21:** Transmission line terminated in an open circuit: (a) schematic representation, (b) normalized voltage on the line, (c) normalized current, and (d) normalized input impedance.

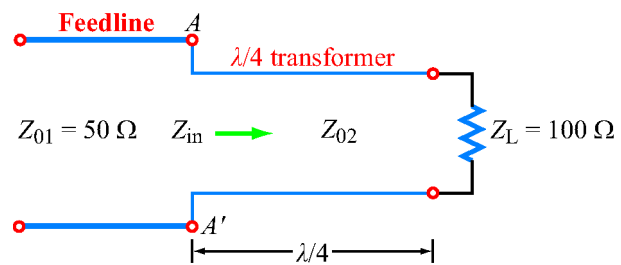


**Figure 2-22:** Configuration for Example 2-10.

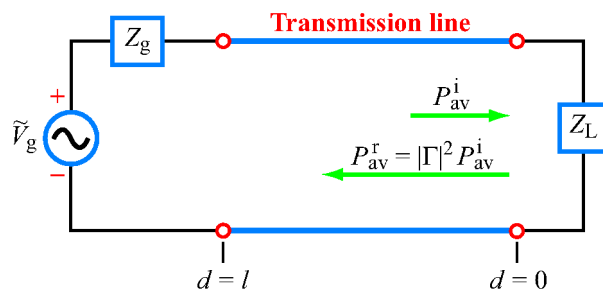


**Figure 2-23:** The time-average power reflected by a load connected to a lossless transmission line is equal to the incident power multiplied by  $|\Gamma|^2$ .

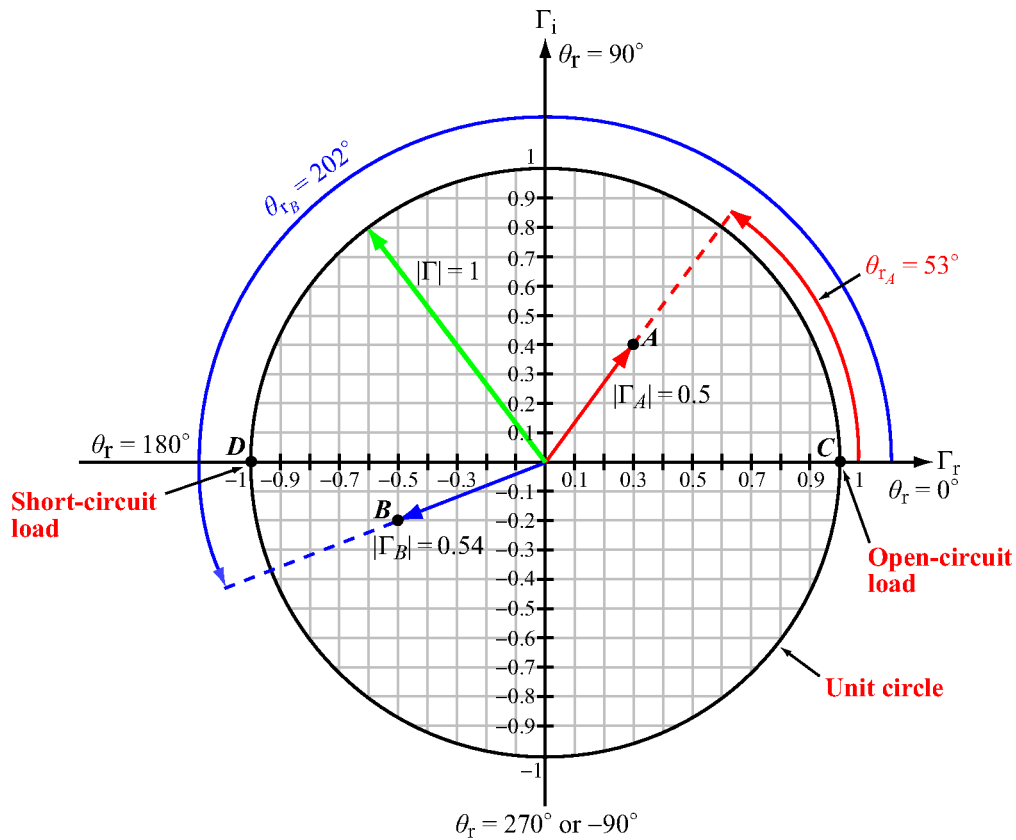


**Figure 2-24:** The complex  $\Gamma$  plane. Point A is at  $\Gamma_A = 0.3 + j0.4 = 0.5e^{j53^\circ}$ , and point B is at  $\Gamma_B = -0.5 - j0.2 = 0.54e^{j202^\circ}$ . The unit circle corresponds to  $|\Gamma| = 1$ . At point C,  $\Gamma = 1$ , corresponding to an open-circuit load, and at point D,  $\Gamma = -1$ , corresponding to a short circuit.



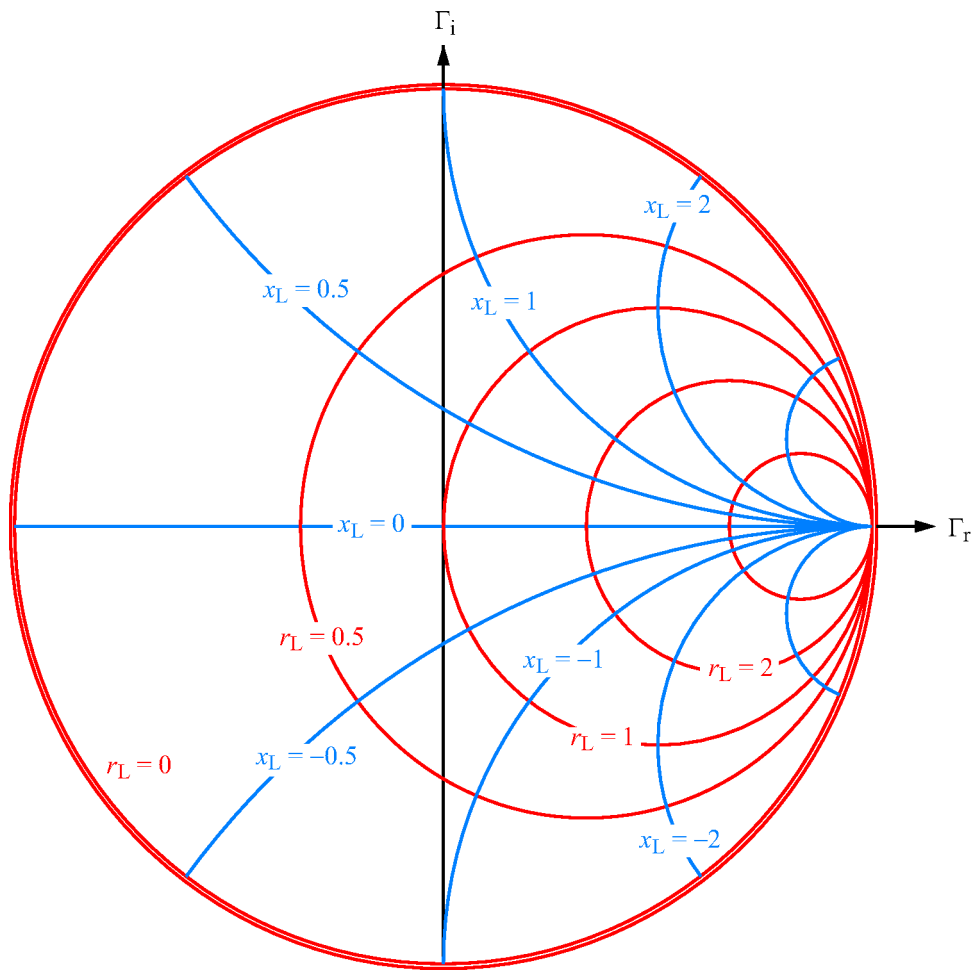


**Figure 2-25:** Families of  $r_L$  and  $x_L$  circles within the domain  $|\Gamma| \leq 1$ .

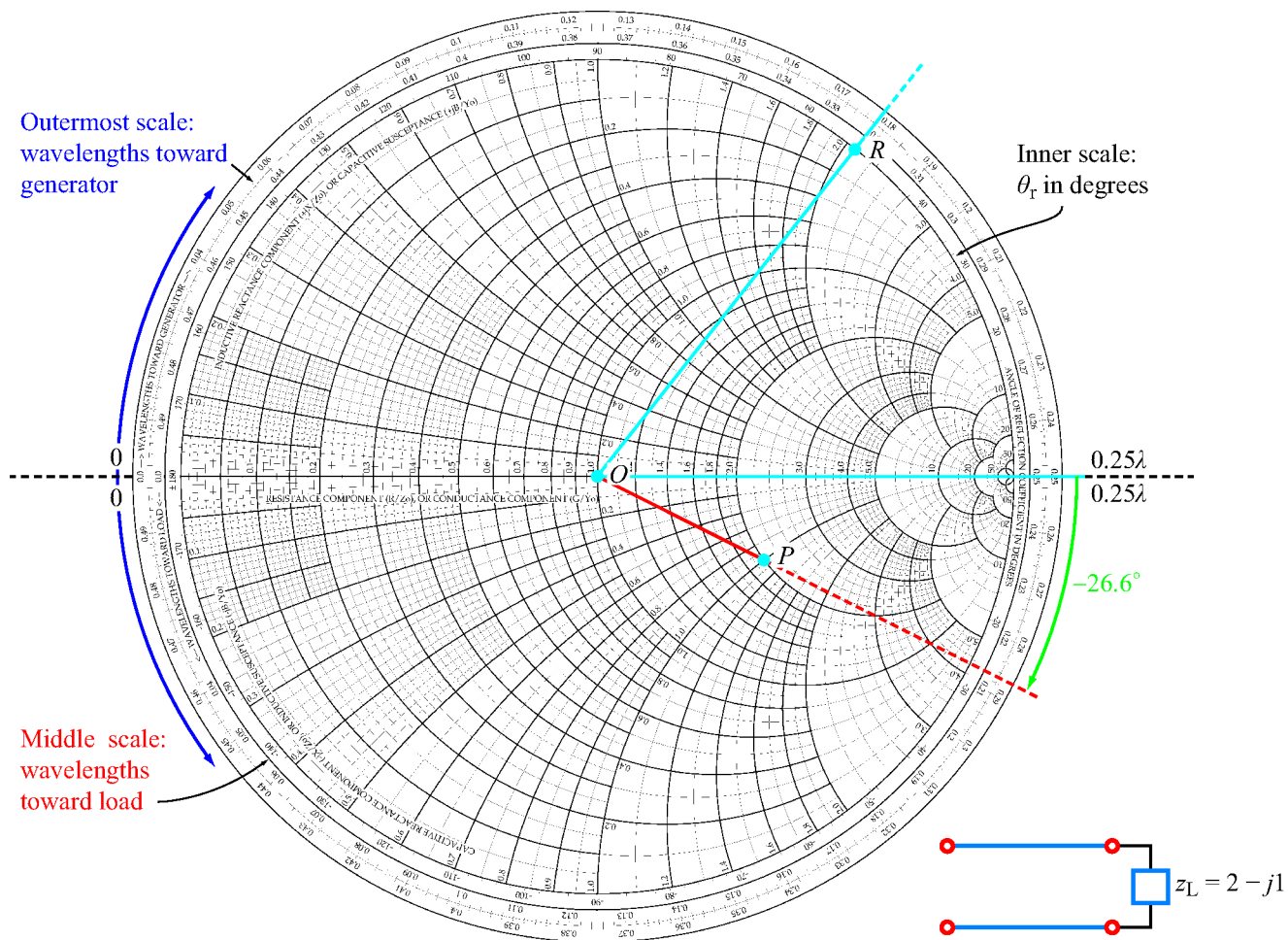


**Figure 2-26:** Point  $P$  represents a normalized load impedance  $z_L = 2 - j1$ . The reflection coefficient has a magnitude  $|\Gamma| = \overline{OP}/\overline{OR} = 0.45$  and an angle  $\theta_r = -26.6^\circ$ . Point  $R$  is an arbitrary point on the  $r_L = 0$  circle (which also is the  $|\Gamma| = 1$  circle).

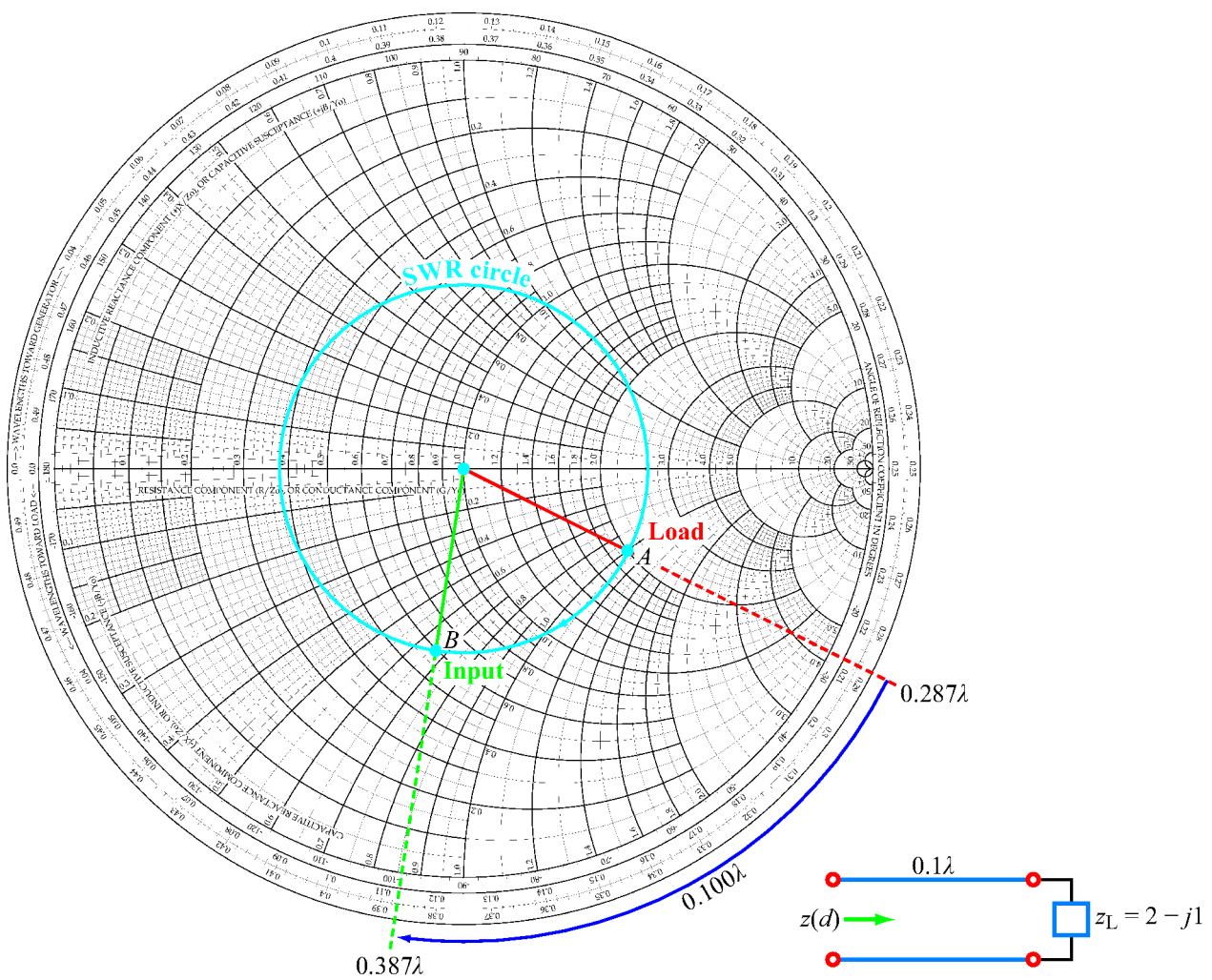


**Figure 2-27:** Point A represents a normalized load  $z_L = 2 - j1$  at  $0.287\lambda$  on the WTG scale. Point B represents the line input at  $d = 0.1\lambda$  from the load. At B,  $z(d) = 0.6 - j0.66$ .

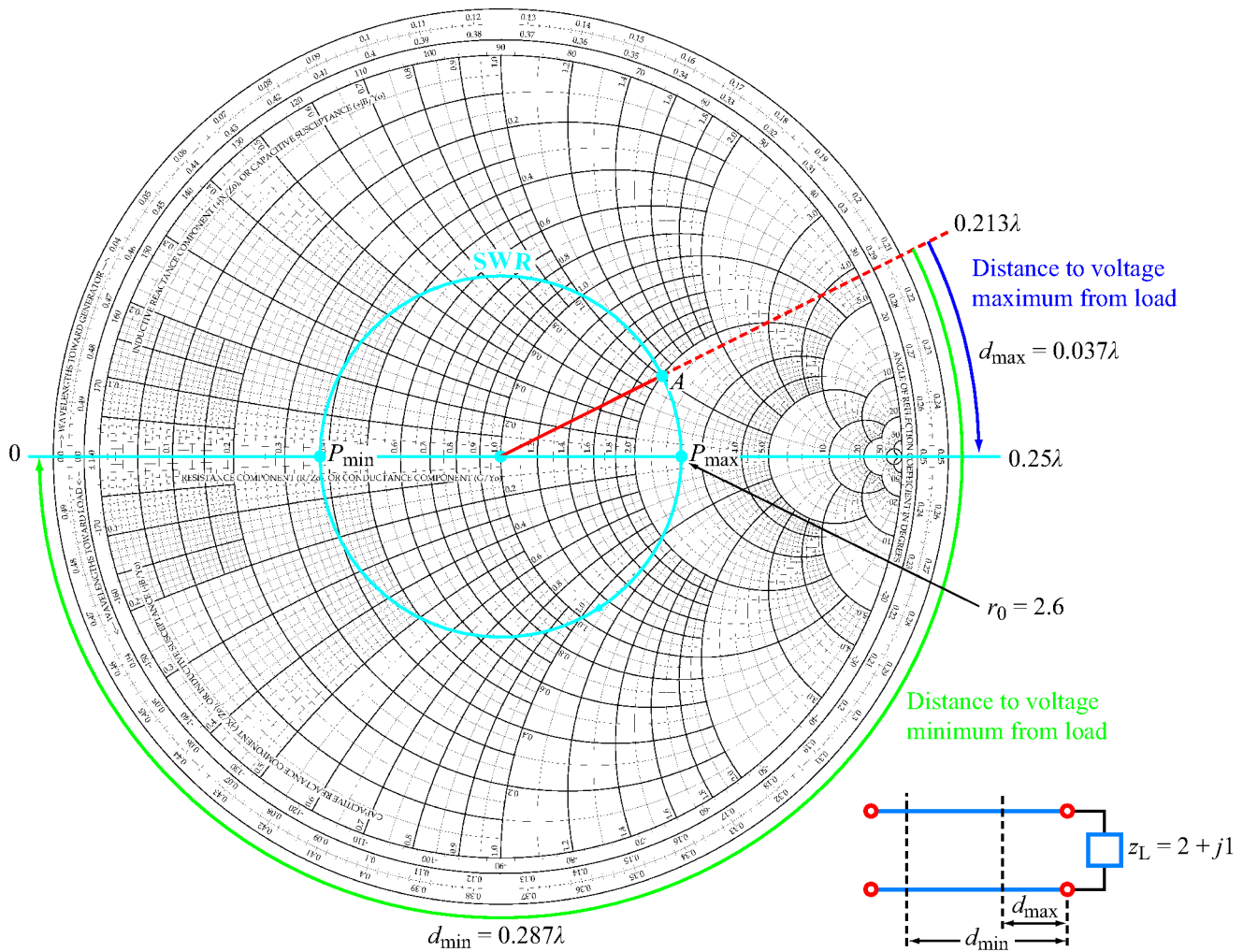


**Figure 2-28:** Point A represents a normalized load with  $z_L = 2 + j1$ . The standing wave ratio is  $S = 2.6$  (at  $P_{\max}$ ), the distance between the load and the first voltage maximum is  $d_{\max} = (0.25 - 0.213)\lambda = 0.037\lambda$ , and the distance between the load and the first voltage minimum is  $d_{\min} = (0.037 + 0.25)\lambda = 0.287\lambda$ .

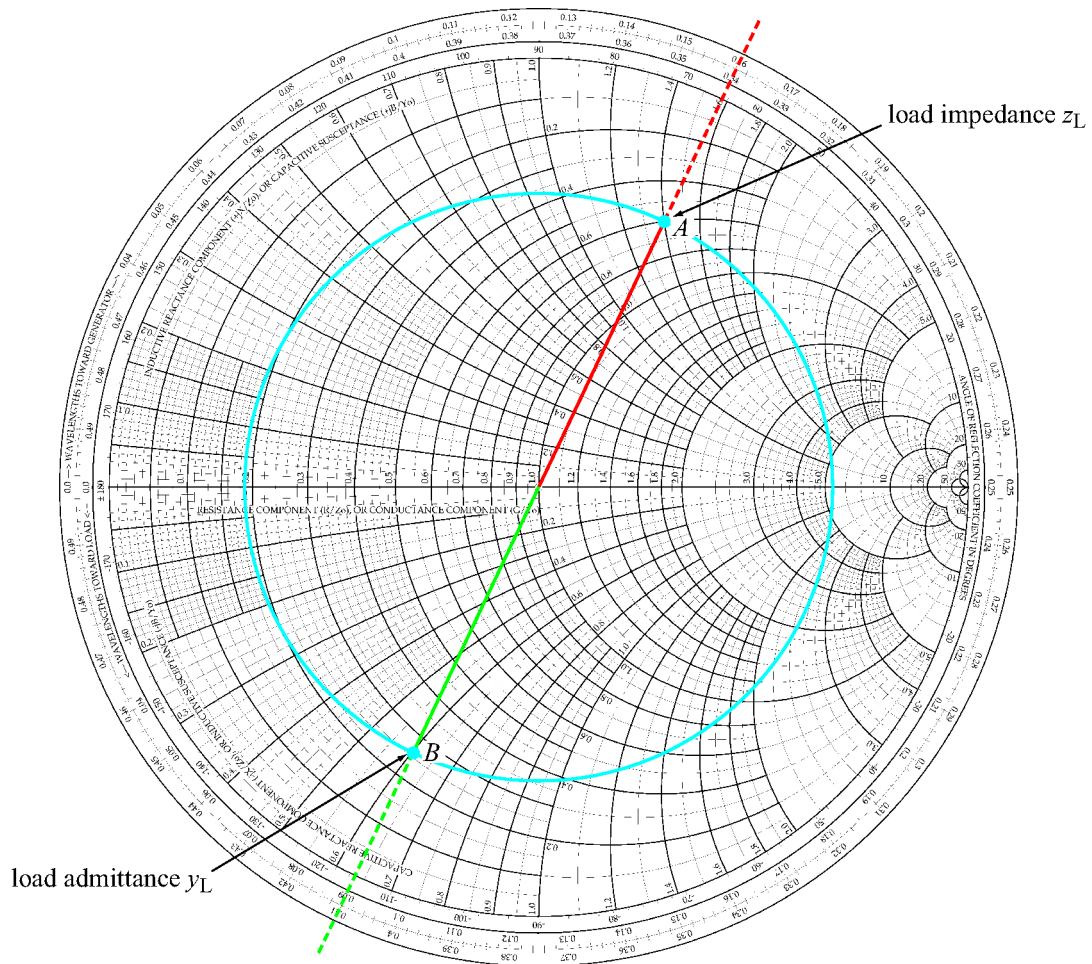


**Figure 2-29:** Point A represents a normalized load  $z_L = 0.6 + j1.4$ . Its corresponding normalized admittance is  $y_L = 0.25 - j0.6$ , and it is at point B.



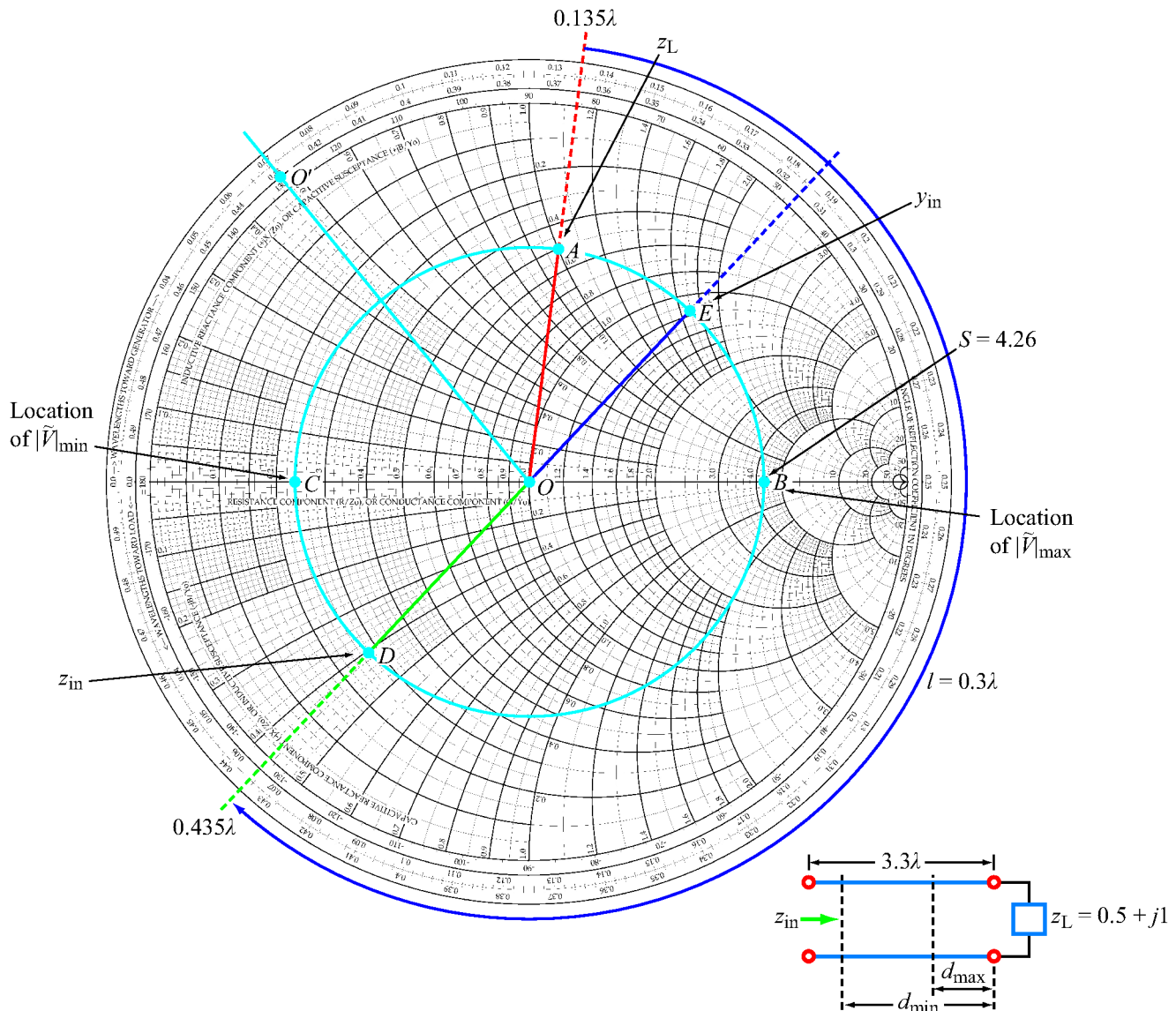


**Figure 2-30:** Solution for Example 2-11. Point A represents a normalized load  $z_L = 0.5 + j1$  at  $0.135\lambda$  on the WTG scale. At A,  $\theta_r = 83^\circ$  and  $|\Gamma| = \overline{OA}/\overline{OO'} = 0.62$ . At B, the standing-wave ratio is  $S = 4.26$ . The distance from A to B gives  $d_{\max} = 0.115\lambda$  and from A to C gives  $d_{\min} = 0.365\lambda$ . Point D represents the normalized input impedance  $z_{in} = 0.28 - j0.40$ , and point E represents the normalized input admittance  $y_{in} = 1.15 + j1.7$ .

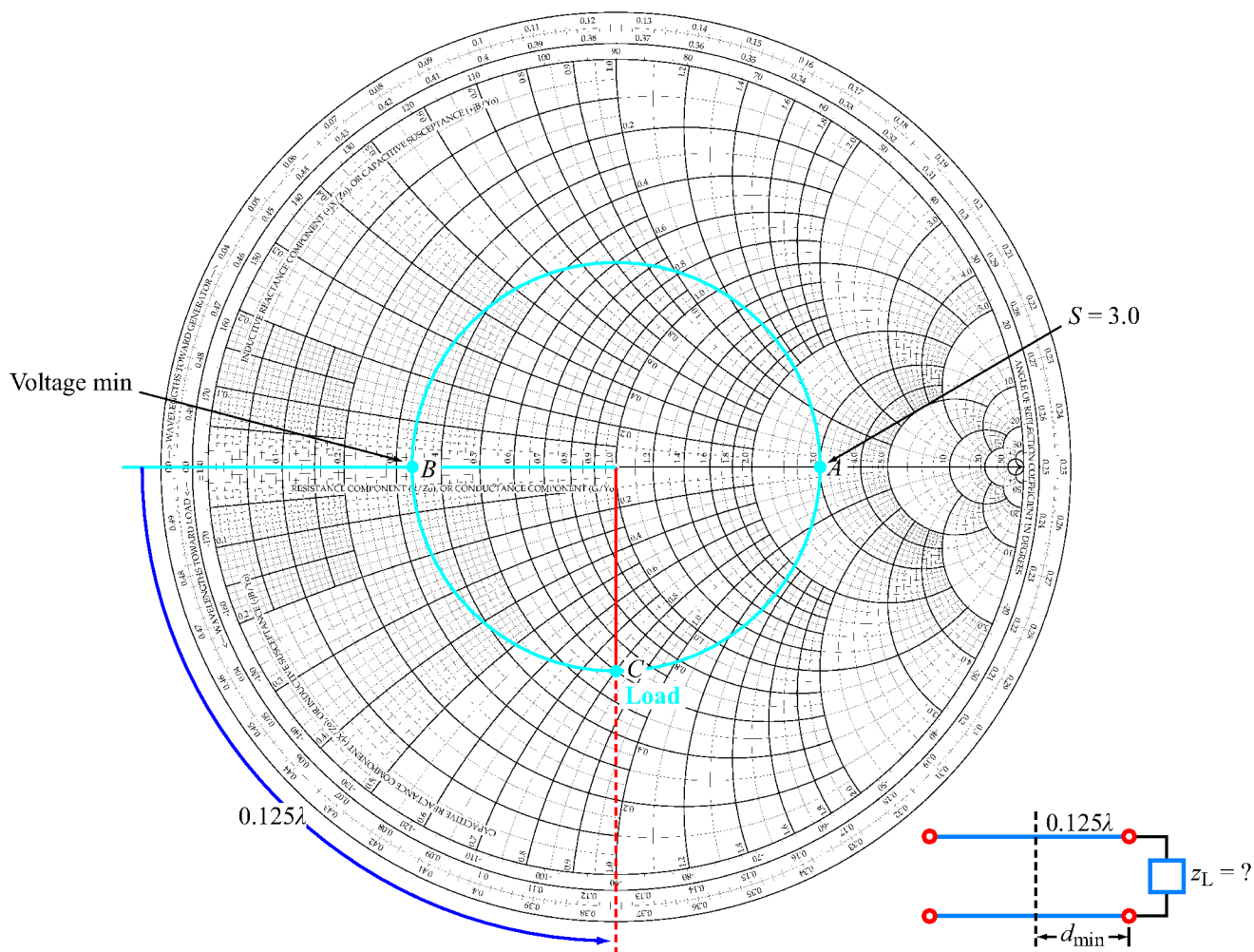


**Figure 2-31:** Solution for Example 2-12. Point A denotes that  $S = 3$ , point B represents the location of the voltage minimum, and point C represents the load at  $0.125\lambda$  on the WTL scale from point B. At C,  $z_L = 0.6 - j0.8$ .

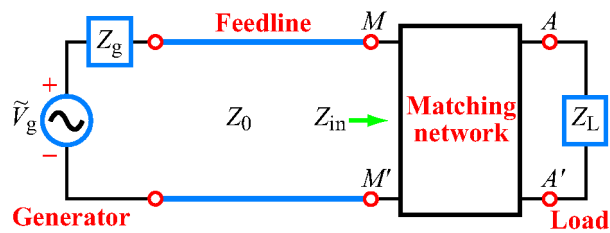
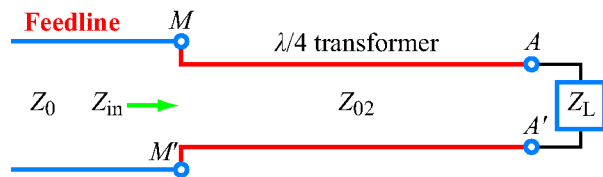
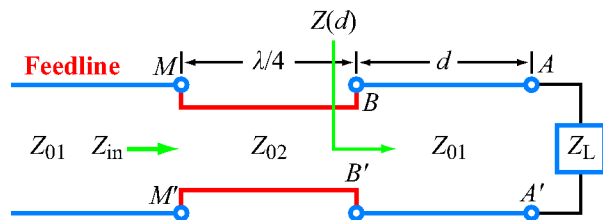


**Figure 2-32:** The function of a matching network is to transform the load impedance  $Z_L$  such that the input impedance  $Z_{in}$  looking into the network is equal to  $Z_0$  of the transmission line.

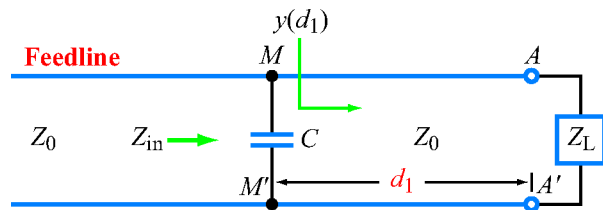




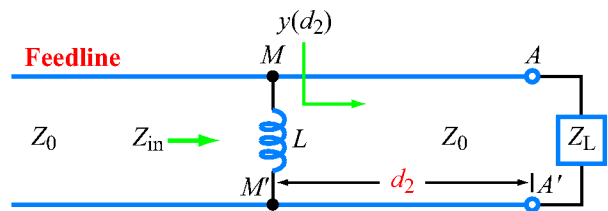
(a) In-series  $\lambda/4$  transformer inserted at  $AA'$



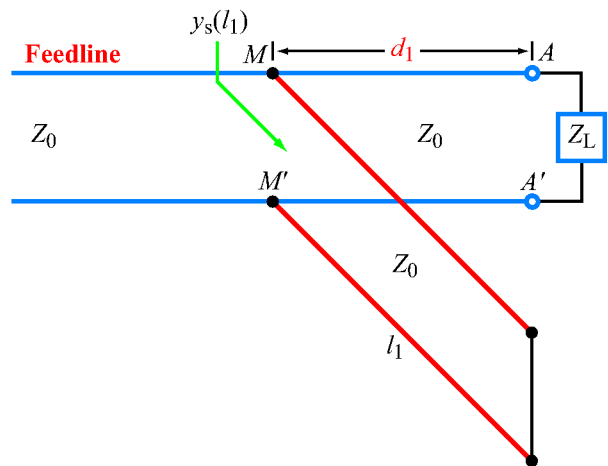
(b) In-series  $\lambda/4$  transformer inserted at  $d = d_{\max}$  or  $d = d_{\min}$



(c) In-parallel insertion of capacitor at distance  $d_1$

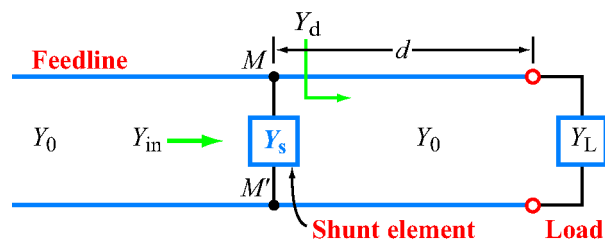


(d) In-parallel insertion of inductor at distance  $d_2$

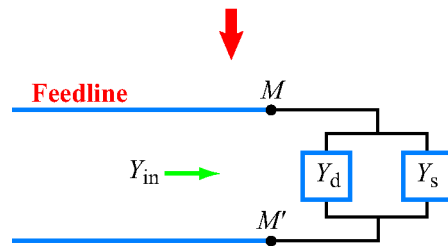


(e) In-parallel insertion of a short-circuited stub

**Figure 2-33:** Five examples of in-series and in-parallel matching networks.

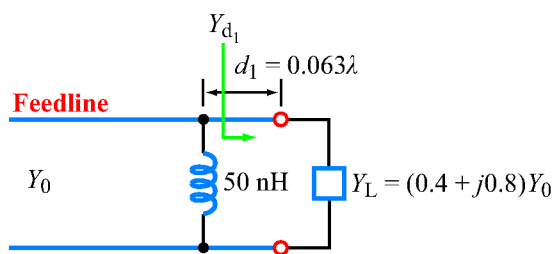


(a) Transmission-line circuit

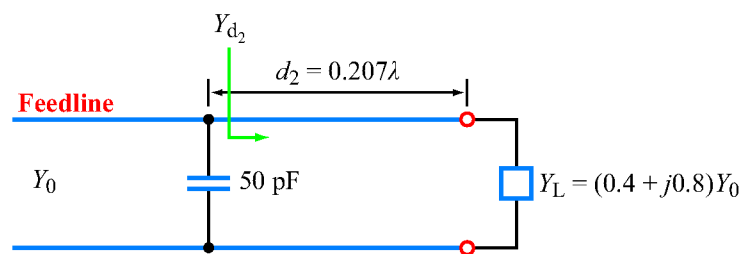


(b) Equivalent circuit

**Figure 2-34:** Inserting a reactive element with admittance  $Y_s$  at  $MM'$  modifies  $Y_d$  to  $Y_{in}$ .



(a) First solution



(b) Second solution

**Figure 2-35:** Solutions for Example 2-13.

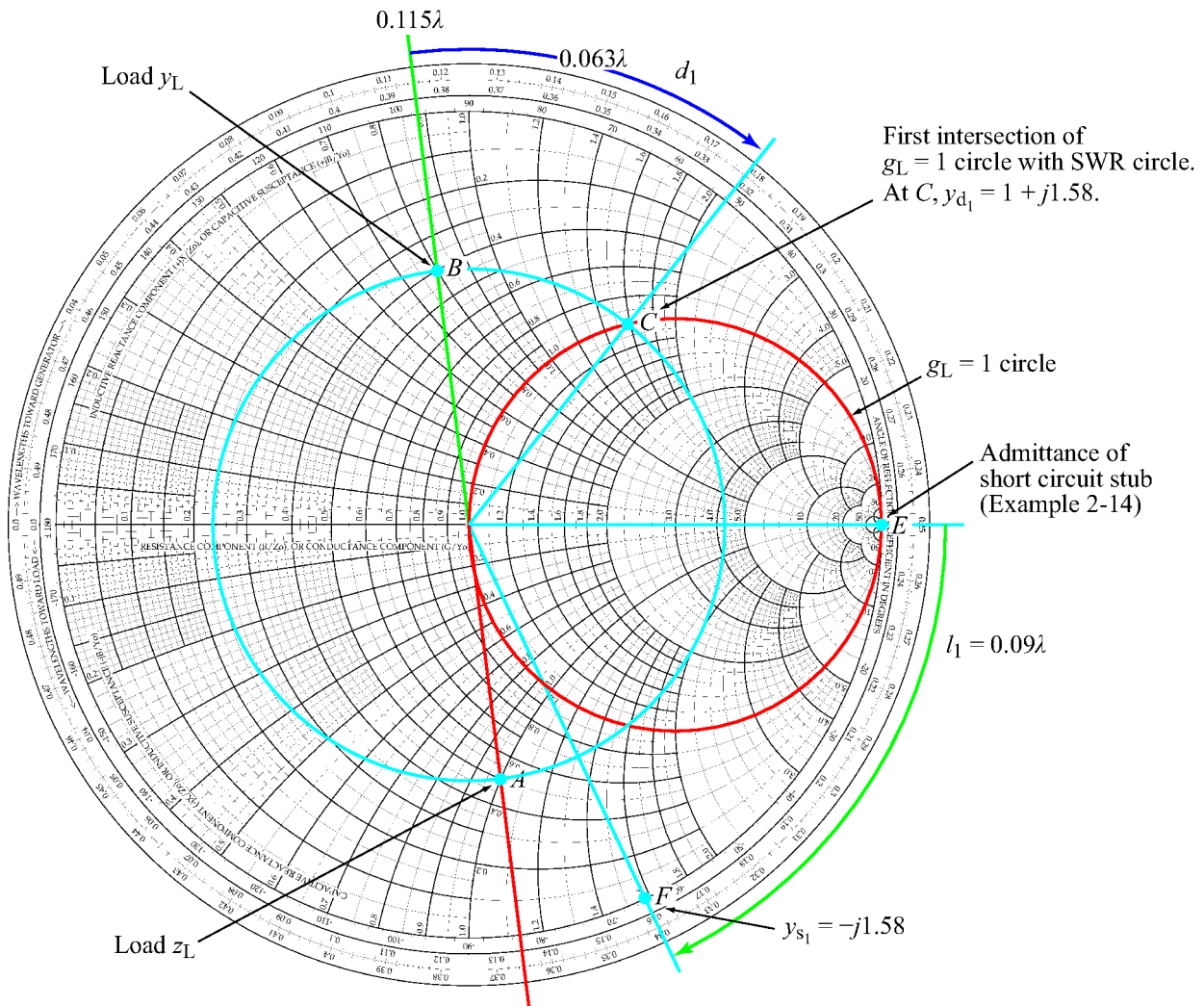


**Figure 2-36:** Solution for point C of Examples 2-13 and 2-14. Point A is the normalized load with  $z_L = 0.5 - j1$ ; point B is  $y_L = 0.4 + j0.8$ . Point C is the intersection of the SWR circle with the  $g_L = 1$  circle. The distance from B to C is  $d_1 = 0.063\lambda$ . The length of the shorted stub (E to F) is  $l_1 = 0.09\lambda$  (Example 2-14).

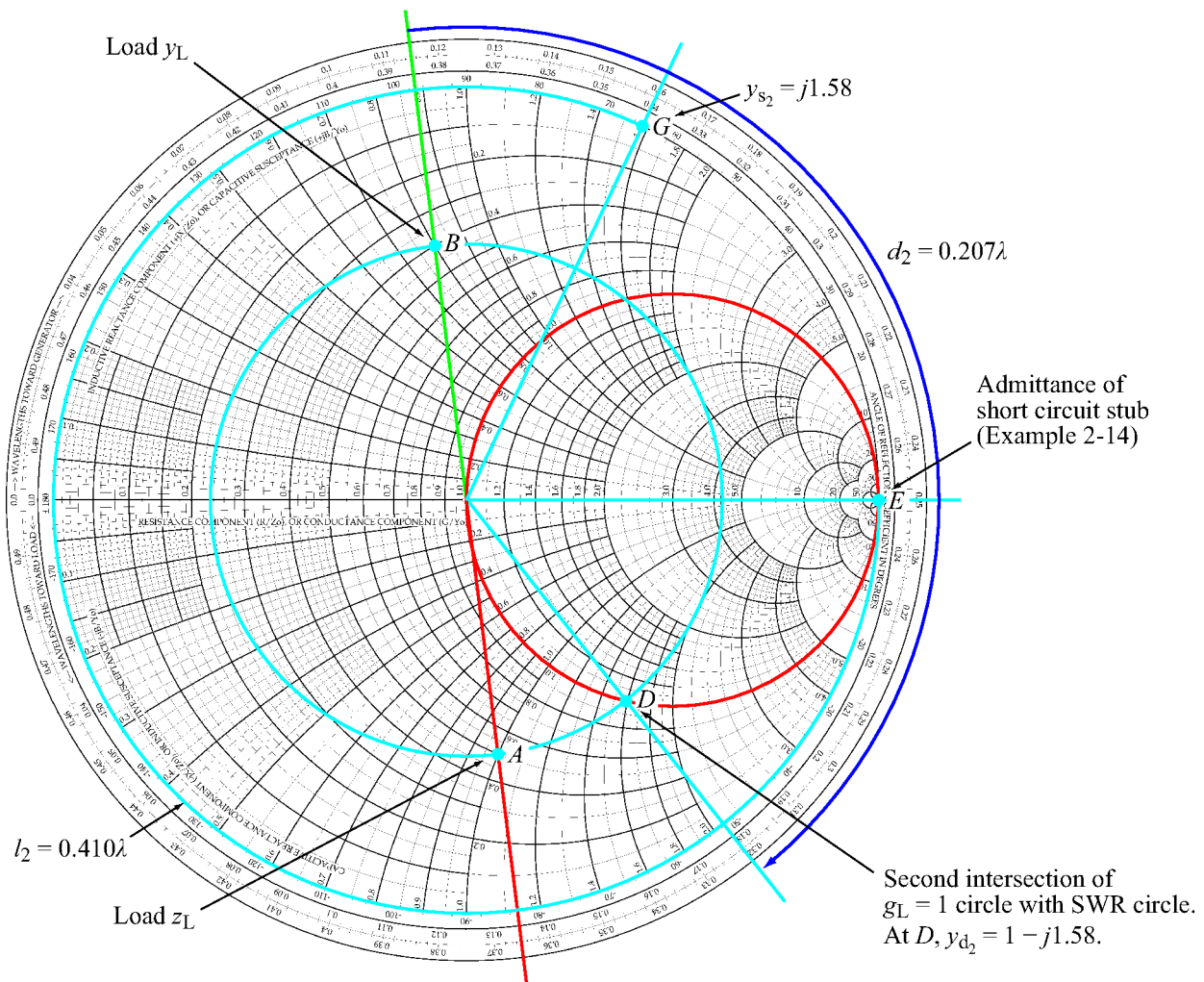


**Figure 2-37:** Solution for point D of Examples 2-13 and 2-14. Point D is the second point of intersection of the SWR circle and the  $g_L = 1$  circle. The distance B to D gives  $d_2 = 0.207\lambda$ , and the distance E to G gives  $l_2 = 0.410\lambda$  (Example 2-14).

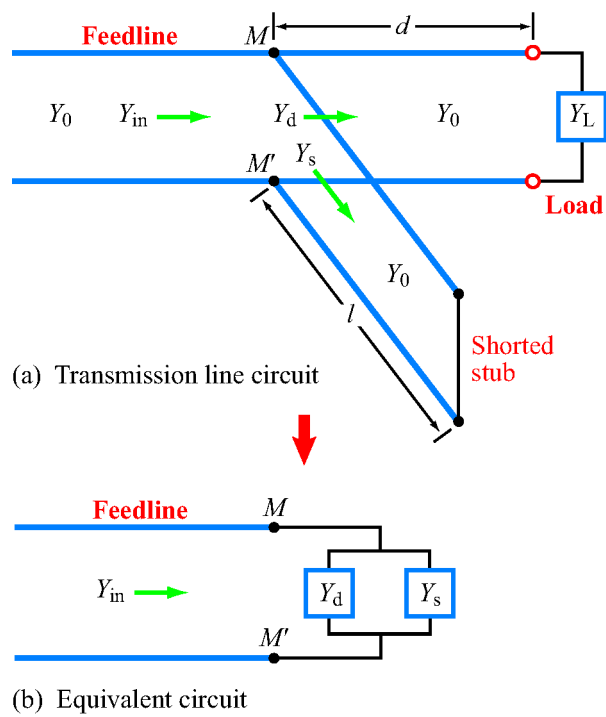


**Figure 2-38:** Shorted-stub matching network.

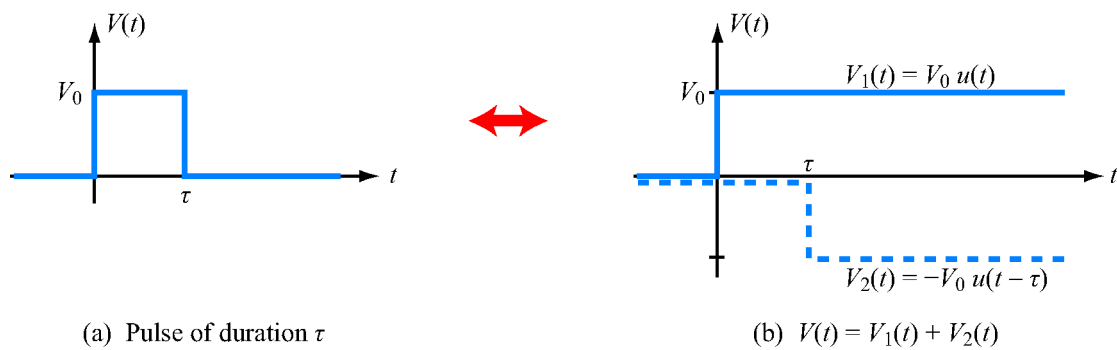
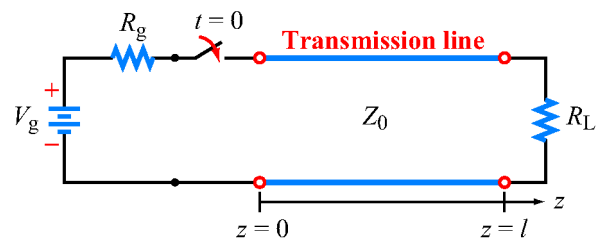
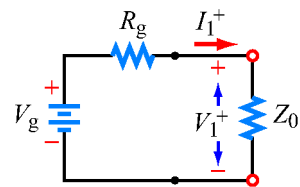


**Figure 2-39:** A rectangular pulse  $V(t)$  of duration  $\tau$  can be represented as the sum of two step functions of opposite polarities displaced by  $\tau$  relative to each other.



(a) Transmission-line circuit



(b) Equivalent circuit at  $t = 0^+$

**Figure 2-40:** At  $t = 0^+$ , immediately after closing the switch in the circuit in (a), the circuit can be represented by the equivalent circuit in (b).



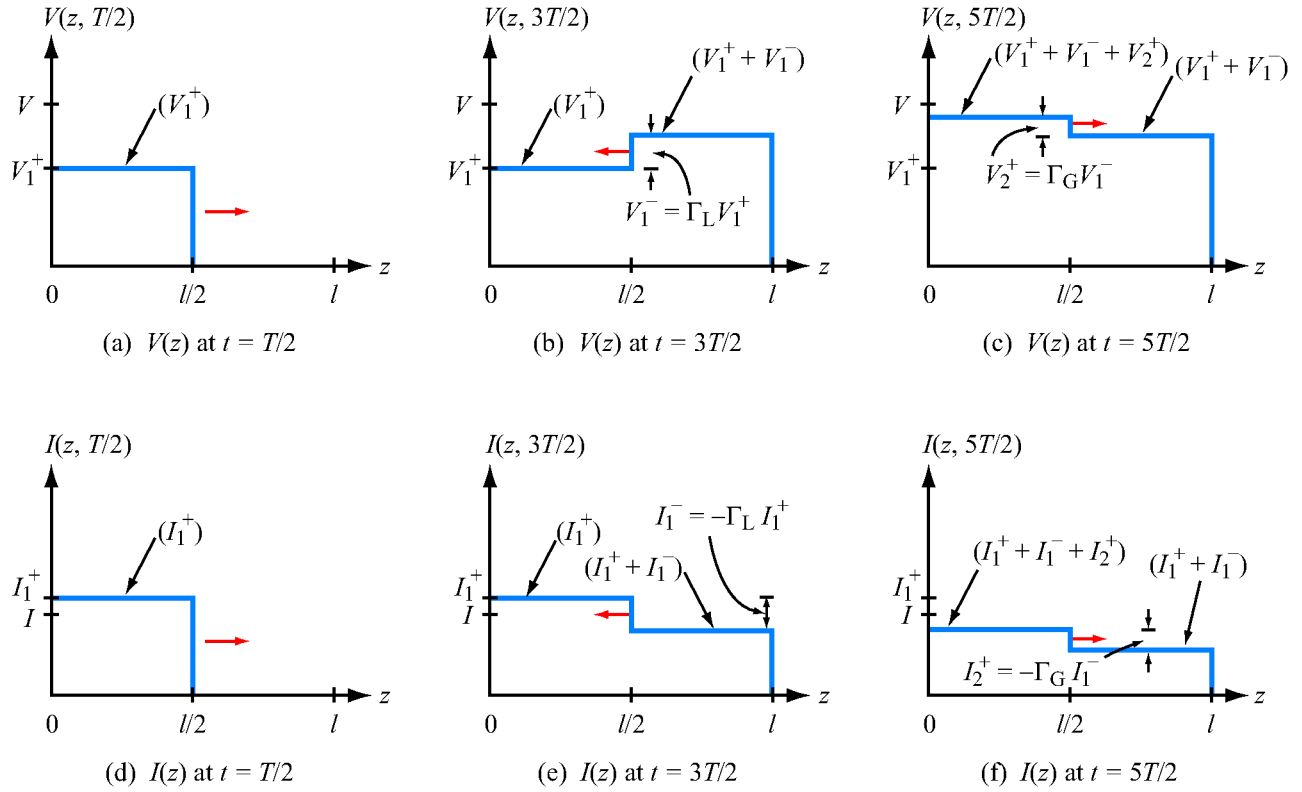


**Figure 2-41:** Voltage and current distributions on a lossless transmission line at  $t = T/2$ ,  $t = 3T/2$ , and  $t = 5T/2$ , due to a unit step voltage applied to a circuit with  $R_g = 4Z_0$  and  $R_L = 2Z_0$ . The corresponding reflection coefficients are  $\Gamma_L = 1/3$  and  $\Gamma_g = 3/5$ .

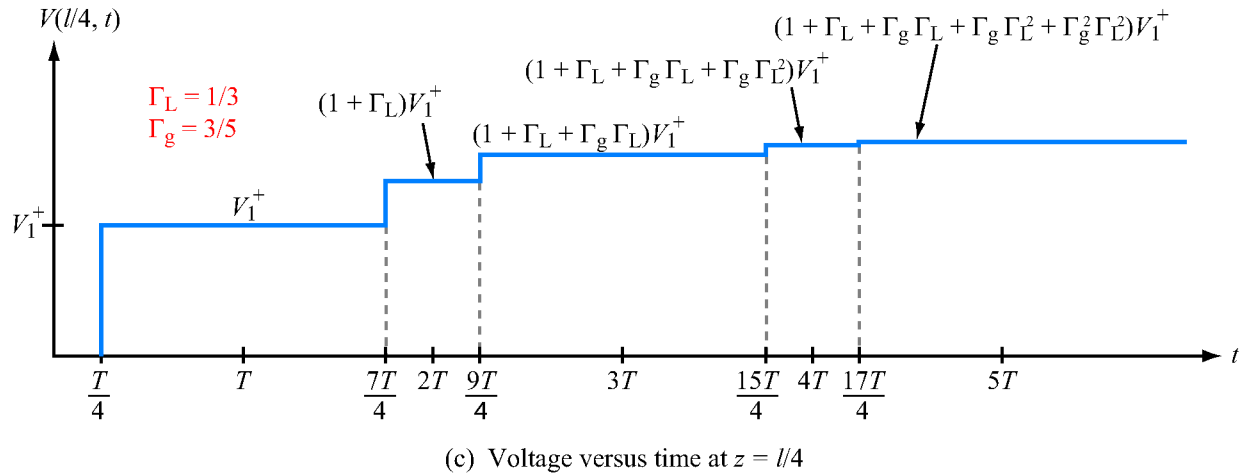
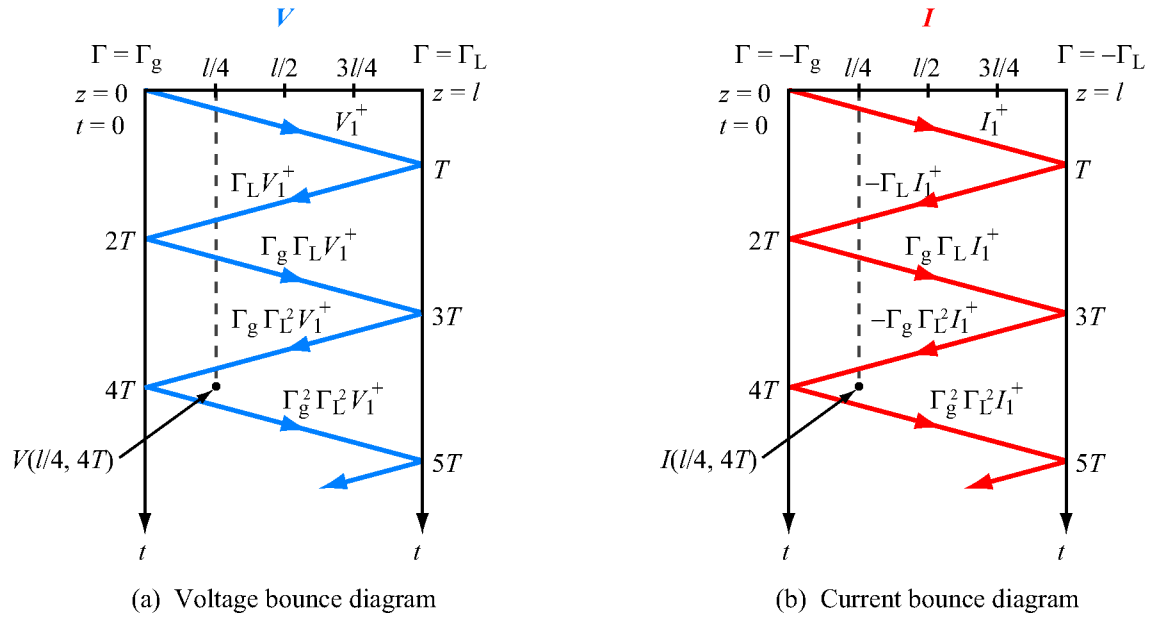


**Figure 2-42:** Bounce diagrams for (a) voltage and (b) current. In (c), the voltage variation with time at  $z = l/4$  for a circuit with  $\Gamma_g = 3/5$  and  $\Gamma_L = 1/3$  is deduced from the vertical dashed line at  $l/4$  in (a).

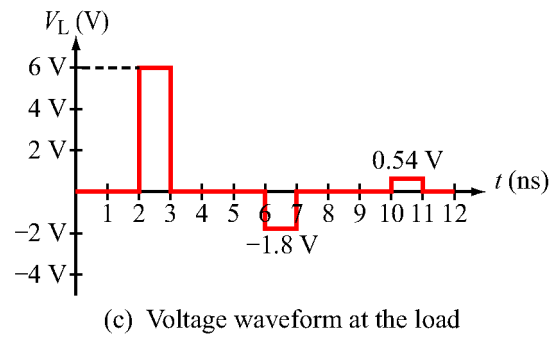
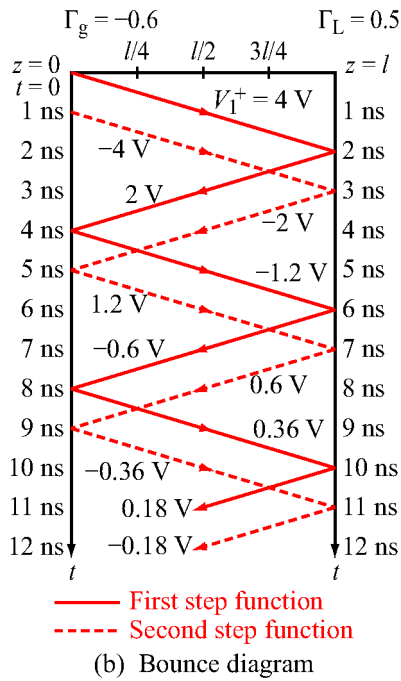
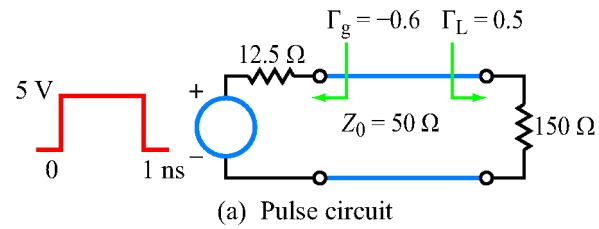
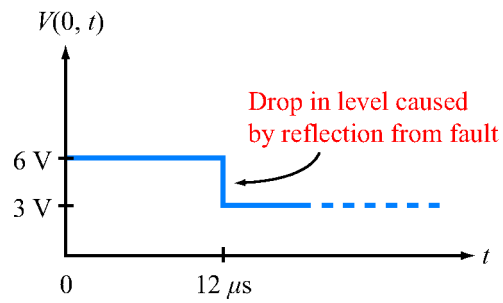
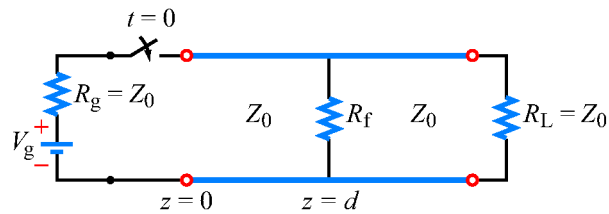


**Figure 2-43:** Example 2-15.



(a) Observed voltage at the sending end



(b) The fault at  $z = d$  is represented by a fault resistance  $R_f$

**Figure 2-44:** Time-domain reflectometer of Example 2-16.

## Chapter 3 Figures

**Figure 3-1** Vector  $\mathbf{A} = \hat{\mathbf{a}}A$  has magnitude  $A = |\mathbf{A}|$  and points in the direction of unit vector  $\hat{\mathbf{a}} = \mathbf{A}/A$ .

**Figure 3-2** Cartesian coordinate system: (a) base vectors  $\hat{\mathbf{x}}$ ,  $\hat{\mathbf{y}}$ , and  $\hat{\mathbf{z}}$ , and (b) components of vector  $\mathbf{A}$ .

**Figure 3-3** Vector addition by (a) the parallelogram rule and (b) the head-to-tail rule.

**Figure 3-4** Distance vector  $\mathbf{R}_{12} = \overrightarrow{P_1P_2} = \mathbf{R}_2 - \mathbf{R}_1$ , where  $\mathbf{R}_1$  and  $\mathbf{R}_2$  are the position vectors of points  $P_1$  and  $P_2$ , respectively.

**Figure 3-5** The angle  $\theta_{AB}$  is the angle between  $\mathbf{A}$  and  $\mathbf{B}$ , measured from  $\mathbf{A}$  to  $\mathbf{B}$  between vector tails. The dot product is positive if  $0 \leq \theta_{AB} < 90^\circ$ , as in (a), and it is negative if  $90^\circ < \theta_{AB} \leq 180^\circ$ , as in (b).

**Figure 3-6** Cross product  $\mathbf{A} \times \mathbf{B}$  points in the direction  $\hat{\mathbf{n}}$ , which is perpendicular to the plane containing  $\mathbf{A}$  and  $\mathbf{B}$  and defined by the right-hand rule.

**Figure 3-7** Geometry of Example 3-1.

**Figure 3-8** Differential length, area, and volume in Cartesian coordinates.

**Figure 3-9** Point  $P(r_1, \phi_1, z_1)$  in cylindrical coordinates;  $r_1$  is the radial distance from the origin in the  $x$ - $y$  plane,  $\phi_1$  is the angle in the  $x$ - $y$  plane measured from the  $x$ -axis toward the  $y$ -axis, and  $z_1$  is the vertical distance from the  $x$ - $y$  plane.

**Figure 3-10** Differential areas and volume in cylindrical coordinates.

**Figure 3-11** Geometry of Example 3-3.

**Figure 3-12** Cylindrical surface of Example 3-4.

**Figure 3-13** Point  $P(R_1, \theta_1, \phi_1)$  in spherical coordinates.

**Figure 3-14** Differential volume in spherical coordinates.

**Figure 3-15** Spherical strip of Example 3-5.

**Figure 3-16** Interrelationships between Cartesian coordinates  $(x, y, z)$  and cylindrical coordinates  $(r, \phi, z)$ .

**Figure 3-17** Interrelationships between base vectors  $(\hat{\mathbf{x}}, \hat{\mathbf{y}})$  and  $(\hat{\mathbf{r}}, \hat{\boldsymbol{\phi}})$ .

**Figure 3-18** Interrelationships between  $(x, y, z)$  and  $(R, \theta, \phi)$ .

**Figure 3-19** Differential distance vector  $d\mathbf{l}$  between points  $P_1$  and  $P_2$ .

**Figure 3-20** Flux lines of the electric field  $\mathbf{E}$  due to a positive charge  $q$ .

**Figure 3-21** Flux lines of a vector field  $\mathbf{E}$  passing through a differential rectangular parallelepiped of volume  $\Delta v = \Delta x \Delta y \Delta z$ .

**Figure 3-22** Circulation is zero for the uniform field in (a), but it is not zero for the azimuthal field in (b).

**Figure 3-23** The direction of the unit vector  $\hat{\mathbf{n}}$  is along the thumb when the other four fingers of the right hand follow  $d\mathbf{l}$ .

**Figure 3-24** Geometry of Example 3-12.

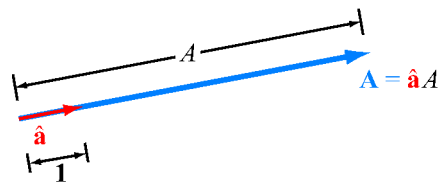
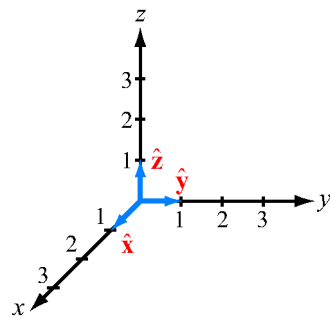
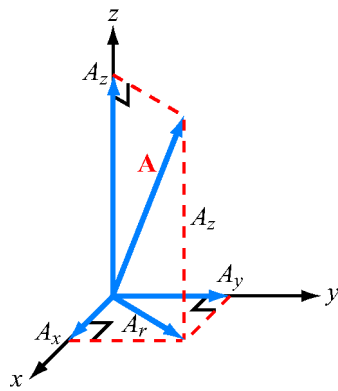


**Figure 3-1:** Vector  $\mathbf{A} = \hat{\mathbf{a}}A$  has magnitude  $A = |\mathbf{A}|$  and points in the direction of unit vector  $\hat{\mathbf{a}} = \mathbf{A}/A$ .



(a) Base vectors



(b) Components of  $\mathbf{A}$

**Figure 3-2:** Cartesian coordinate system: (a) base vectors  $\hat{\mathbf{x}}$ ,  $\hat{\mathbf{y}}$ , and  $\hat{\mathbf{z}}$ , and (b) components of vector  $\mathbf{A}$ .



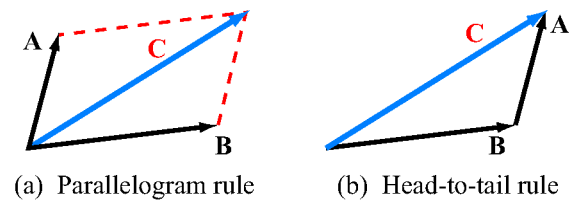


**Figure 3-3:** Vector addition by (a) the parallelogram rule and (b) the head-to-tail rule.

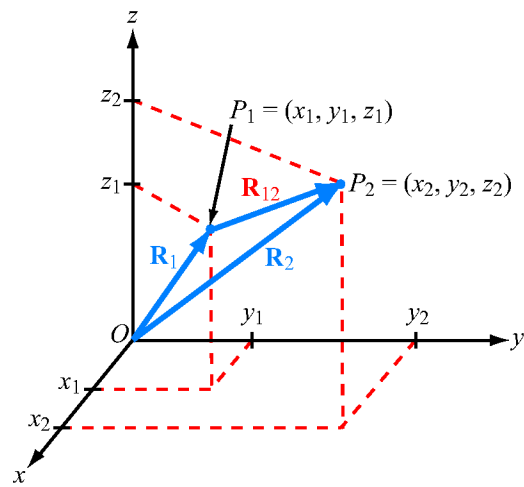


**Figure 3-4:** Distance vector  $\mathbf{R}_{12} = \overrightarrow{P_1 P_2} = \mathbf{R}_2 - \mathbf{R}_1$ , where  $\mathbf{R}_1$  and  $\mathbf{R}_2$  are the position vectors of points  $P_1$  and  $P_2$ , respectively.

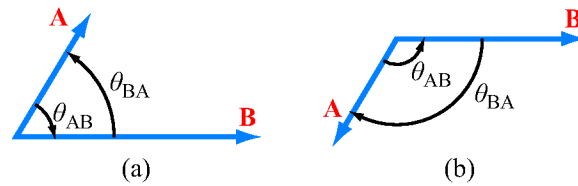
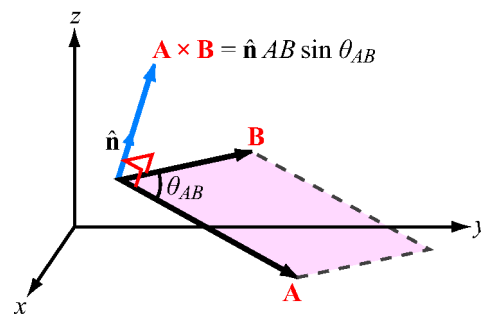
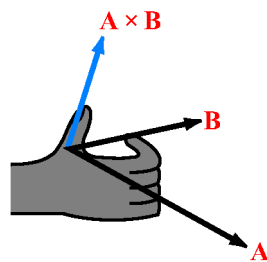


**Figure 3-5:** The angle  $\theta_{AB}$  is the angle between  $\mathbf{A}$  and  $\mathbf{B}$ , measured from  $\mathbf{A}$  to  $\mathbf{B}$  between vector tails. The dot product is positive if  $0 \leq \theta_{AB} < 90^\circ$ , as in (a), and it is negative if  $90^\circ < \theta_{AB} \leq 180^\circ$ , as in (b).



(a) Cross product



(b) Right-hand rule

**Figure 3-6:** Cross product  $\mathbf{A} \times \mathbf{B}$  points in the direction  $\hat{\mathbf{n}}$ , which is perpendicular to the plane containing  $\mathbf{A}$  and  $\mathbf{B}$  and defined by the right-hand rule.

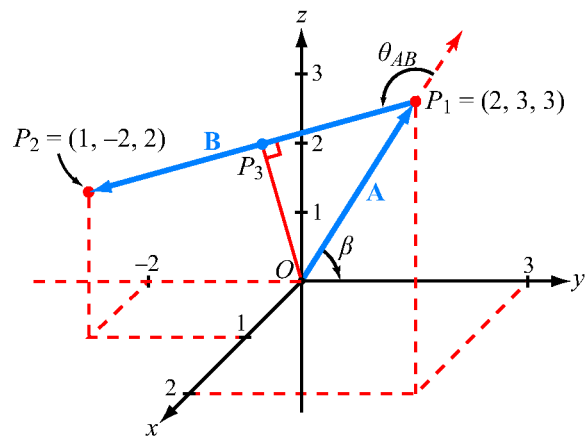


**Figure 3-7:** Geometry of Example 3-1.

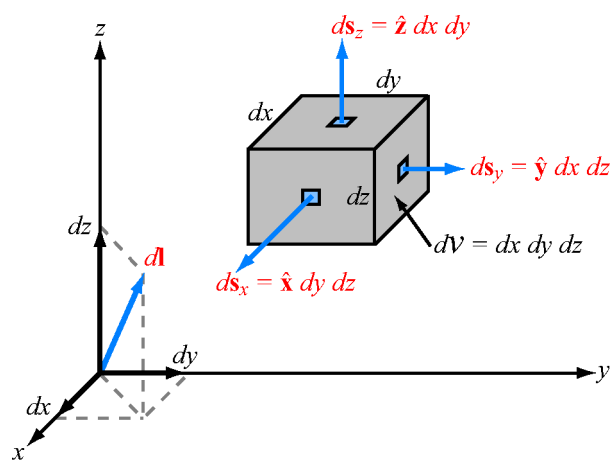


**Figure 3-8:** Differential length, area, and volume in Cartesian coordinates.

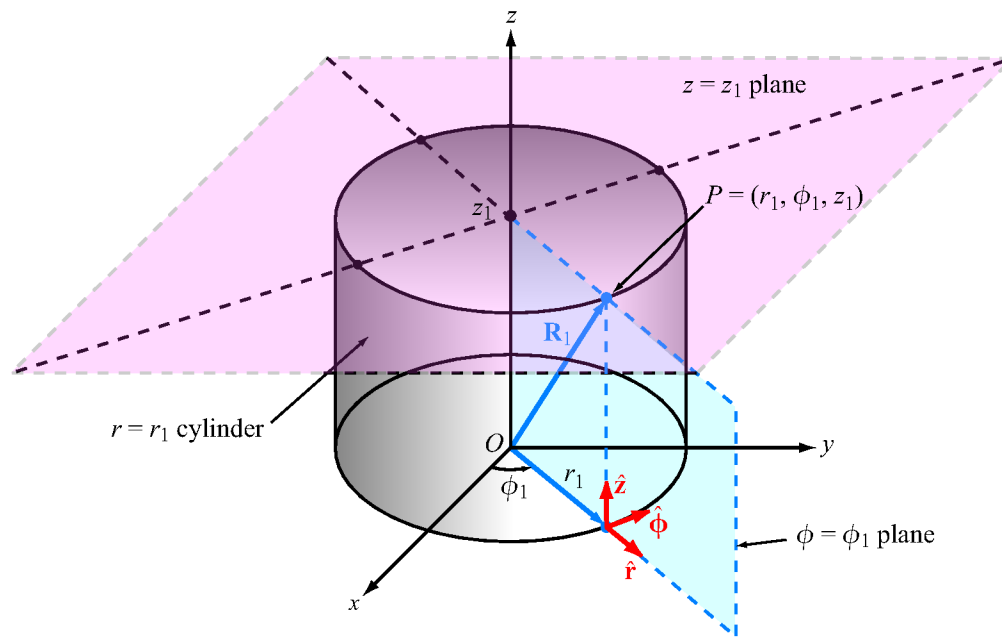


**Figure 3-9:** Point  $P(r_1, \phi_1, z_1)$  in cylindrical coordinates;  $r_1$  is the radial distance from the origin in the  $x$ - $y$  plane,  $\phi_1$  is the angle in the  $x$ - $y$  plane measured from the  $x$ -axis toward the  $y$ -axis, and  $z_1$  is the vertical distance from the  $x$ - $y$  plane.

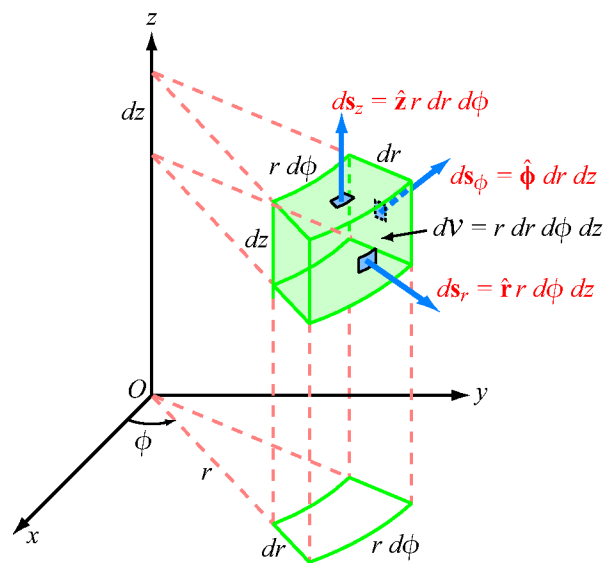


**Figure 3-10:** Differential areas and volume in cylindrical coordinates.



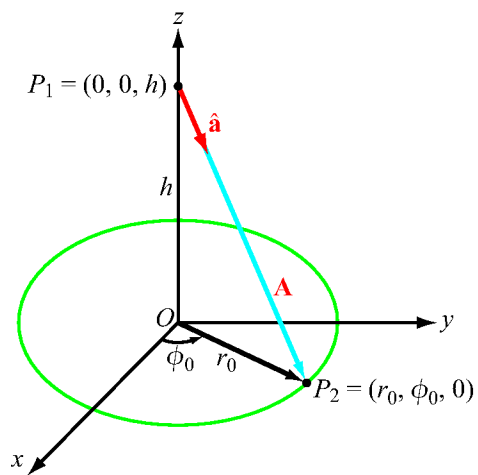


**Figure 3-11:** Geometry of Example 3-3.

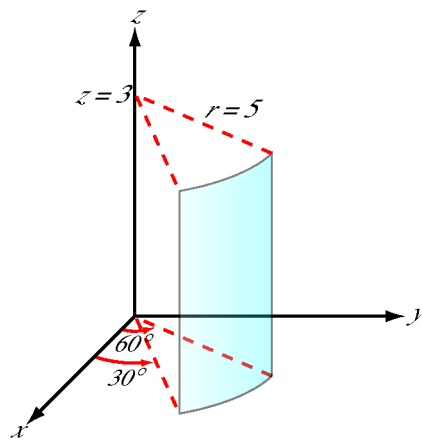


**Figure 3-12:** Cylindrical surface of Example 3-4.

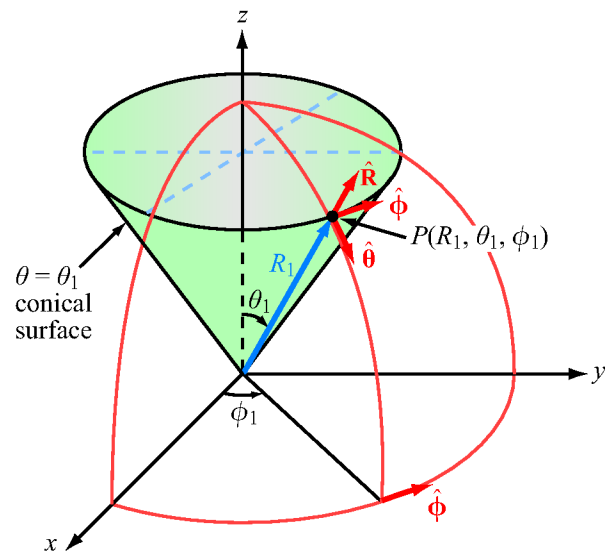


**Figure 3-13:** Point  $P(R_1, \theta_1, \phi_1)$  in spherical coordinates.

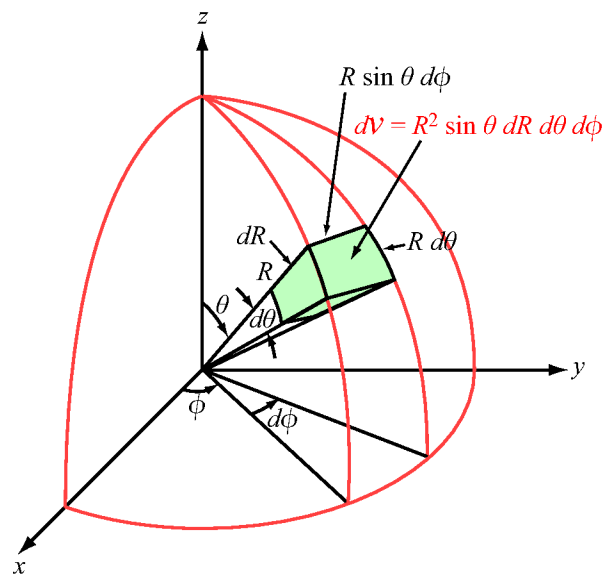


**Figure 3-14:** Differential volume in spherical coordinates.

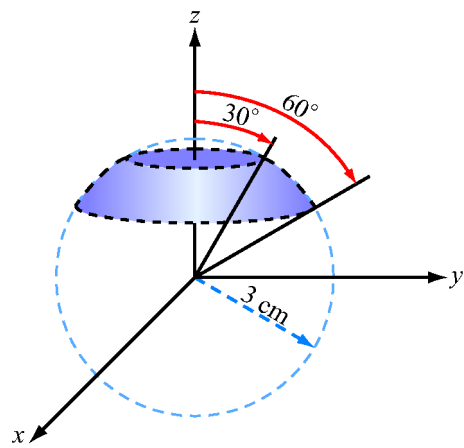


**Figure 3-15:** Spherical strip of Example 3-5.

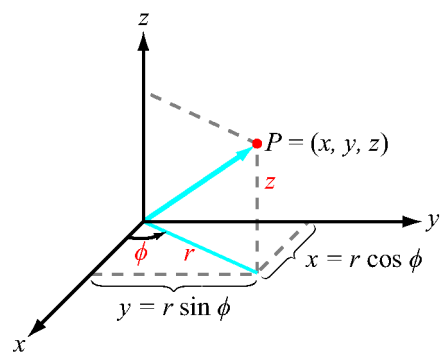


**Figure 3-16:** Interrelationships between Cartesian coordinates  $(x, y, z)$  and cylindrical coordinates  $(r, \phi, z)$ .

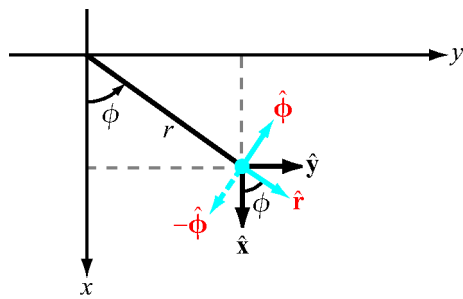


**Figure 3-17:** Interrelationships between base vectors  $(\hat{\mathbf{x}}, \hat{\mathbf{y}})$  and  $(\hat{\mathbf{r}}, \hat{\phi})$ .

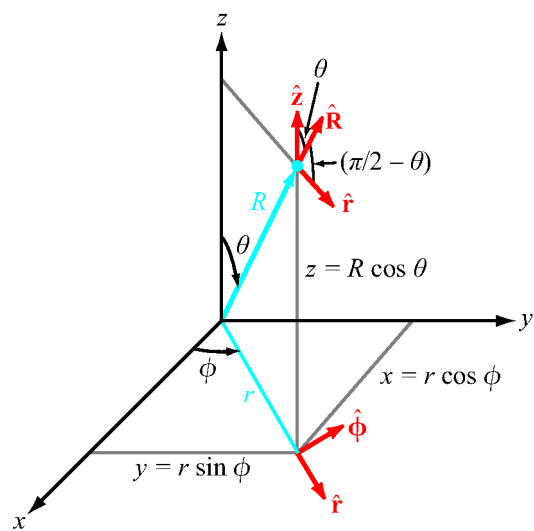


**Figure 3-18:** Interrelationships between  $(x, y, z)$  and  $(R, \theta, \phi)$ .



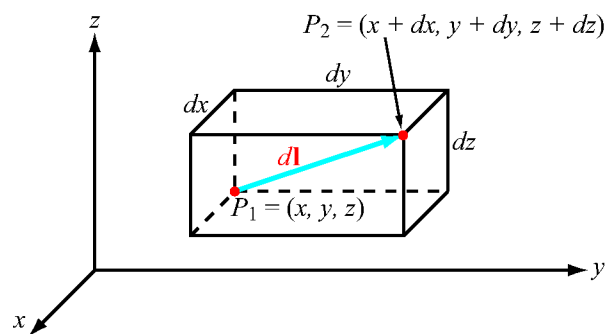


**Figure 3-19:** Differential distance vector  $d\mathbf{l}$  between points  $P_1$  and  $P_2$ .

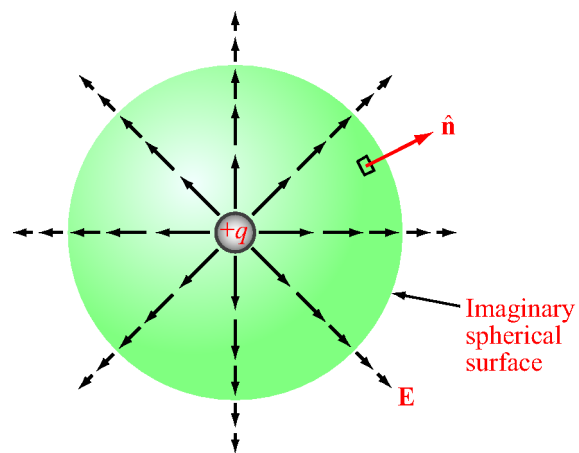


**Figure 3-20:** Flux lines of the electric field  $\mathbf{E}$  due to a positive charge  $q$ .

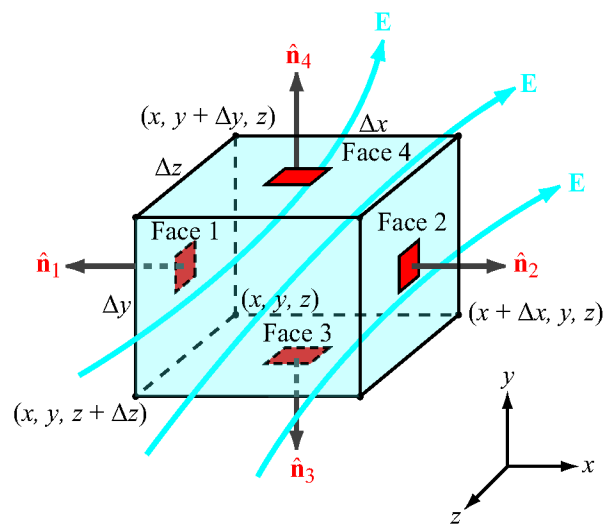
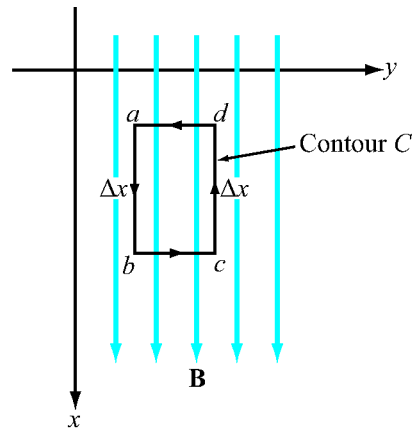
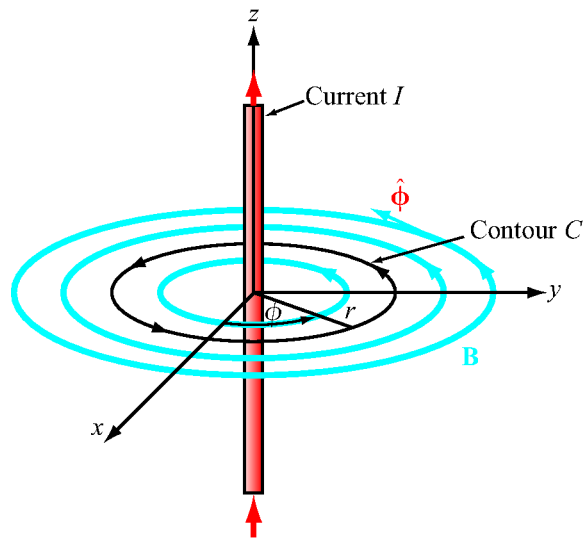


**Figure 3-21:** Flux lines of a vector field  $\mathbf{E}$  passing through a differential rectangular parallelepiped of volume  $\Delta v = \Delta x \Delta y \Delta z$ .



(a) Uniform field



(b) Azimuthal field

**Figure 3-22:** Circulation is zero for the uniform field in (a), but it is not zero for the azimuthal field in (b).

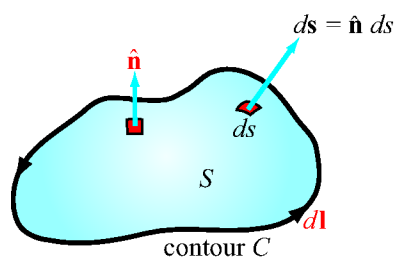


**Figure 3-23:** The direction of the unit vector  $\hat{n}$  is along the thumb when the other four fingers of the right hand follow  $d\mathbf{l}$ .

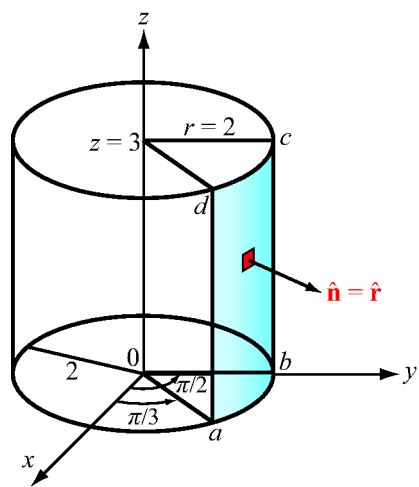


**Figure 3-24:** Geometry of Example 3-12.

## Chapter 4 Figures

**Figure 4-1** Charge distributions for Examples 4-1 and 4-2.

**Figure 4-2** Charges with velocity  $\mathbf{u}$  moving through a cross section  $\Delta s'$  in (a) and  $\Delta s$  in (b).

**Figure 4-3** Electric-field lines due to a charge  $q$ .

**Figure 4-4** The electric field  $\mathbf{E}$  at  $P$  due to two charges is equal to the vector sum of  $\mathbf{E}_1$  and  $\mathbf{E}_2$ .

**Figure 4-5** Electric field due to a volume charge distribution.

**Figure 4-6** Ring of charge with line density  $\rho_\ell$ . (a) The field  $d\mathbf{E}_1$  due to infinitesimal segment 1 and (b) the fields  $d\mathbf{E}_1$  and  $d\mathbf{E}_2$  due to segments at diametrically opposite locations (Example 4-4).

**Figure 4-7** Circular disk of charge with surface charge density  $\rho_s$ . The electric field at  $P = (0, 0, h)$  points along the  $z$ -direction (Example 4-5).

**Figure 4-8** The integral form of Gauss's law states that the outward flux of  $\mathbf{D}$  through a surface is proportional to the enclosed charge  $Q$ .

**Figure 4-9** Electric field  $\mathbf{D}$  due to point charge  $q$ .

**Figure 4-10** Gaussian surface around an infinitely long line of charge (Example 4-6).

**Figure 4-11** Work done in moving a charge  $q$  a distance  $dy$  against the electric field  $\mathbf{E}$  is  $dW = qE dy$ .

**Figure 4-12** In electrostatics, the potential difference between  $P_2$  and  $P_1$  is the same irrespective of the path used for calculating the line integral of the electric field between them.

**Figure 4-13** Electric dipole with dipole moment  $\mathbf{p} = q\mathbf{d}$  (Example 4-7).

**Figure 4-14** Linear resistor of cross section  $A$  and length  $l$  connected to a dc voltage source  $V$ .

**Figure 4-15** Coaxial cable of Example 4-9.

**Figure 4-16** In the absence of an external electric field  $\mathbf{E}$ , the center of the electron cloud is co-located with the center of the nucleus, but when a field is applied, the two centers are separated by a distance  $d$ .

**Figure 4-17** A dielectric medium polarized by an external electric field  $\mathbf{E}$ .

**Figure 4-18** Interface between two dielectric media.

**Figure 4-19** Application of boundary conditions at the interface between two dielectric media (Example 4-10).

**Figure 4-20** When a conducting slab is placed in an external electric field  $\mathbf{E}_1$ , charges that accumulate on the conductor surfaces induce an internal electric field  $\mathbf{E}_i = -\mathbf{E}_1$ . Consequently, the total field inside the conductor is zero.

**Figure 4-21** Metal sphere placed in an external electric field  $\mathbf{E}_0$ .

**Figure 4-22** Boundary between two conducting media.

**Figure 4-23** A dc voltage source connected to a capacitor composed of two conducting bodies.

**Figure 4-24** A dc voltage source connected to a parallel-plate capacitor (Example 4-11).

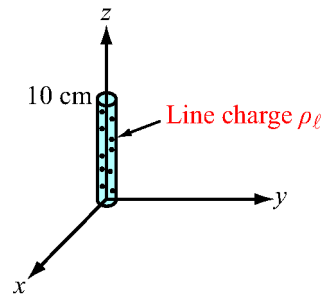
**Figure 4-25** Coaxial capacitor filled with insulating material of permittivity  $\epsilon$  (Example 4-12).

**Figure 4-26** By image theory, a charge  $Q$  above a grounded perfectly conducting plane is equivalent to  $Q$  and its image  $-Q$  with the ground plane removed.

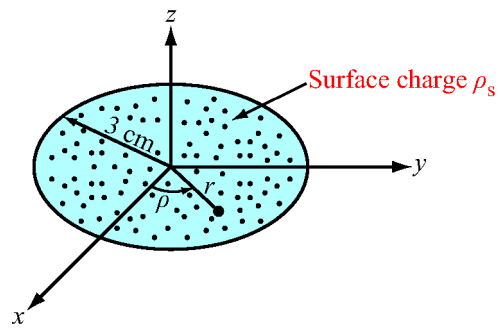
**Figure 4-27** Charge distributions above a conducting plane and their image-method equivalents.

**Figure 4-28** Application of the image method for finding  $\mathbf{E}$  at point  $P$  (Example 4-13).





(a) Line charge distribution



(b) Surface charge distribution

**Figure 4-1:** Charge distributions for Examples 4-1 and 4-2.

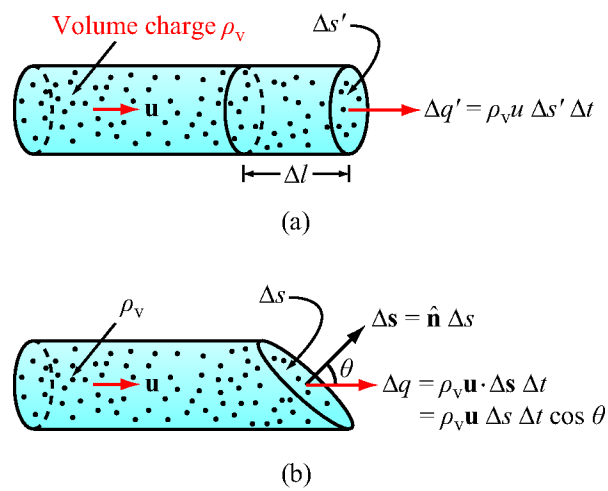


**Figure 4-2:** Charges with velocity  $\mathbf{u}$  moving through a cross section  $\Delta s'$  in (a) and  $\Delta s$  in (b).

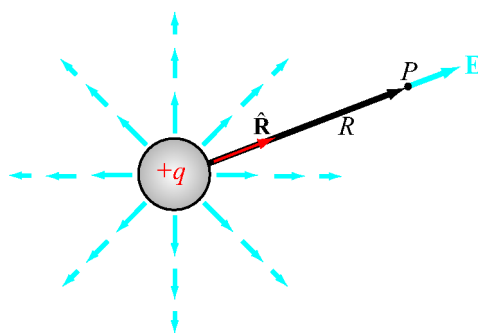


**Figure 4-3:** Electric-field lines due to a charge  $q$ .

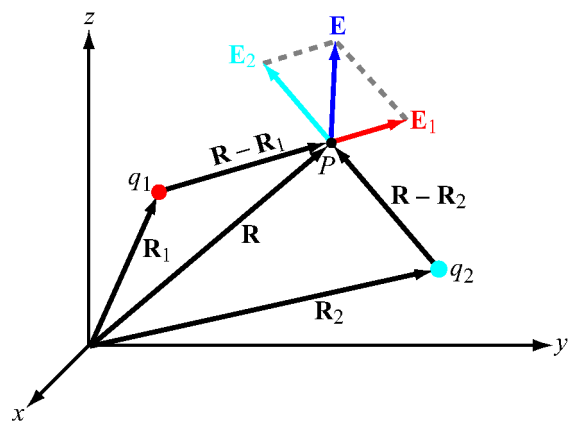


**Figure 4-4:** The electric field  $\mathbf{E}$  at  $P$  due to two charges is equal to the vector sum of  $\mathbf{E}_1$  and  $\mathbf{E}_2$ .

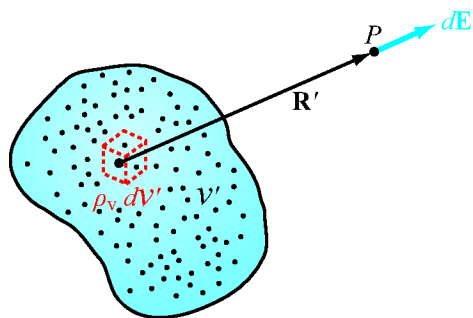


**Figure 4-5:** Electric field due to a volume charge distribution.

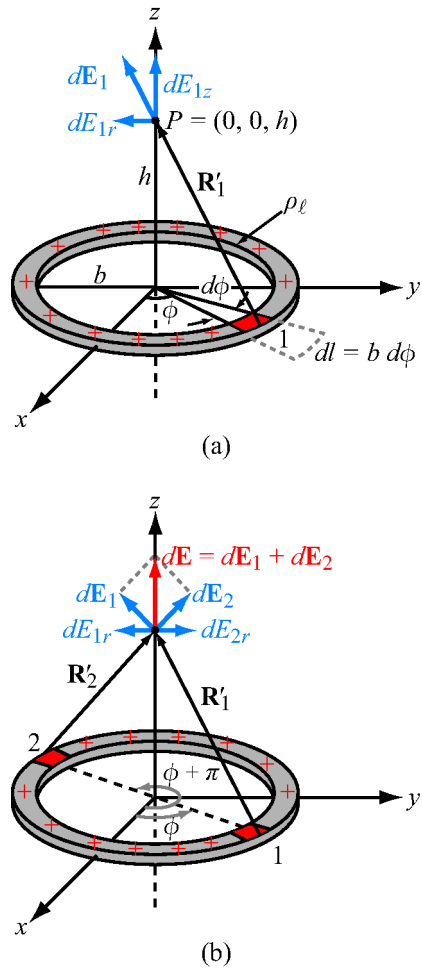


**Figure 4-6:** Ring of charge with line density  $\rho_\ell$ . (a) The field  $d\mathbf{E}_1$  due to infinitesimal segment 1 and (b) the fields  $d\mathbf{E}_1$  and  $d\mathbf{E}_2$  due to segments at diametrically opposite locations (Example 4-4).

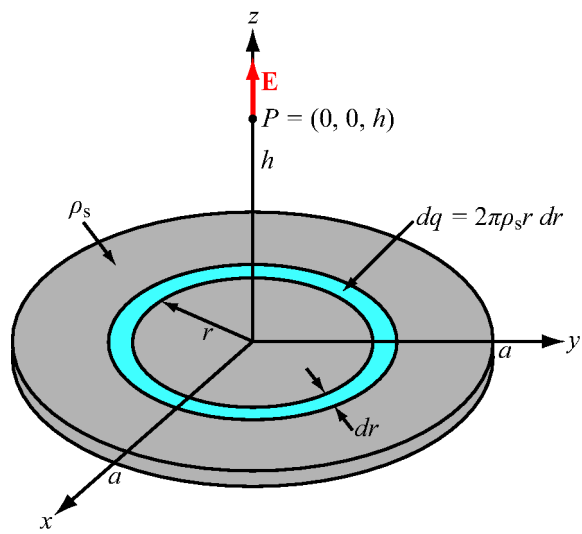


**Figure 4-7:** Circular disk of charge with surface charge density  $\rho_s$ . The electric field at  $P = (0, 0, h)$  points along the  $z$ -direction (Example 4-5).

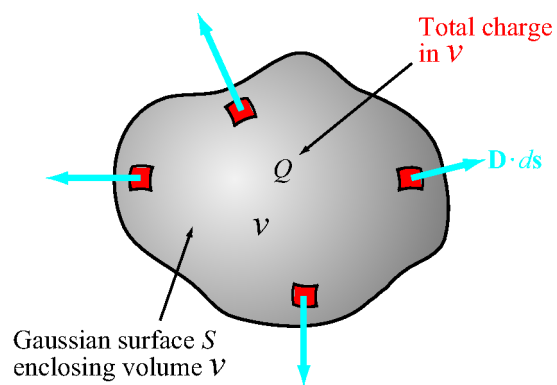


**Figure 4-8:** The integral form of Gauss's law states that the outward flux of  $\mathbf{D}$  through a surface is proportional to the enclosed charge  $Q$ .



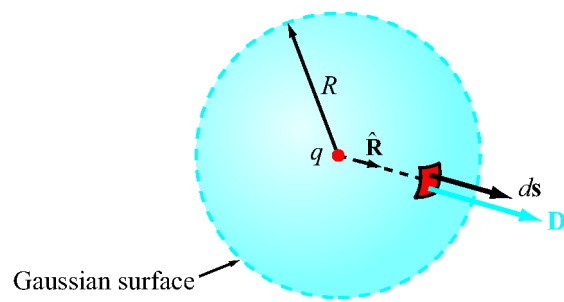


**Figure 4-9:** Electric field  $\mathbf{D}$  due to point charge  $q$ .

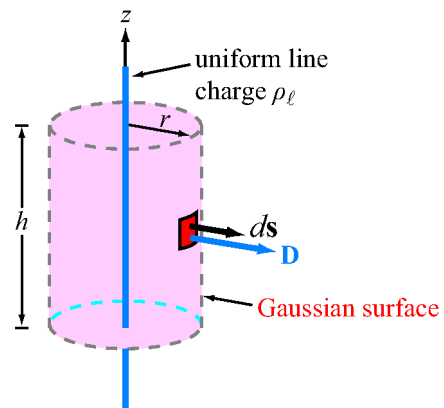


**Figure 4-10:** Gaussian surface around an infinitely long line of charge (Example 4-6).

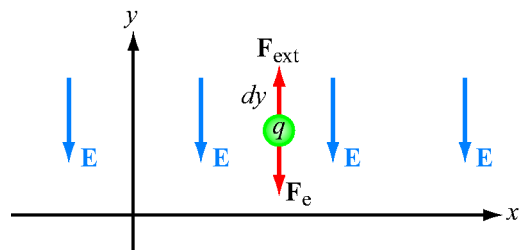


**Figure 4-11:** Work done in moving a charge  $q$  a distance  $dy$  against the electric field  $\mathbf{E}$  is  $dW = qE \, dy$ .

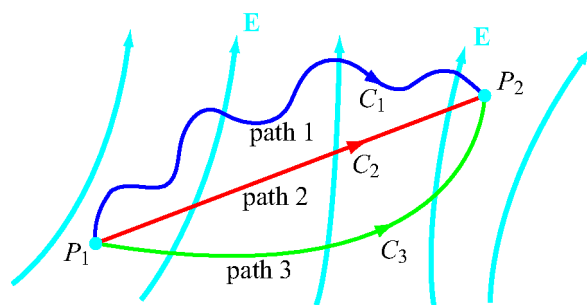
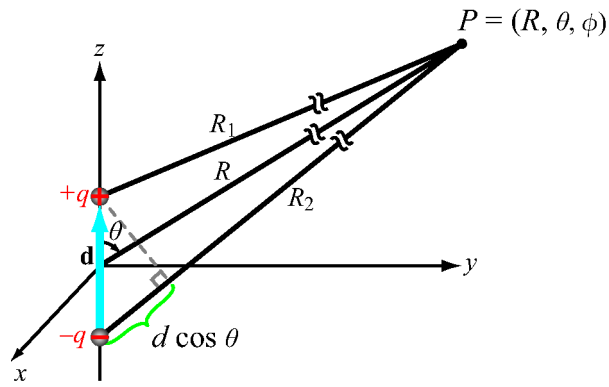
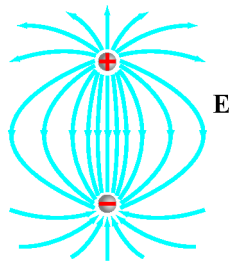


**Figure 4-12:** In electrostatics, the potential difference between  $P_2$  and  $P_1$  is the same irrespective of the path used for calculating the line integral of the electric field between them.



(a) Electric dipole



(b) Electric-field pattern

**Figure 4-13:** Electric dipole with dipole moment  $\mathbf{p} = q\mathbf{d}$  (Example 4-7).

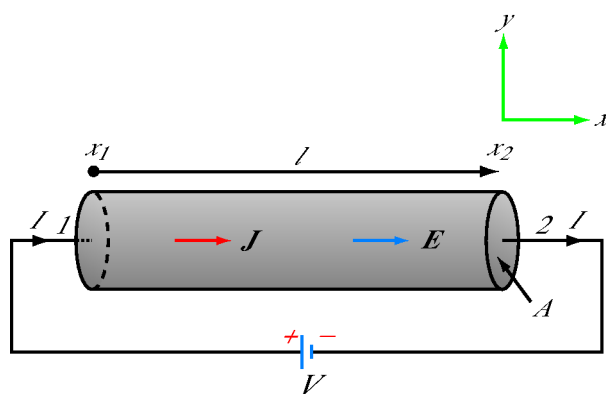


**Figure 4-14:** Linear resistor of cross section  $A$  and length  $l$  connected to a dc voltage source  $V$ .

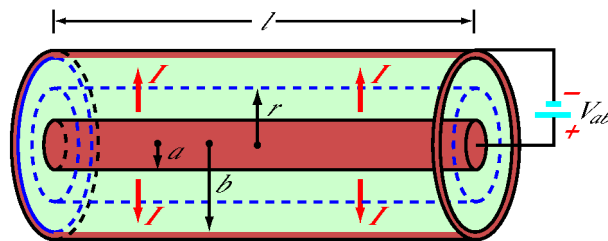


**Figure 4-15:** Coaxial cable of Example 4-9.

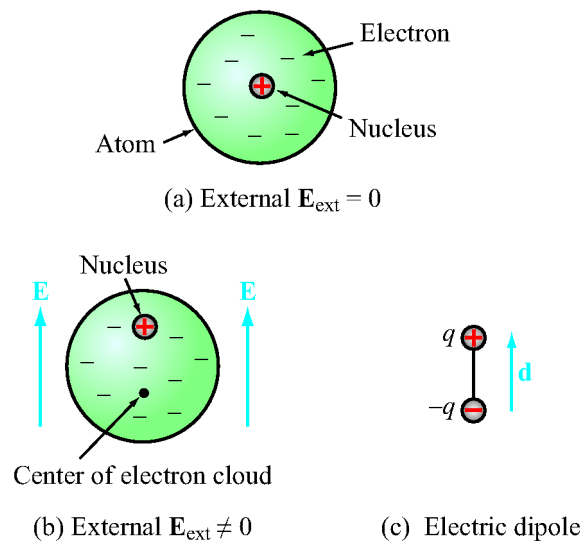


**Figure 4-16:** In the absence of an external electric field  $\mathbf{E}$ , the center of the electron cloud is co-located with the center of the nucleus, but when a field is applied, the two centers are separated by a distance  $d$ .



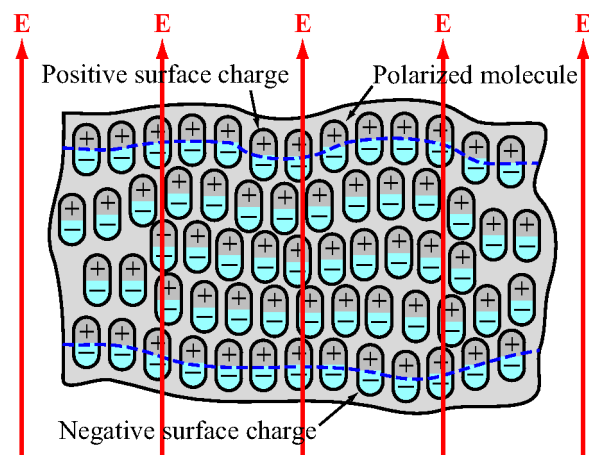


**Figure 4-17:** A dielectric medium polarized by an external electric field  $\mathbf{E}$ .

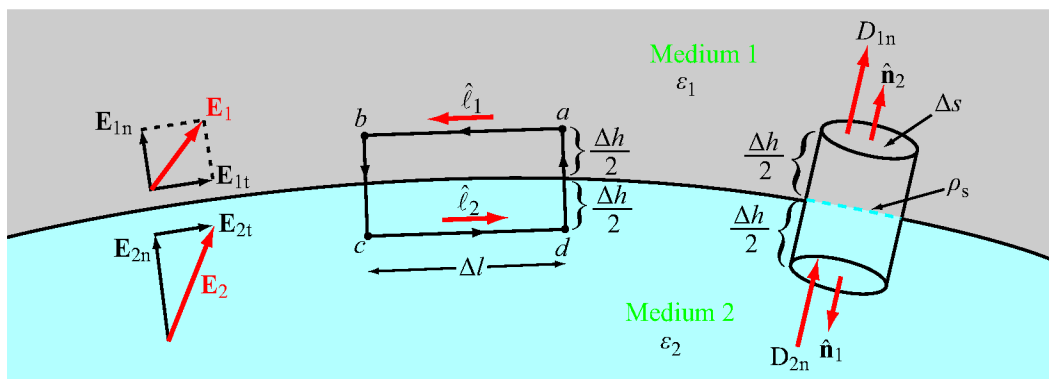


**Figure 4-18:** Interface between two dielectric media.

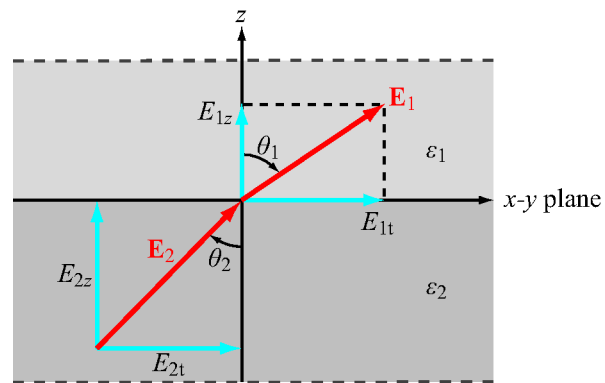


**Figure 4-19:** Application of boundary conditions at the interface between two dielectric media (Example 4-10).

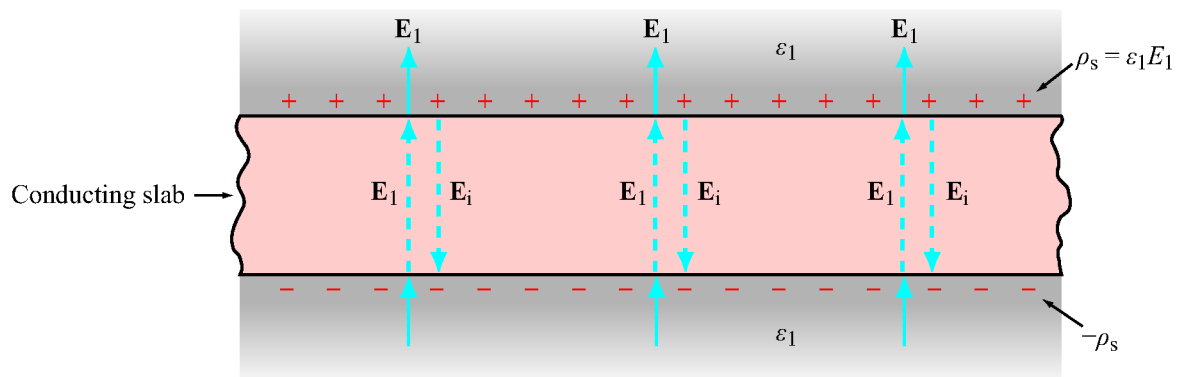


**Figure 4-20:** When a conducting slab is placed in an external electric field  $\mathbf{E}_1$ , charges that accumulate on the conductor surfaces induce an internal electric field  $\mathbf{E}_i = -\mathbf{E}_1$ . Consequently, the total field inside the conductor is zero.

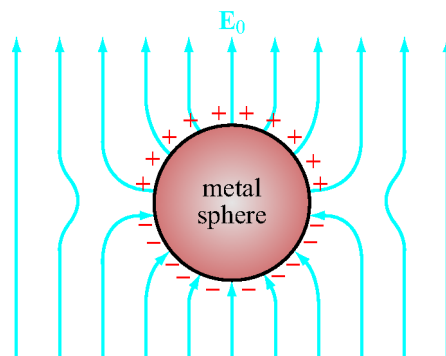


**Figure 4-21:** Metal sphere placed in an external electric field  $E_0$ .

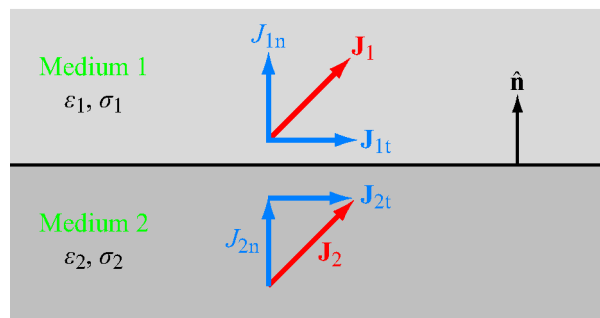


**Figure 4-22:** Boundary between two conducting media.

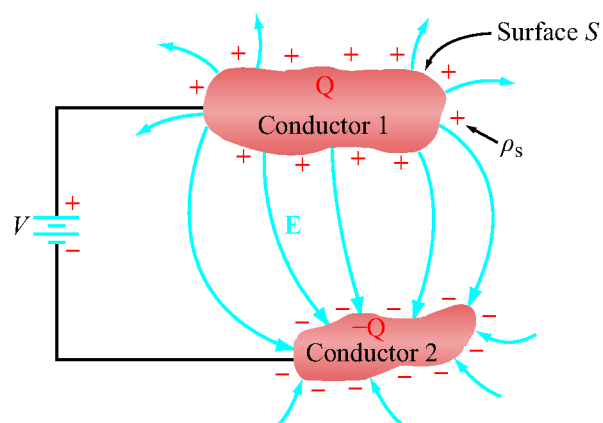


**Figure 4-23:** A dc voltage source connected to a capacitor composed of two conducting bodies.

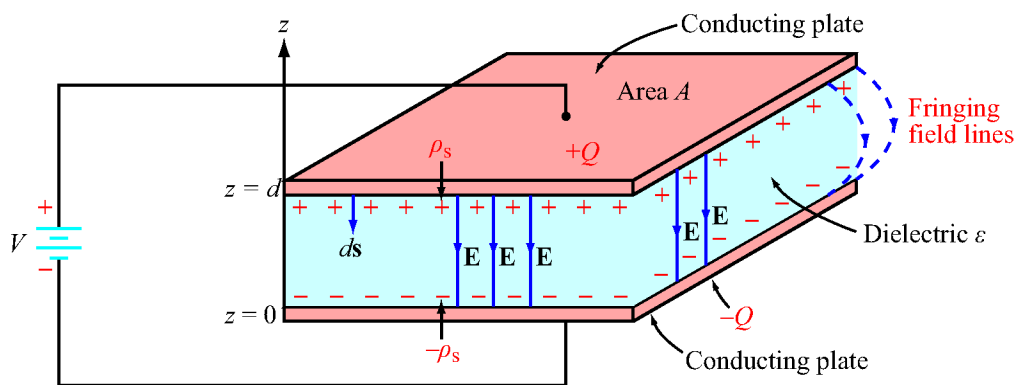


**Figure 4-24:** A dc voltage source connected to a parallel-plate capacitor (Example 4-11).



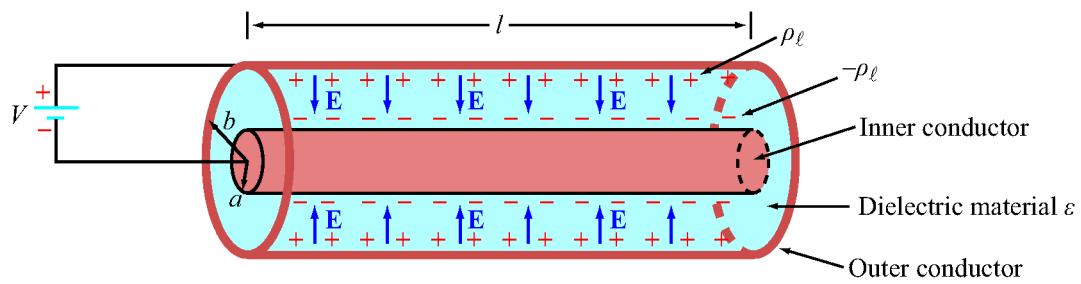


**Figure 4-25:** Coaxial capacitor filled with insulating material of permittivity  $\epsilon$  (Example 4-12).

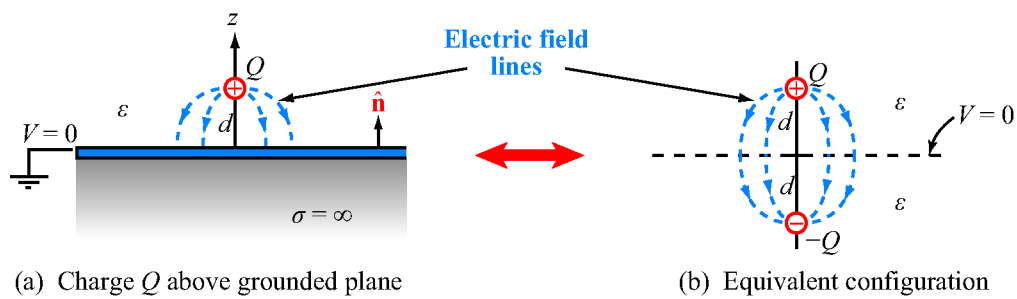
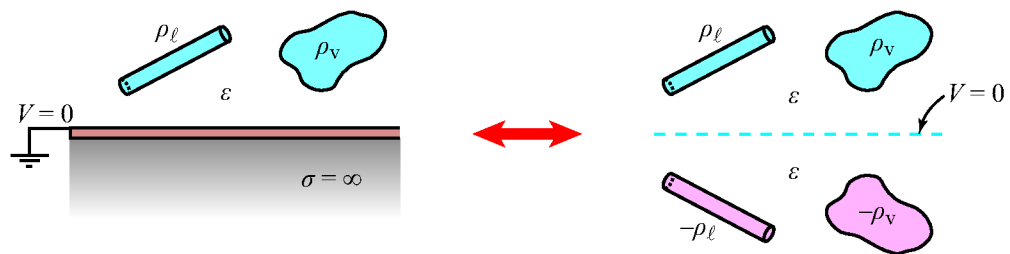


**Figure 4-26:** By image theory, a charge  $Q$  above a grounded perfectly conducting plane is equivalent to  $Q$  and its image  $-Q$  with the ground plane removed.



(a) Charge distributions above ground plane

(b) Equivalent distributions

**Figure 4-27:** Charge distributions above a conducting plane and their image-method equivalents.

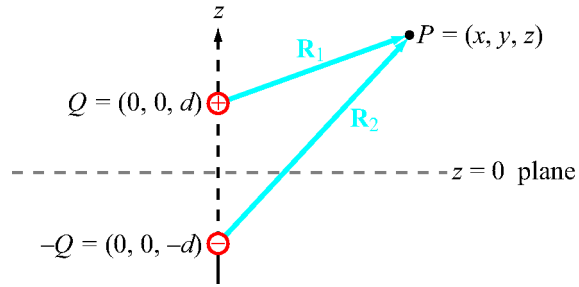


**Figure 4-28:** Application of the image method for finding  $\mathbf{E}$  at point  $P$  (Example 4-13).

## Chapter 5 Figures

**Figure 5-1** The direction of the magnetic force exerted on a charged particle moving in a magnetic field is (a) perpendicular to both  $\mathbf{B}$  and  $\mathbf{u}$  and (b) depends on the charge polarity (positive or negative).

**Figure 5-2** When a slightly flexible vertical wire is placed in a magnetic field directed into the page (as denoted by the crosses), it is (a) not deflected when the current through it is zero, (b) deflected to the left when  $I$  is upward, and (c) deflected to the right when  $I$  is downward.

**Figure 5-3** In a uniform magnetic field, (a) the net force on a closed current loop is zero because the integral of the displacement vector  $d\mathbf{l}$  over a closed contour is zero, and (b) the force on a line segment is proportional to the vector between the end point ( $\mathbf{F}_m = I\boldsymbol{\ell} \times \mathbf{B}$ ).

**Figure 5-4** Semicircular conductor in a uniform field (Example 5-1).

**Figure 5-5** The force  $\mathbf{F}$  acting on a circular disk that can pivot along the  $z$ -axis generates a torque  $\mathbf{T} = \mathbf{d} \times \mathbf{F}$  that causes the disk to rotate.

**Figure 5-6** Rectangular loop pivoted along the  $y$ -axis: (a) front view and (b) bottom view. The combination of forces  $\mathbf{F}_1$  and  $\mathbf{F}_3$  on the loop generates a torque that tends to rotate the loop in a clockwise direction as shown in (b).

**Figure 5-7** Rectangular loop in a uniform magnetic field with flux density  $\mathbf{B}$  whose direction is perpendicular to the rotation axis of the loop, but makes an angle  $\theta$  with the loop's surface normal  $\hat{\mathbf{n}}$ .

**Figure 5-8** Magnetic field  $d\mathbf{H}$  generated by a current element  $I d\mathbf{l}$ . The direction of the field induced at point  $P$  is opposite to that induced at point  $P'$ .

**Figure 5-9** (a) The total current crossing the cross section  $S$  of the cylinder is  $I = \int_S \mathbf{J} \cdot d\mathbf{s}$ . (b) The total current flowing across the surface of the conductor is  $I = \int_l J_s dl$ .

**Figure 5-10** Linear conductor of length  $l$  carrying a current  $I$ . (a) The field  $d\mathbf{H}$  at point  $P$  due to incremental current element  $d\mathbf{l}$ . (b) Limiting angles  $\theta_1$  and  $\theta_2$ , each measured between vector  $I d\mathbf{l}$  and the vector connecting the end of the conductor associated with that angle to point  $P$  (Example 5-2).

**Figure 5-11** Magnetic field surrounding a long, linear current-carrying conductor.

**Figure 5-12** Circular loop carrying a current  $I$  (Example 5-3).

**Figure 5-13** Patterns of (a) the electric field of an electric dipole, (b) the magnetic field of a magnetic dipole, and (c) the magnetic field of a bar magnet. Far away from the sources, the field patterns are similar in all three cases.

**Figure 5-14** Magnetic forces on parallel current-carrying conductors.

**Figure 5-15** Whereas (a) the net electric flux through a closed surface surrounding a charge is not zero, (b) the net magnetic flux through a closed surface surrounding one of the poles of a magnet is zero.

**Figure 5-16** Ampère's law states that the line integral of  $\mathbf{H}$  around a closed contour  $C$  is equal to the current traversing the surface bounded by the contour. This is true for contours (a) and (b), but the line integral of  $\mathbf{H}$  is zero for the contour in (c) because the current  $I$  (denoted by the symbol  $\odot$ ) is not enclosed by the contour  $C$ .

**Figure 5-17** Infinitely long wire of radius  $a$  carrying a uniform current  $I$  along the  $+z$ -direction: (a) general configuration showing contours  $C_1$  and  $C_2$ ; (b) cross-sectional view; and (c) a plot of  $H$  versus  $r$  (Example 5-4).

**Figure 5-18** Toroidal coil with inner radius  $a$  and outer radius  $b$ . The wire loops usually are much more closely spaced than shown in the figure (Example 5-5).

**Figure 5-19** A thin current sheet in the  $x$ - $y$  plane carrying a surface current density  $\mathbf{J}_s = \hat{\mathbf{x}}J_s$  (Example 5-6).

**Figure 5-20** An electron generates (a) an orbital magnetic moment  $\mathbf{m}_o$  as it rotates around the nucleus and (b) a spin magnetic moment  $\mathbf{m}_s$ , as it spins about its own axis.

**Figure 5-21** Comparison of (a) unmagnetized and (b) magnetized domains in a ferromagnetic material.

**Figure 5-22** Typical hysteresis curve for a ferromagnetic material.

**Figure 5-23** Comparison of hysteresis curves for (a) a hard ferromagnetic material and (b) a soft ferromagnetic material.

**Figure 5-24** Boundary between medium 1 with  $\mu_1$  and medium 2 with  $\mu_2$ .

**Figure 5-25** Magnetic field lines of (a) a loosely wound solenoid and (b) a tightly wound solenoid.

**Figure 5-26** Solenoid cross section showing geometry for calculating  $\mathbf{H}$  at a point  $P$  on the solenoid axis.

**Figure 5-27** To compute the inductance per unit length of a two-conductor transmission line, we need to determine the magnetic flux through the area  $S$  between the conductors.

**Figure 5-28** Cross-sectional view of coaxial transmission line (Example 5-7).

**Figure 5-29** Magnetic field lines generated by current  $I_1$  in loop 1 linking surface  $S_2$  of loop 2.

**Figure 5-30** Toroidal coil with two windings used as a transformer.

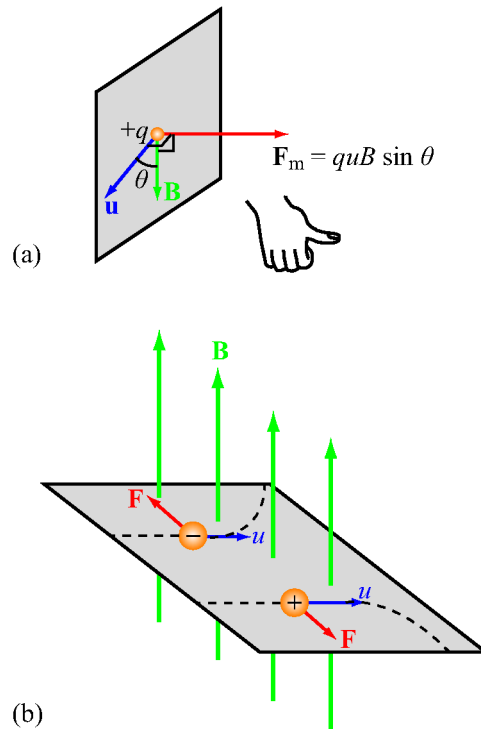


**Figure 5-1:** The direction of the magnetic force exerted on a charged particle moving in a magnetic field is (a) perpendicular to both  $\mathbf{B}$  and  $\mathbf{u}$  and (b) depends on the charge polarity (positive or negative).



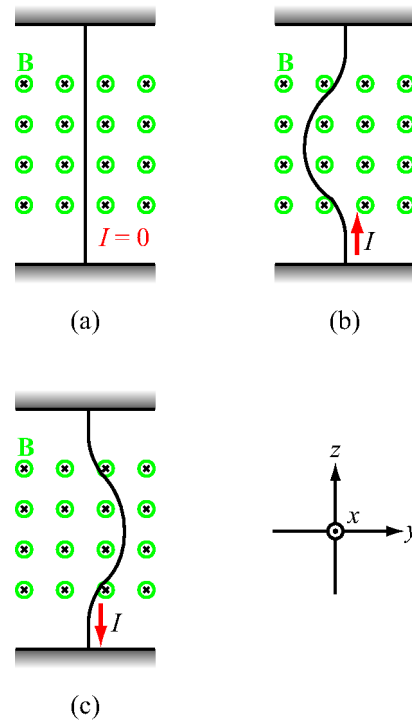


**Figure 5-2:** When a slightly flexible vertical wire is placed in a magnetic field directed into the page (as denoted by the crosses), it is (a) not deflected when the current through it is zero, (b) deflected to the left when  $I$  is upward, and (c) deflected to the right when  $I$  is downward.

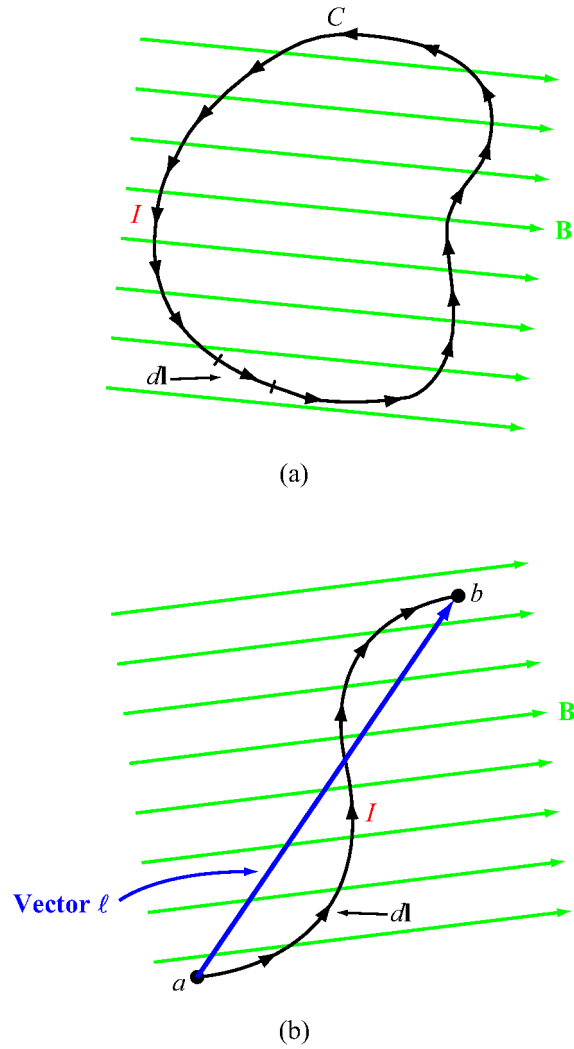


**Figure 5-3:** In a uniform magnetic field, (a) the net force on a closed current loop is zero because the integral of the displacement vector  $d\mathbf{l}$  over a closed contour is zero, and (b) the force on a line segment is proportional to the vector between the end point ( $\mathbf{F}_m = I\boldsymbol{\ell} \times \mathbf{B}$ ).

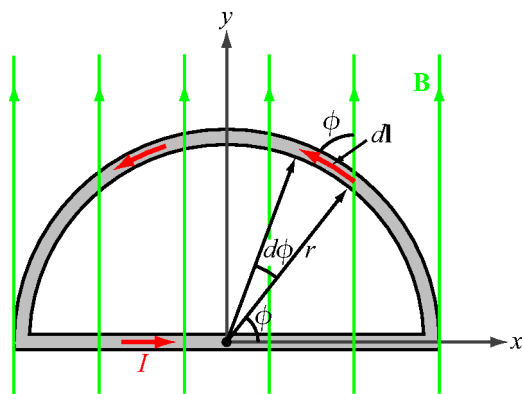


**Figure 5-4:** Semicircular conductor in a uniform field (Example 5-1).

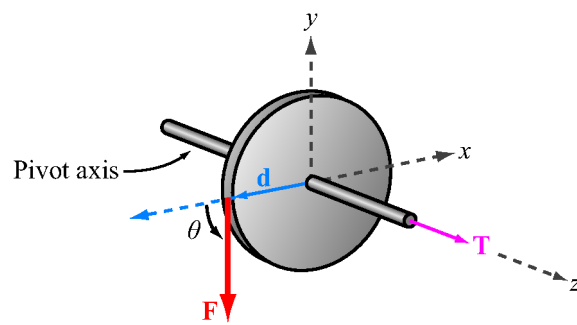


**Figure 5-5:** The force  $\mathbf{F}$  acting on a circular disk that can pivot along the  $z$ -axis generates a torque  $\mathbf{T} = \mathbf{d} \times \mathbf{F}$  that causes the disk to rotate.

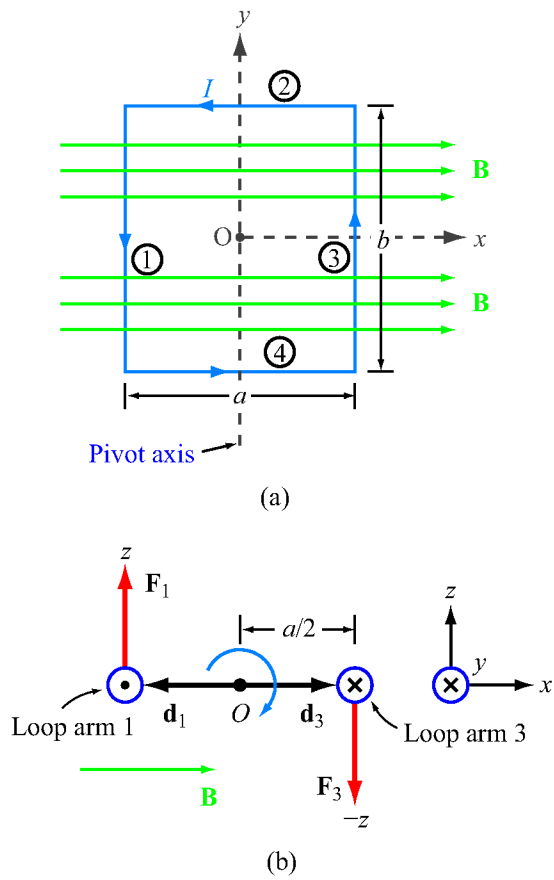
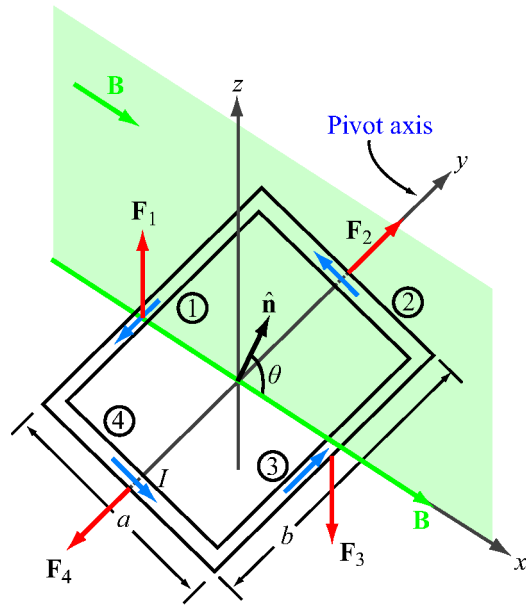
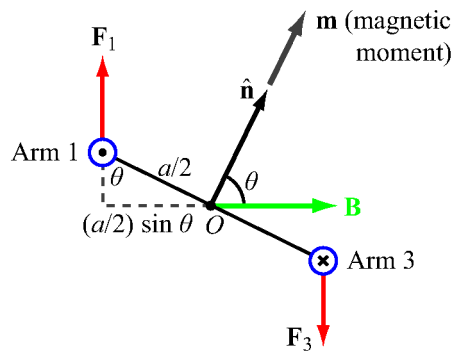


**Figure 5-6:** Rectangular loop pivoted along the  $y$ -axis: (a) front view and (b) bottom view. The combination of forces  $\mathbf{F}_1$  and  $\mathbf{F}_3$  on the loop generates a torque that tends to rotate the loop in a clockwise direction as shown in (b).



(a)



(b)

**Figure 5-7:** Rectangular loop in a uniform magnetic field with flux density  $\mathbf{B}$  whose direction is perpendicular to the rotation axis of the loop, but makes an angle  $\theta$  with the loop's surface normal  $\hat{\mathbf{n}}$ .

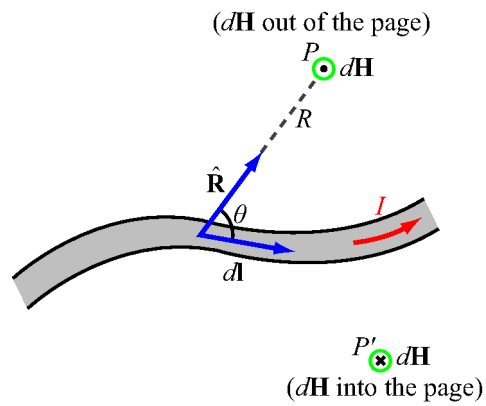
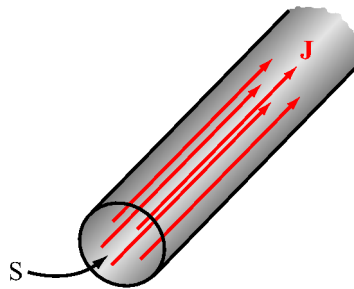
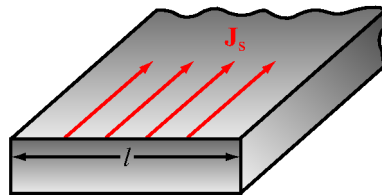


**Figure 5-8:** Magnetic field  $d\mathbf{H}$  generated by a current element  $I d\mathbf{l}$ . The direction of the field induced at point  $P$  is opposite to that induced at point  $P'$ .



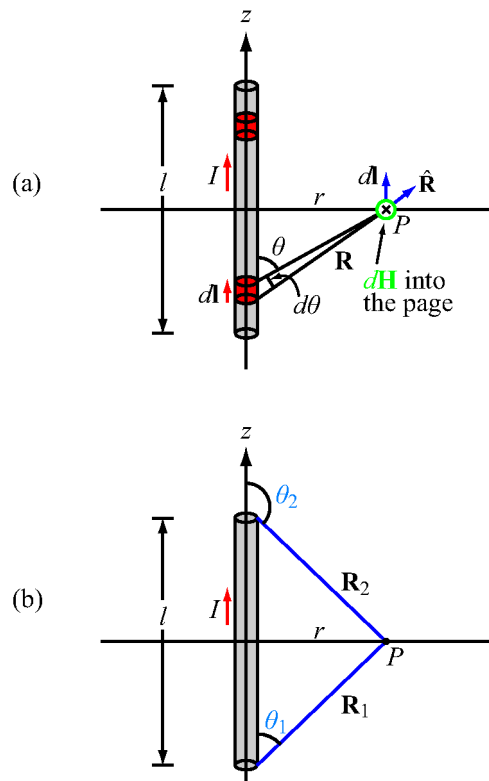
(a) Volume current density  $\mathbf{J}$  in A/m<sup>2</sup>



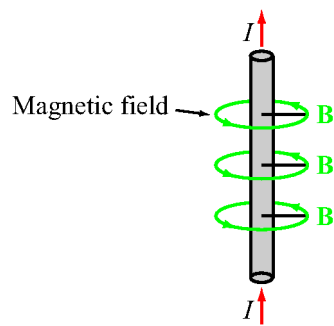
(b) Surface current density  $\mathbf{J}_s$  in A/m

**Figure 5-9:** (a) The total current crossing the cross section  $S$  of the cylinder is  $I = \int_S \mathbf{J} \cdot d\mathbf{s}$ . (b) The total current flowing across the surface of the conductor is  $I = \int_l J_s dl$ .

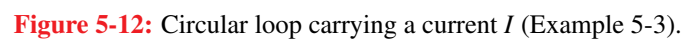




**Figure 5-10:** Linear conductor of length  $l$  carrying a current  $I$ . (a) The field  $d\mathbf{H}$  at point  $P$  due to incremental current element  $d\mathbf{l}$ . (b) Limiting angles  $\theta_1$  and  $\theta_2$ , each measured between vector  $I d\mathbf{l}$  and the vector connecting the end of the conductor associated with that angle to point  $P$  (Example 5-2).



**Figure 5-11:** Magnetic field surrounding a long, linear current-carrying conductor.



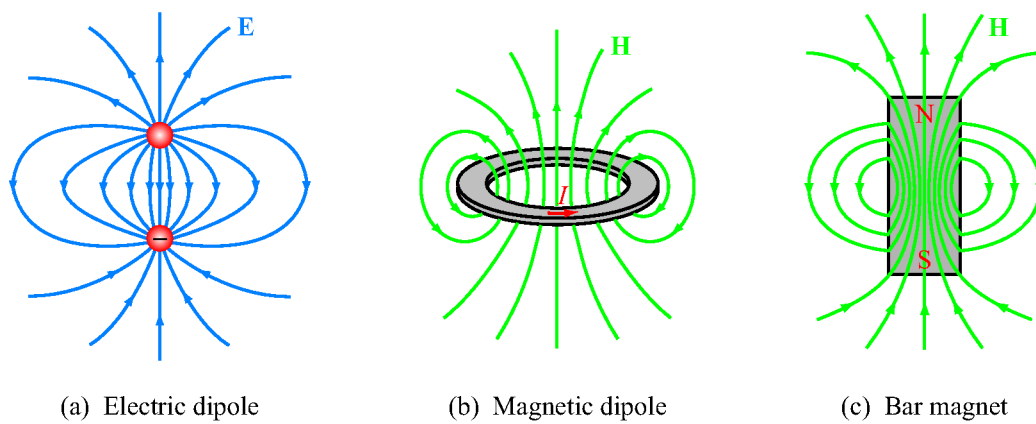


**Figure 5-13:** Patterns of (a) the electric field of an electric dipole, (b) the magnetic field of a magnetic dipole, and (c) the magnetic field of a bar magnet. Far away from the sources, the field patterns are similar in all three cases.

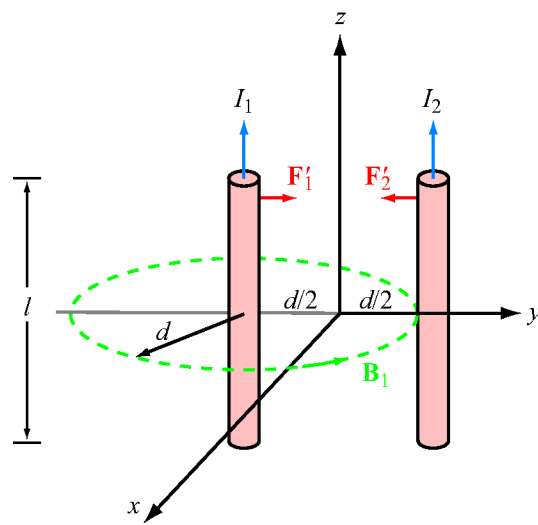


**Figure 5-14:** Magnetic forces on parallel current-carrying conductors.

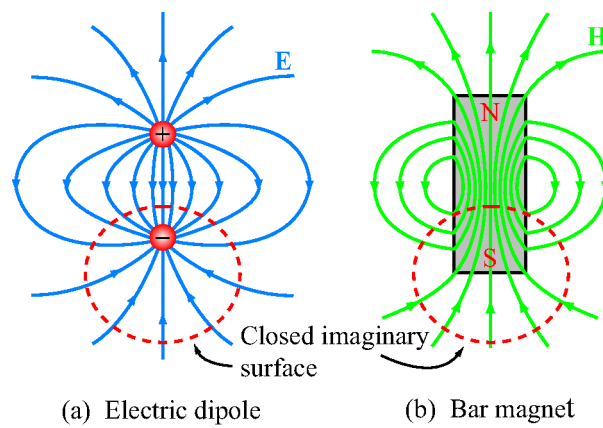


**Figure 5-15:** Whereas (a) the net electric flux through a closed surface surrounding a charge is not zero, (b) the net magnetic flux through a closed surface surrounding one of the poles of a magnet is zero.

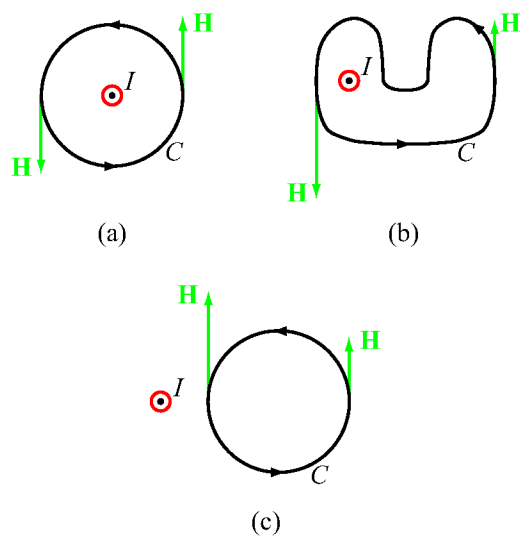
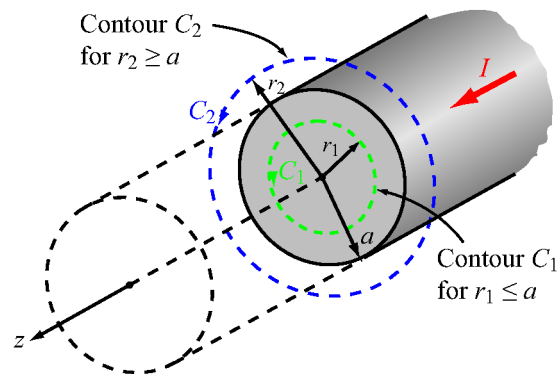
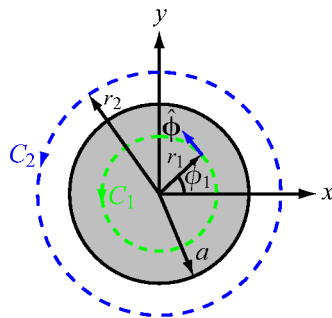


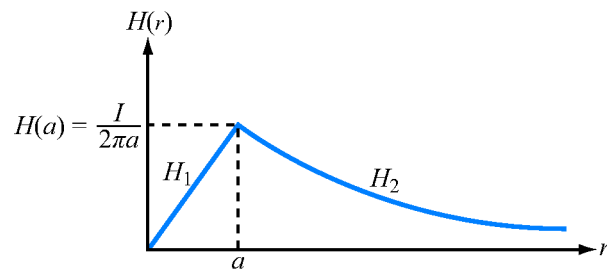
**Figure 5-16:** Ampère's law states that the line integral of  $\mathbf{H}$  around a closed contour  $C$  is equal to the current traversing the surface bounded by the contour. This is true for contours (a) and (b), but the line integral of  $\mathbf{H}$  is zero for the contour in (c) because the current  $I$  (denoted by the symbol  $\odot$ ) is not enclosed by the contour  $C$ .



(a) Cylindrical wire



(b) Wire cross section



(c)

**Figure 5-17:** Infinitely long wire of radius  $a$  carrying a uniform current  $I$  along the  $+z$ -direction: (a) general configuration showing contours  $C_1$  and  $C_2$ ; (b) cross-sectional view; and (c) a plot of  $H$  versus  $r$  (Example 5-4).



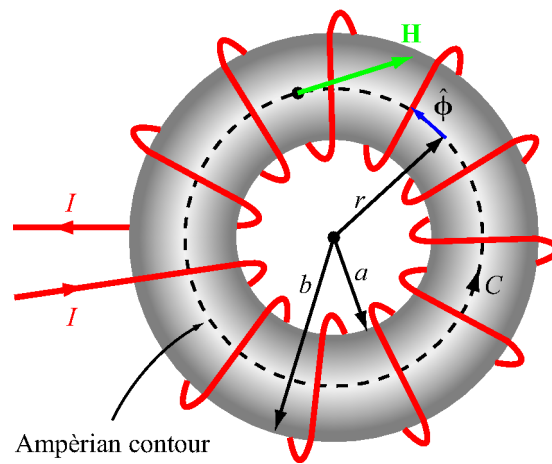


**Figure 5-18:** Toroidal coil with inner radius  $a$  and outer radius  $b$ . The wire loops usually are much more closely spaced than shown in the figure (Example 5-5).

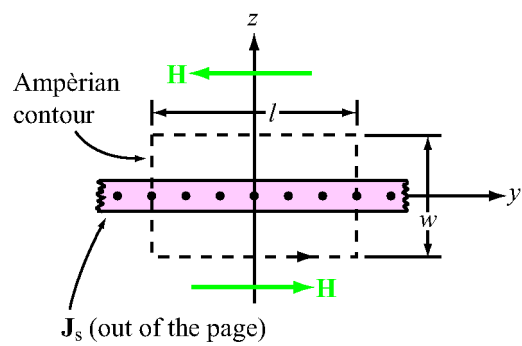


**Figure 5-19:** A thin current sheet in the  $x$ - $y$  plane carrying a surface current density  $\mathbf{J}_s = \hat{\mathbf{x}}J_s$  (Example 5-6).

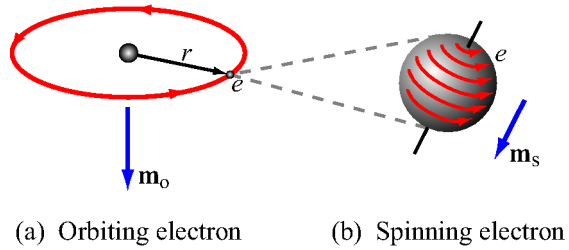
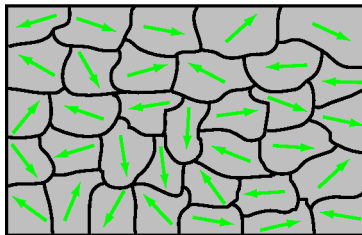
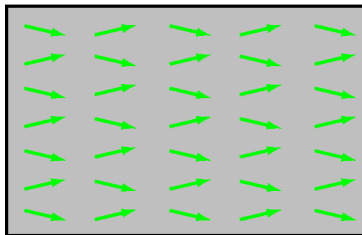


**Figure 5-20:** An electron generates (a) an orbital magnetic moment  $\mathbf{m}_o$  as it rotates around the nucleus and (b) a spin magnetic moment  $\mathbf{m}_s$ , as it spins about its own axis.



(a) Unmagnetized domains



(b) Magnetized domains

**Figure 5-21:** Comparison of (a) unmagnetized and (b) magnetized domains in a ferromagnetic material.

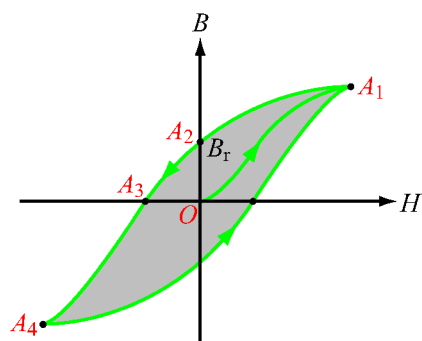


**Figure 5-22:** Typical hysteresis curve for a ferromagnetic material.

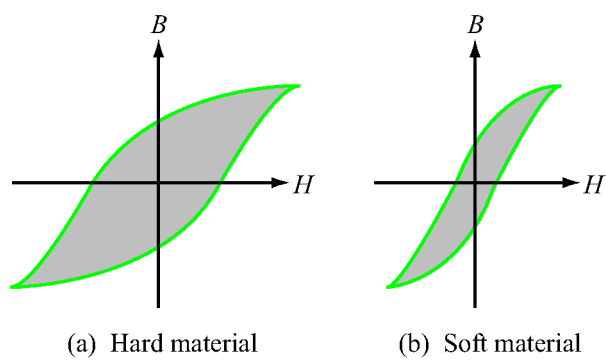


**Figure 5-23:** Comparison of hysteresis curves for (a) a hard ferromagnetic material and (b) a soft ferromagnetic material.

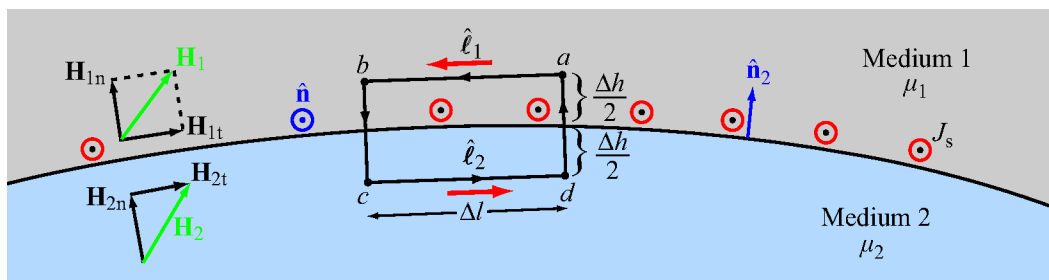


**Figure 5-24:** Boundary between medium 1 with  $\mu_1$  and medium 2 with  $\mu_2$ .

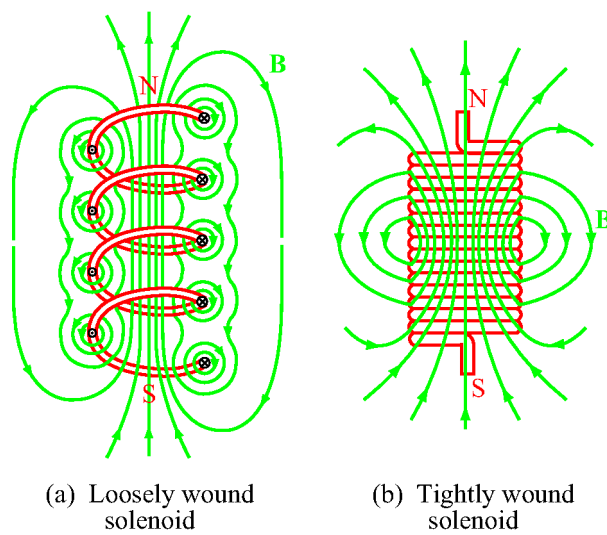


**Figure 5-25:** Magnetic field lines of (a) a loosely wound solenoid and (b) a tightly wound solenoid.



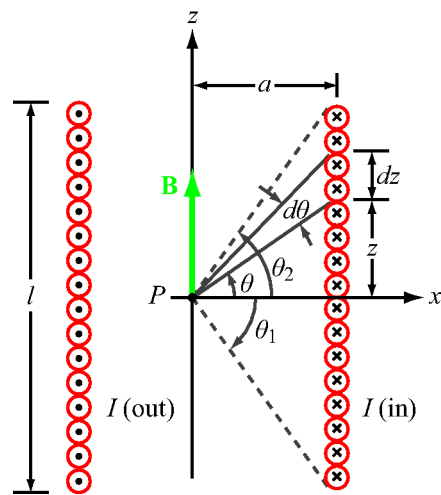
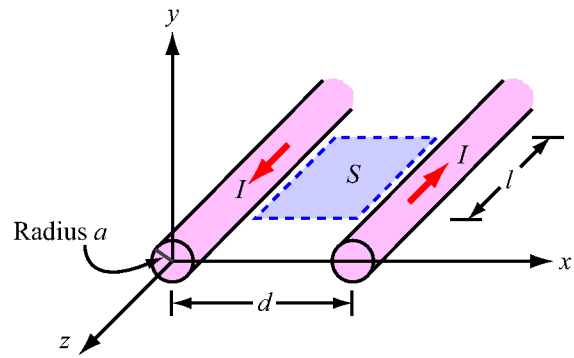
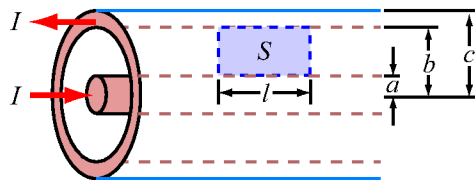


**Figure 5-26:** Solenoid cross section showing geometry for calculating  $\mathbf{H}$  at a point  $P$  on the solenoid axis.



(a) Parallel-wire transmission line



(b) Coaxial transmission line

**Figure 5-27:** To compute the inductance per unit length of a two-conductor transmission line, we need to determine the magnetic flux through the area  $S$  between the conductors.

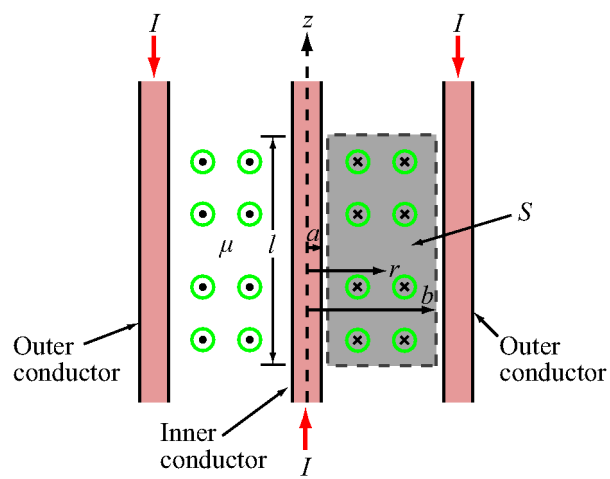


**Figure 5-28:** Cross-sectional view of coaxial transmission line (Example 5-7).

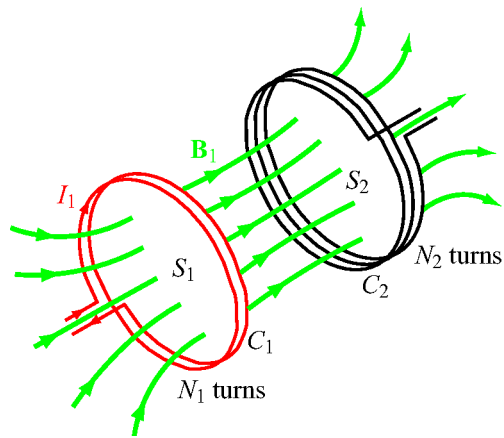


**Figure 5-29:** Magnetic field lines generated by current  $I_1$  in loop 1 linking surface  $S_2$  of loop 2.

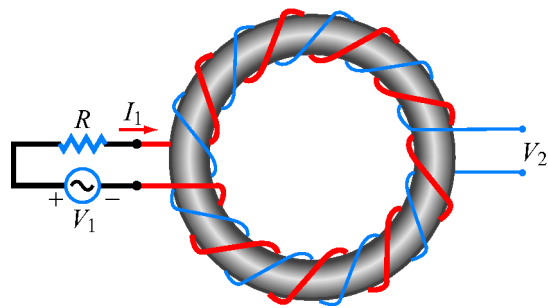


**Figure 5-30:** Toroidal coil with two windings used as a transformer.

## Chapter 6 Figures

**Figure 6-1** The galvanometer (predecessor of the ammeter) shows a deflection whenever the magnetic flux passing through the square loop changes with time.

**Figure 6-2** (a) Stationary circular loop in a changing magnetic field  $\mathbf{B}(t)$ , and (b) its equivalent circuit.

**Figure 6-3** Circular loop with  $N$  turns in the  $x$ - $y$  plane. The magnetic field is  $\mathbf{B} = B_0(\hat{y}2 + \hat{z}3) \sin \omega t$  (Example 6-1).

**Figure 6-4** Circuit for Example 6-2.

**Figure 6-5** In a transformer, the directions of  $I_1$  and  $I_2$  are such that the flux  $\Phi$  generated by one of them is opposite to that generated by the other. The direction of the secondary winding in (b) is opposite to that in (a), and so are the direction of  $I_2$  and the polarity of  $V_2$ .

**Figure 6-6** Equivalent circuit for the primary side of the transformer.

**Figure 6-7** Conducting wire moving with velocity  $\mathbf{u}$  in a static magnetic field.

**Figure 6-8** Sliding bar with velocity  $\mathbf{u}$  in a magnetic field that increases linearly with  $x$ ; that is,  $\mathbf{B} = \hat{z}B_0x$  (Example 6-3).

**Figure 6-9** Moving loop of Example 6-4.

**Figure 6-10** Moving rod of Example 6-5.

**Figure 6-11** Principles of the ac motor and the ac generator. In (a) the magnetic torque on the wires causes the loop to rotate, and in (b) the rotating loop generates an emf.

**Figure 6-12** A loop rotating in a magnetic field induces an emf.

**Figure 6-13** The displacement current  $I_{2d}$  in the insulating material of the capacitor is equal to the conducting current  $I_{1c}$  in the wire.

**Figure 6-14** The total current flowing out of a volume  $v$  is equal to the flux of the current density  $\mathbf{J}$  through the surface  $S$ , which in turn is equal to the rate of decrease of the charge enclosed in  $v$ .

**Figure 6-15** Kirchhoff's current law states that the algebraic sum of all the currents flowing out of a junction is zero.

**Figure 6-16** Electric potential  $V(\mathbf{R})$  due to a charge distribution  $\rho_v$  over a volume  $v'$ .

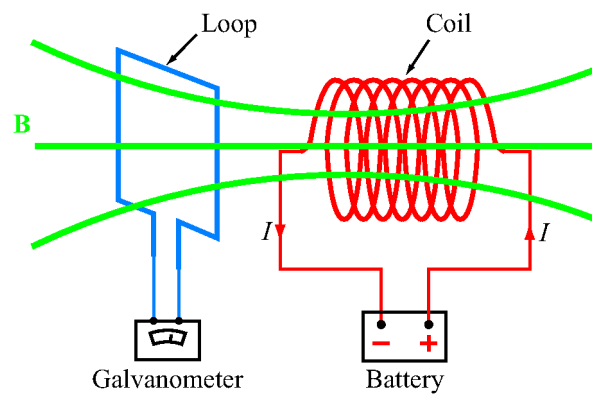
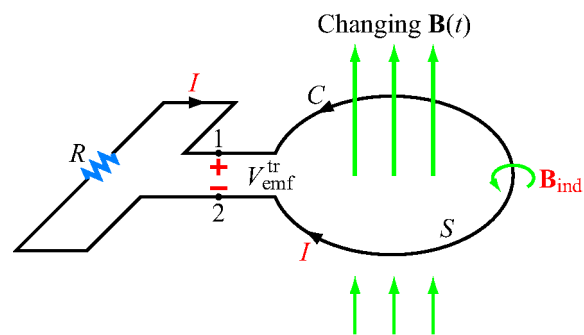
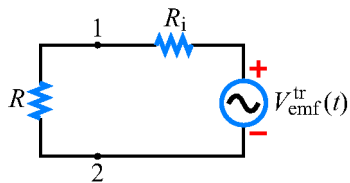


**Figure 6-1:** The galvanometer (predecessor of the ammeter) shows a deflection whenever the magnetic flux passing through the square loop changes with time.





(a) Loop in a changing  $\mathbf{B}$  field



(b) Equivalent circuit

**Figure 6-2:** (a) Stationary circular loop in a changing magnetic field  $\mathbf{B}(t)$ , and (b) its equivalent circuit.

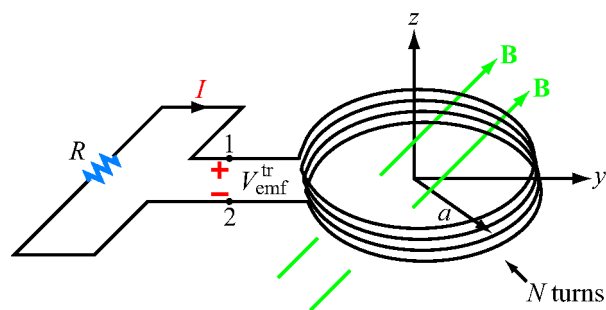


**Figure 6-3:** Circular loop with  $N$  turns in the  $x$ - $y$  plane. The magnetic field is  $\mathbf{B} = B_0(\hat{\mathbf{y}}2 + \hat{\mathbf{z}}3) \sin \omega t$  (Example 6-1).

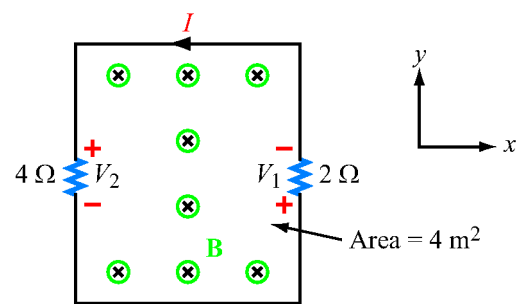


**Figure 6-4:** Circuit for Example 6-2.

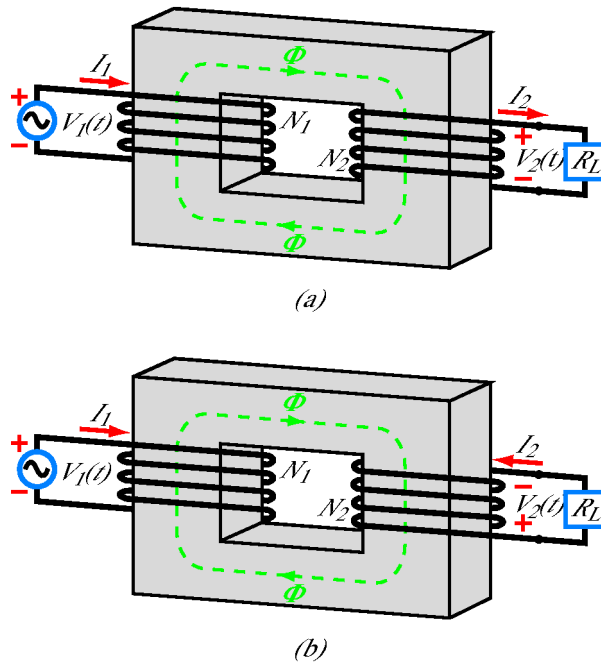


**Figure 6-5:** In a transformer, the directions of  $I_1$  and  $I_2$  are such that the flux  $\Phi$  generated by one of them is opposite to that generated by the other. The direction of the secondary winding in (b) is opposite to that in (a), and so are the direction of  $I_2$  and the polarity of  $V_2$ .

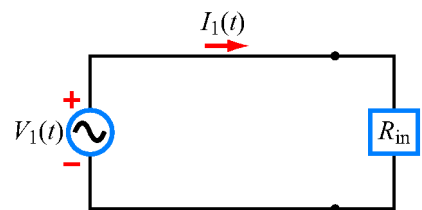


**Figure 6-6:** Equivalent circuit for the primary side of the transformer.

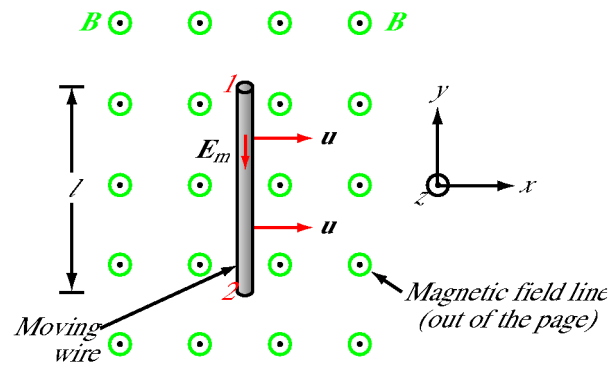


**Figure 6-7:** Conducting wire moving with velocity  $\mathbf{u}$  in a static magnetic field.

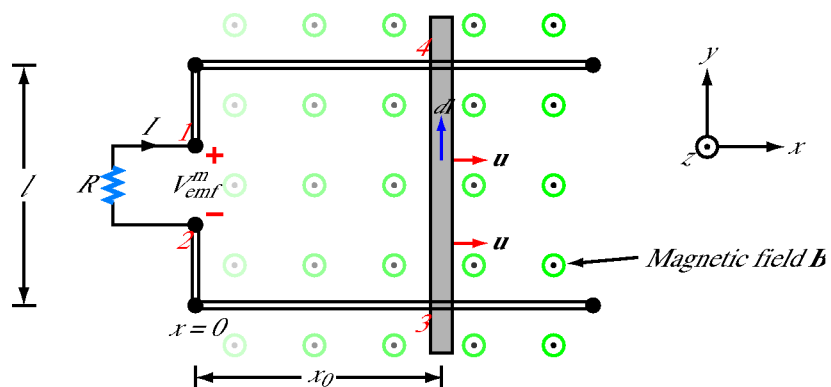


**Figure 6-8:** Sliding bar with velocity  $\mathbf{u}$  in a magnetic field that increases linearly with  $x$ ; that is,  $\mathbf{B} = \hat{\mathbf{z}}B_0x$  (Example 6-3).

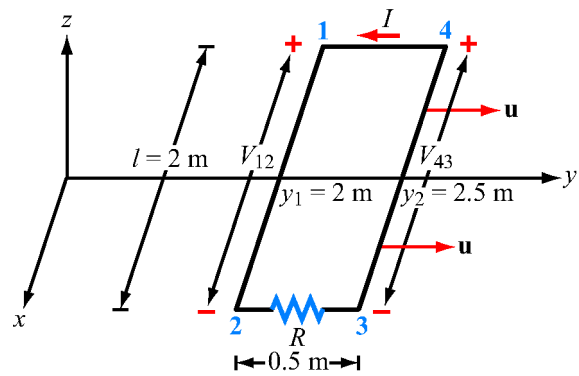


**Figure 6-9:** Moving loop of Example 6-4.



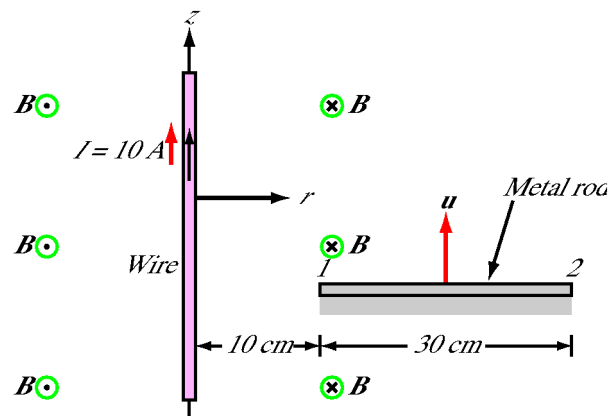


**Figure 6-10:** Moving rod of Example 6-5.

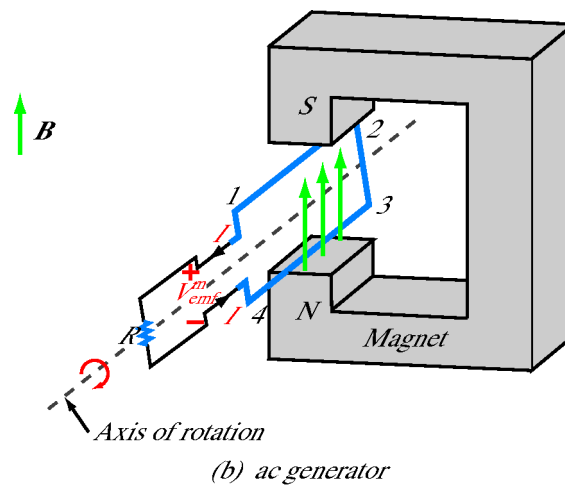
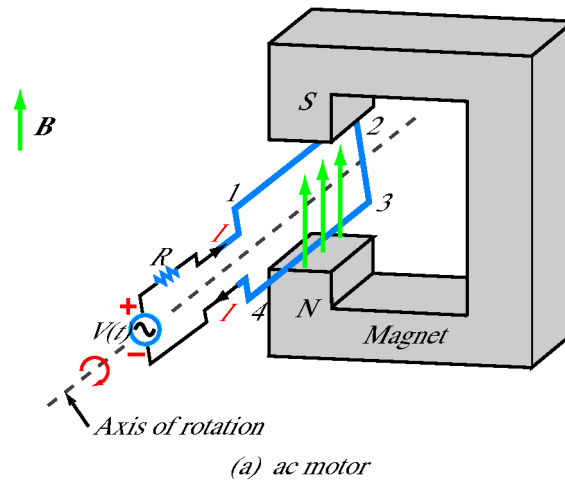


**Figure 6-11:** Principles of the ac motor and the ac generator. In (a) the magnetic torque on the wires causes the loop to rotate, and in (b) the rotating loop generates an emf.

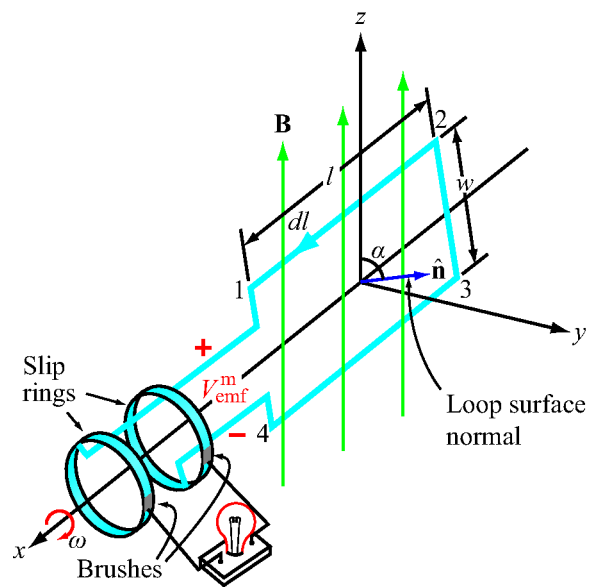


**Figure 6-12:** A loop rotating in a magnetic field induces an emf.

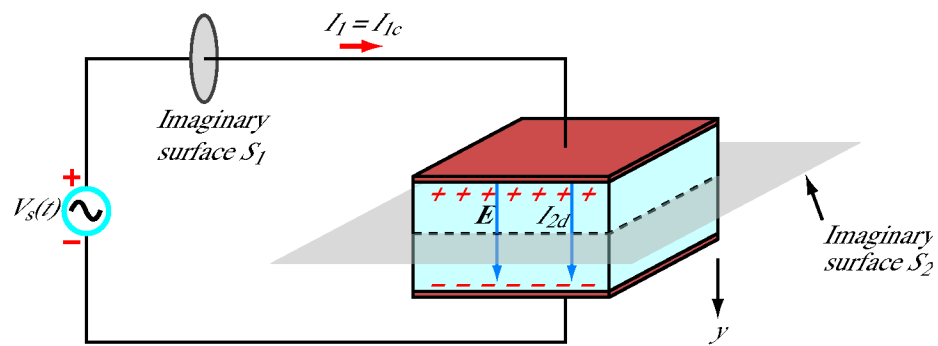


**Figure 6-13:** The displacement current  $I_{2d}$  in the insulating material of the capacitor is equal to the conducting current  $I_{1c}$  in the wire.

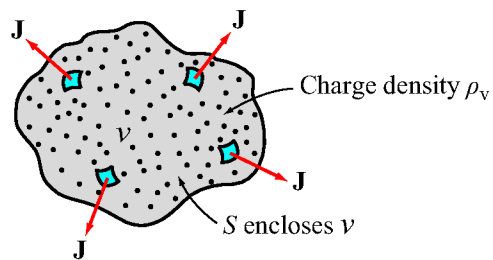


**Figure 6-14:** The total current flowing out of a volume  $V$  is equal to the flux of the current density  $\mathbf{J}$  through the surface  $S$ , which in turn is equal to the rate of decrease of the charge enclosed in  $V$ .

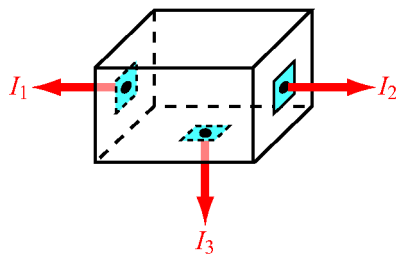


**Figure 6-15:** Kirchhoff's current law states that the algebraic sum of all the currents flowing out of a junction is zero.

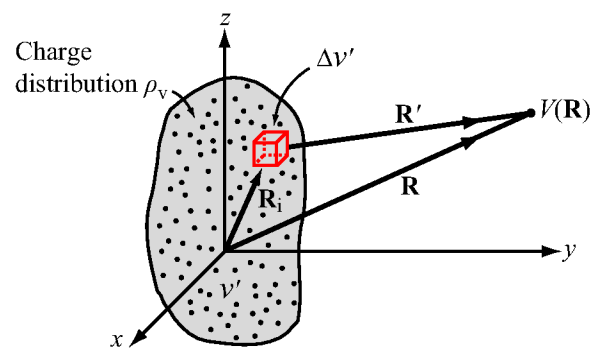


**Figure 6-16:** Electric potential  $V(\mathbf{R})$  due to a charge distribution  $\rho_v$  over a volume  $V'$ .

## Chapter 7 Figures

**Figure 7-1** Waves radiated by an EM source, such as a light bulb or an antenna, have spherical wavefronts, as in (a); to a distant observer, however, the wavefront across the observer's aperture appears approximately planar, as in (b).

**Figure 7-2** The atmospheric layer bounded by the ionosphere at the top and Earth's surface at the bottom forms a guiding structure for the propagation of radio waves in the HF band.

**Figure 7-3** A guided electromagnetic wave traveling in a coaxial transmission line consists of time-varying electric and magnetic fields in the dielectric medium between the inner and outer conductors.

**Figure 7-4** A transverse electromagnetic (TEM) wave propagating in the direction  $\hat{\mathbf{k}} = \hat{\mathbf{z}}$ . For all TEM waves,  $\hat{\mathbf{k}}$  is parallel to  $\mathbf{E} \times \mathbf{H}$ .

**Figure 7-5** Spatial variations of  $\mathbf{E}$  and  $\mathbf{H}$  at  $t = 0$  for the plane wave of Example 7-1.

**Figure 7-6** The wave  $(\mathbf{E}, \mathbf{H})$  is equivalent to the sum of two waves, one with fields  $(E_x^+, H_y^+)$  and another with  $(E_y^+, H_x^+)$ , with both traveling in the  $+z$ -direction.

**Figure 7-7** Linearly polarized wave traveling in the  $+z$ -direction (out of the page).

**Figure 7-8** Circularly polarized plane waves propagating in the  $+z$ -direction (out of the page).

**Figure 7-9** Right-hand circularly polarized wave radiated by a helical antenna.

**Figure 7-10** Right-hand circularly polarized wave of Example 7-2.

**Figure 7-11** Polarization ellipse in the  $x$ - $y$  plane, with the wave traveling in the  $z$ -direction (out of the page).

**Figure 7-12** Polarization states for various combinations of the polarization angles  $(\gamma, \chi)$  for a wave traveling out of the page.

**Figure 7-13** Attenuation of the magnitude of  $\tilde{E}_x(z)$  with distance  $z$ . The skin depth  $\delta_s$  is the value of  $z$  at which  $|\tilde{E}_x(z)|/|E_{x0}| = e^{-1}$ , or  $z = \delta_s = 1/\alpha$ .

**Figure 7-14** Current density  $\mathbf{J}$  in a conducting wire is (a) uniform across its cross section in the dc case, but (b) in the ac case,  $\mathbf{J}$  is highest along the wire's perimeter.

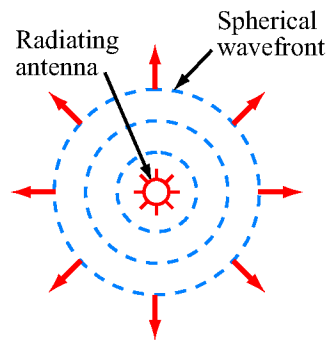


**Figure 7-15** Exponential decay of current density  $\tilde{J}_x(z)$  with  $z$  in a solid conductor. The total current flowing through (a) a section of width  $w$  extending between  $z = 0$  and  $z = \infty$  is equivalent to (b) a constant current density  $J_0$  flowing through a section of depth  $\delta_s$ .

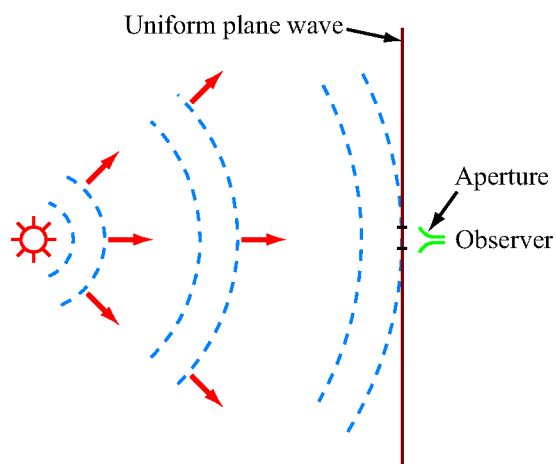
**Figure 7-16** The inner conductor of the coaxial cable in (a) is represented in (b) by a planar conductor of width  $2\pi a$  and depth  $\delta_s$ , as if its skin has been cut along its length on the bottom side and then unfurled into a planar geometry.

**Figure 7-17** EM power flow through an aperture.

**Figure 7-18** Solar radiation intercepted by (a) a spherical surface of radius  $R_s$ , and (b) Earth's surface (Example 7-5).



(a) Spherical wave



(b) Plane-wave approximation

**Figure 7-1:** Waves radiated by an EM source, such as a light bulb or an antenna, have spherical wavefronts, as in (a); to a distant observer, however, the wavefront across the observer's aperture appears approximately planar, as in (b).

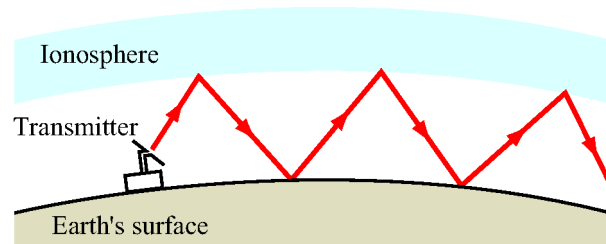


**Figure 7-2:** The atmospheric layer bounded by the ionosphere at the top and Earth's surface at the bottom forms a guiding structure for the propagation of radio waves in the HF band.

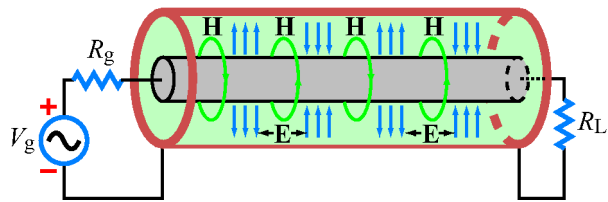


**Figure 7-3:** A guided electromagnetic wave traveling in a coaxial transmission line consists of time-varying electric and magnetic fields in the dielectric medium between the inner and outer conductors.

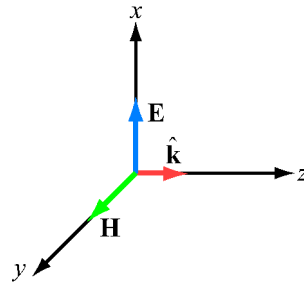


**Figure 7-4:** A transverse electromagnetic (TEM) wave propagating in the direction  $\hat{\mathbf{k}} = \hat{\mathbf{z}}$ . For all TEM waves,  $\hat{\mathbf{k}}$  is parallel to  $\mathbf{E} \times \mathbf{H}$ .

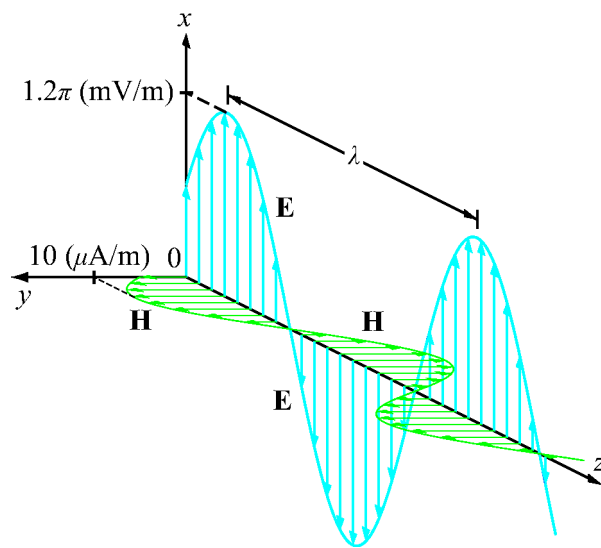


**Figure 7-5:** Spatial variations of  $\mathbf{E}$  and  $\mathbf{H}$  at  $t = 0$  for the plane wave of Example 7-1.

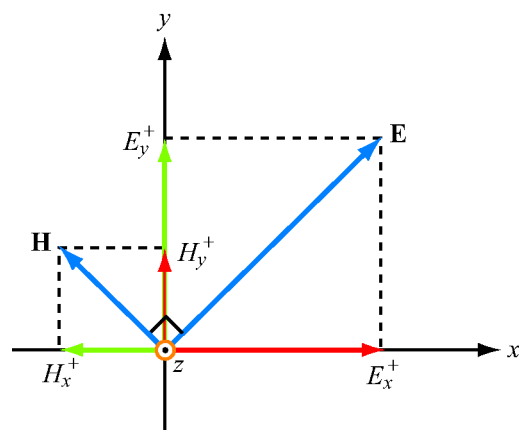


**Figure 7-6:** The wave  $(\mathbf{E}, \mathbf{H})$  is equivalent to the sum of two waves, one with fields  $(E_x^+, H_y^+)$  and another with  $(E_y^+, H_x^+)$ , with both traveling in the  $+z$ -direction.

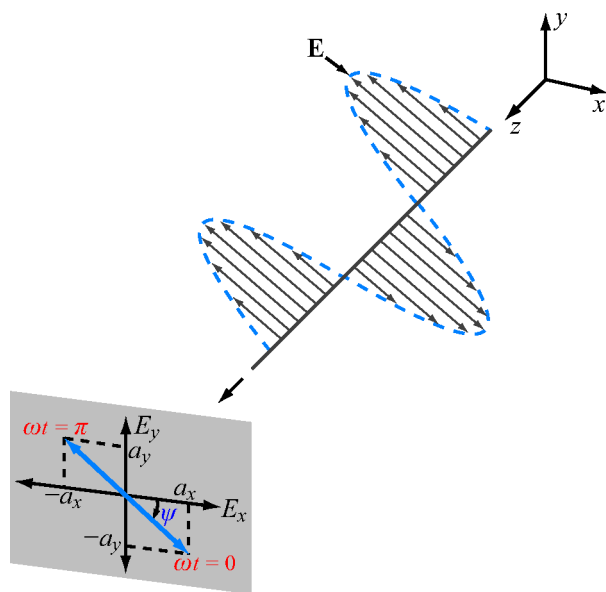
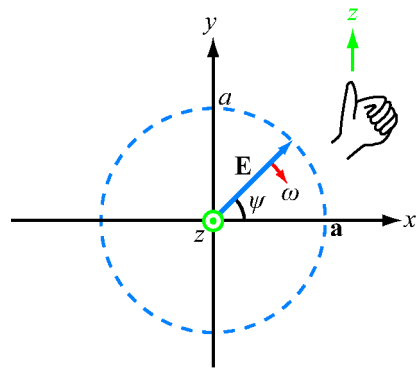
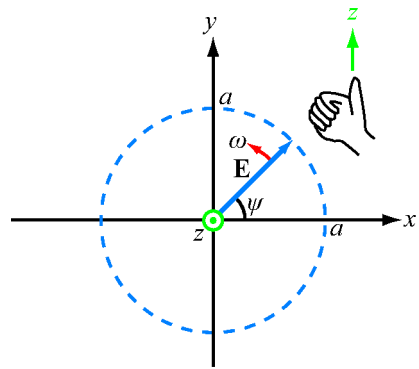


**Figure 7-7:** Linearly polarized wave traveling in the  $+z$ -direction (out of the page).





(a) LHC polarization



(b) RHC polarization

**Figure 7-8:** Circularly polarized plane waves propagating in the  $+z$ -direction (out of the page).

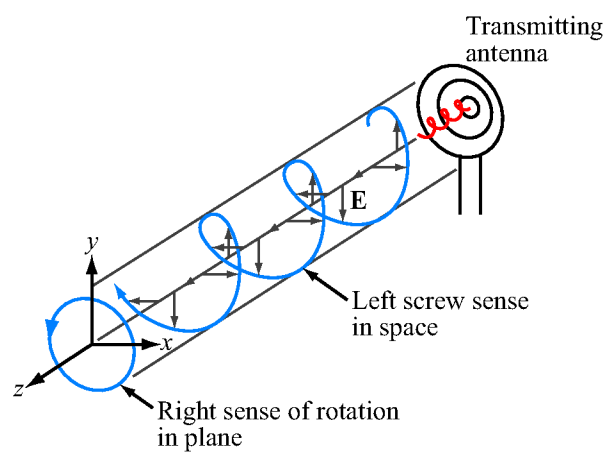


**Figure 7-9:** Right-hand circularly polarized wave radiated by a helical antenna.

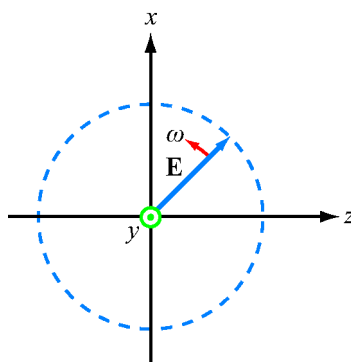


**Figure 7-10:** Right-hand circularly polarized wave of Example 7-2.

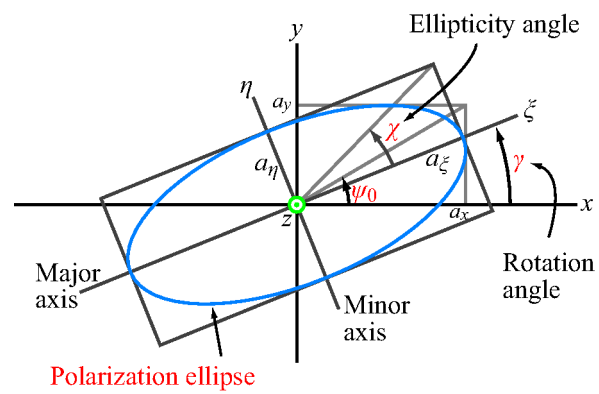


**Figure 7-11:** Polarization ellipse in the  $x$ - $y$  plane, with the wave traveling in the  $z$ -direction (out of the page).

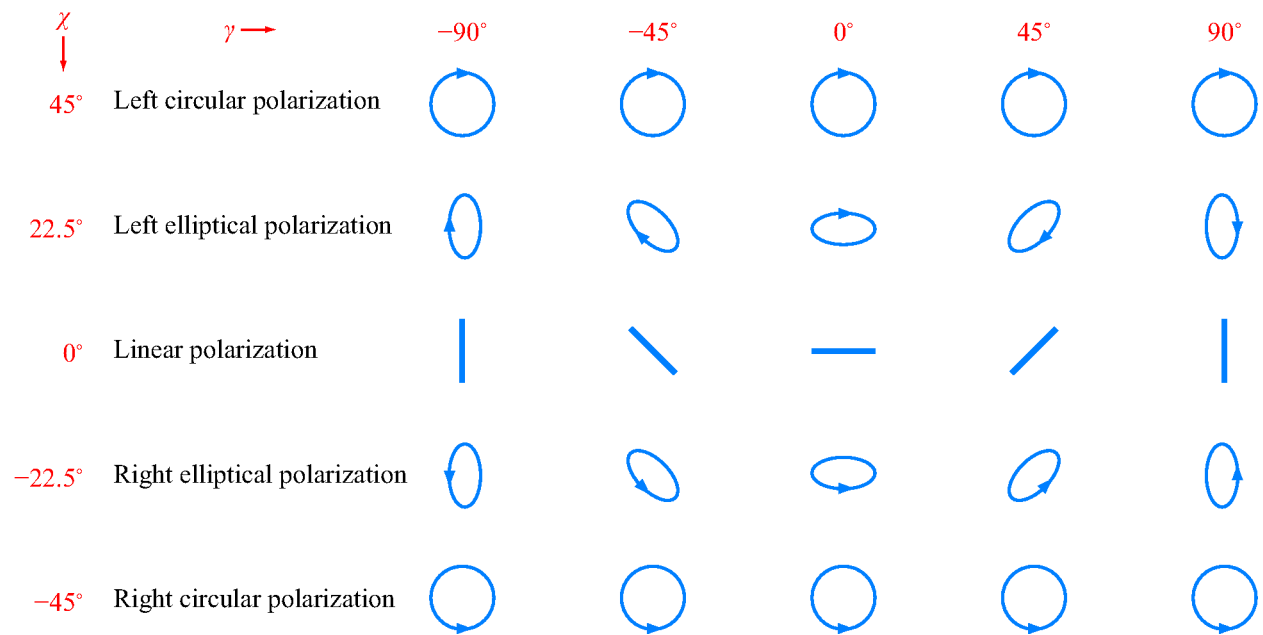


**Figure 7-12:** Polarization states for various combinations of the polarization angles  $(\gamma, \chi)$  for a wave traveling out of the page.

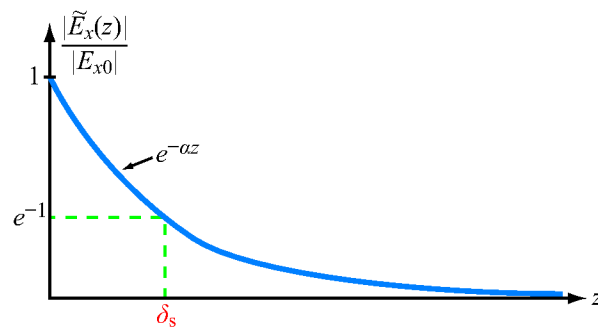


**Figure 7-13:** Attenuation of the magnitude of  $\tilde{E}_x(z)$  with distance  $z$ . The skin depth  $\delta_s$  is the value of  $z$  at which  $|\tilde{E}_x(z)|/|E_{x0}| = e^{-1}$ , or  $z = \delta_s = 1/\alpha$ .

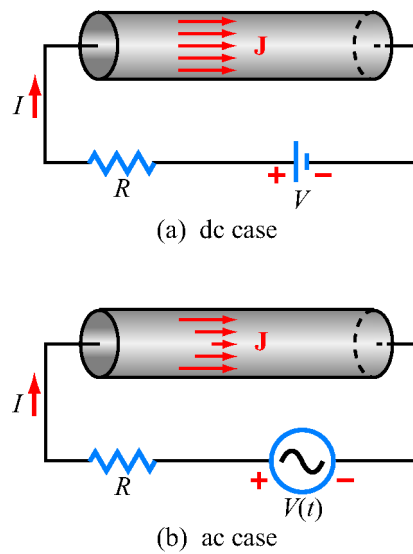
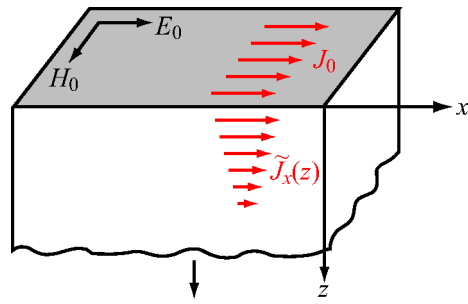
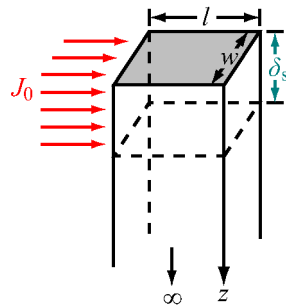


**Figure 7-14:** Current density  $\mathbf{J}$  in a conducting wire is (a) uniform across its cross section in the dc case, but (b) in the ac case,  $\mathbf{J}$  is highest along the wire's perimeter.



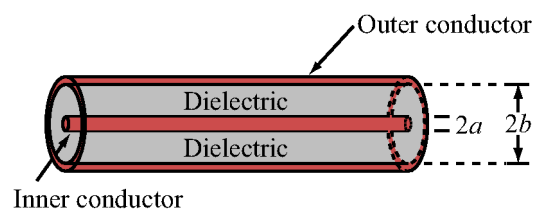
(a) Exponentially decaying  $\tilde{J}_x(z)$



(b) Equivalent  $J_0$  over skin depth  $\delta_s$

**Figure 7-15:** Exponential decay of current density  $\tilde{J}_x(z)$  with  $z$  in a solid conductor. The total current flowing through (a) a section of width  $w$  extending between  $z = 0$  and  $z = \infty$  is equivalent to (b) a constant current density  $J_0$  flowing through a section of depth  $\delta_s$ .





(a) Coaxial cable



(b) Equivalent inner conductor

**Figure 7-16:** The inner conductor of the coaxial cable in (a) is represented in (b) by a planar conductor of width  $2\pi a$  and depth  $\delta_s$ , as if its skin has been cut along its length on the bottom side and then unfurled into a planar geometry.

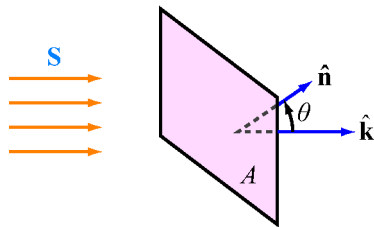
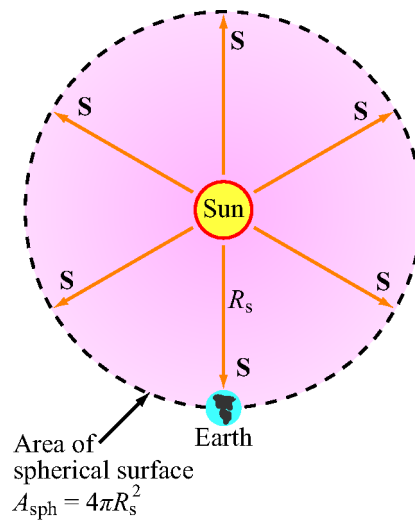
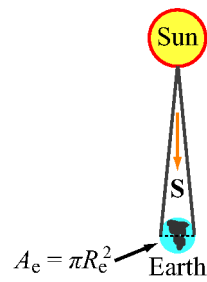


**Figure 7-17:** EM power flow through an aperture.



(a) Radiated solar power



(b) Earth intercepted power

**Figure 7-18:** Solar radiation intercepted by (a) a spherical surface of radius  $R_s$ , and (b) Earth's surface (Example 7-5).

## Chapter 8 Figures

**Figure 8-1** Signal path between a shipboard transmitter (Tx) and a submarine receiver (Rx).

**Figure 8-2** Discontinuity between two different transmission lines is analogous to that between two dissimilar media.

**Figure 8-3** Ray representation of wave reflection and transmission at (a) normal incidence and (b) oblique incidence, and (c) wavefront representation of oblique incidence.

**Figure 8-4** The two dielectric media separated by the  $x$ - $y$  plane in (a) can be represented by the transmission-line analogue in (b).

**Figure 8-5** Antenna beam “looking” through an aircraft radome of thickness  $d$  (Example 8-1).

**Figure 8-6** (a) Planar section of the radome of Fig. 8-5 at an expanded scale and (b) its transmission-line equivalent model (Example 8-1).

**Figure 8-7** Normal incidence at a planar boundary between two lossy media.

**Figure 8-8** Wave patterns for fields  $E_1(z, t)$  and  $H_1(z, t)$  of Example 8-3.

**Figure 8-9** Wave reflection and refraction at a planar boundary between different media.

**Figure 8-10** Snell’s laws state that  $\theta_r = \theta_i$  and  $\sin \theta_t = (n_1/n_2) \sin \theta_i$ . Refraction is (a) inward if  $n_1 < n_2$  and (b) outward if  $n_1 > n_2$ ; and (c) the refraction angle is  $90^\circ$  if  $n_1 > n_2$  and  $\theta_i$  is equal to or greater than the critical angle  $\theta_c = \sin^{-1}(n_2/n_1)$ .

**Figure 8-11** The exit angle  $\theta_3$  is equal to the incidence angle  $\theta_1$  if the dielectric slab has parallel boundaries and is surrounded by media with the same index of refraction on both sides (Example 8-4).

**Figure 8-12** Waves can be guided along optical fibers as long as the reflection angles exceed the critical angle for total internal reflection.

**Figure 8-13** Distortion of rectangular pulses caused by modal dispersion in optical fibers.

**Figure 8-14** The plane of incidence is the plane containing the direction of wave travel,  $\hat{\mathbf{k}}_i$ , and the surface normal to the boundary. In the present case the plane of incidence containing  $\hat{\mathbf{k}}_i$  and  $\hat{\mathbf{z}}$  coincides with the plane of the paper. A wave is (a) perpendicularly polarized

when its electric field vector is perpendicular to the plane of incidence and (b) parallel polarized when its electric field vector lies in the plane of incidence.

**Figure 8-15** Perpendicularly polarized plane wave incident at an angle  $\theta_i$  upon a planar boundary.

**Figure 8-16** Parallel polarized plane wave incident at an angle  $\theta_i$  upon a planar boundary.

**Figure 8-17** Plots for  $|\Gamma_{\perp}|$  and  $|\Gamma_{\parallel}|$  as a function of  $\theta_i$  for a dry soil surface, a wet-soil surface, and a water surface. For each surface,  $|\Gamma_{\parallel}| = 0$  at the Brewster angle.

**Figure 8-18** Reflection and transmission of an incident circular beam illuminating a spot of size  $A$  on the interface.

**Figure 8-19** Angular plots for  $(R_{\parallel}, T_{\parallel})$  for an air–glass interface.

**Figure 8-20** Wave travel by successive reflections in (a) an optical fiber, (b) a circular metal waveguide, and (c) a rectangular metal waveguide.

**Figure 8-21** The inner conductor of a coaxial cable can excite an EM wave in the waveguide.

**Figure 8-22** Waveguide coordinate system.

**Figure 8-23**  $TM_{11}$  electric and magnetic field lines across two cross-sectional planes.

**Figure 8-24** Cutoff frequencies for TE and TM modes in a hollow rectangular waveguide with  $a = 3$  cm and  $b = 2$  cm (Example 8-9).

**Figure 8-25** The amplitude-modulated high-frequency waveform in (b) is the product of the Gaussian-shaped pulse with the sinusoidal high-frequency carrier in (a).

**Figure 8-26**  $\omega$ - $\beta$  diagram for TE and TM modes in a hollow rectangular waveguide. The straight line pertains to propagation in an unbounded medium or on a TEM transmission line.

**Figure 8-27** The  $TE_{10}$  mode can be constructed as the sum of two TEM waves.

**Figure 8-28** A resonant cavity supports a very narrow bandwidth around its resonant frequency  $f_0$ .

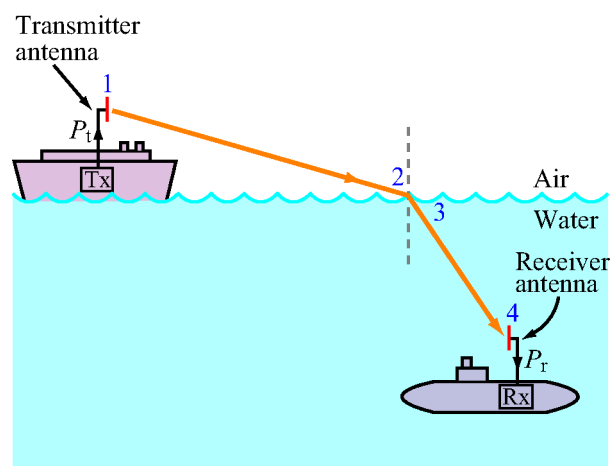
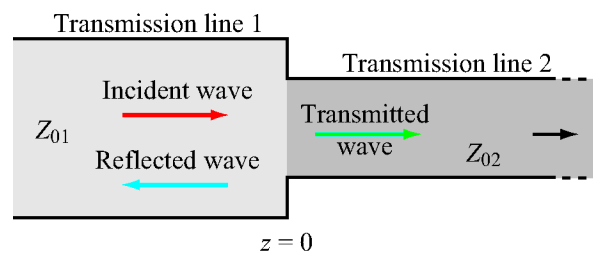
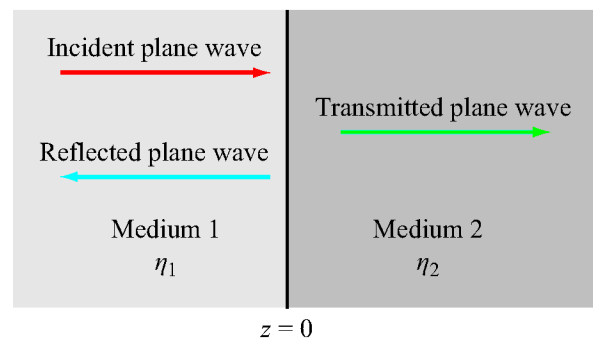


**Figure 8-1:** Signal path between a shipboard transmitter (Tx) and a submarine receiver (Rx).



(a) Boundary between transmission lines



(b) Boundary between different media

**Figure 8-2:** Discontinuity between two different transmission lines is analogous to that between two dissimilar media.

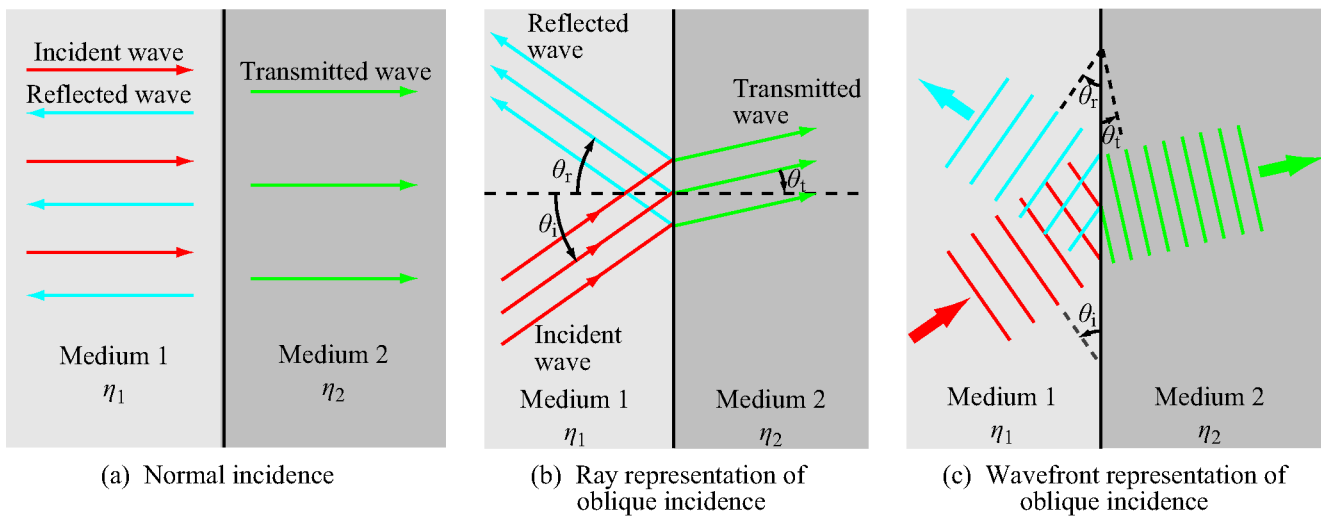
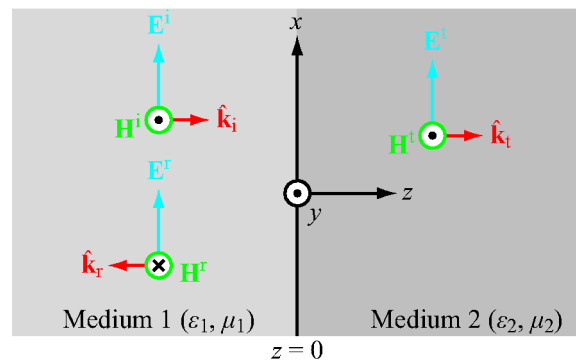
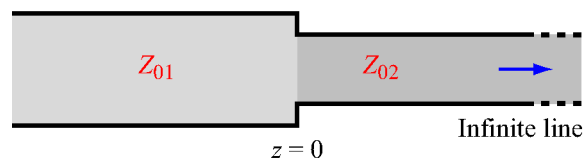


**Figure 8-3:** Ray representation of wave reflection and transmission at (a) normal incidence and (b) oblique incidence, and (c) wavefront representation of oblique incidence.





(a) Boundary between dielectric media



(b) Transmission-line analogue

**Figure 8-4:** The two dielectric media separated by the  $x$ - $y$  plane in (a) can be represented by the transmission-line analogue in (b).

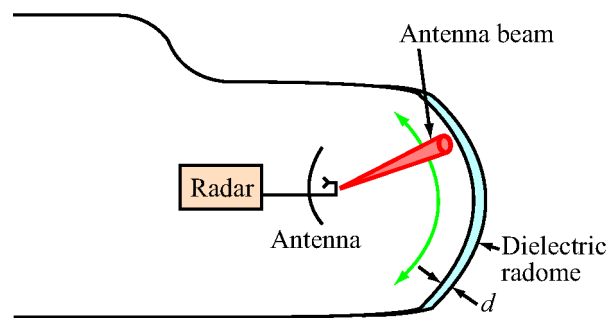


**Figure 8-5:** Antenna beam “looking” through an aircraft radome of thickness  $d$  (Example 8-1).

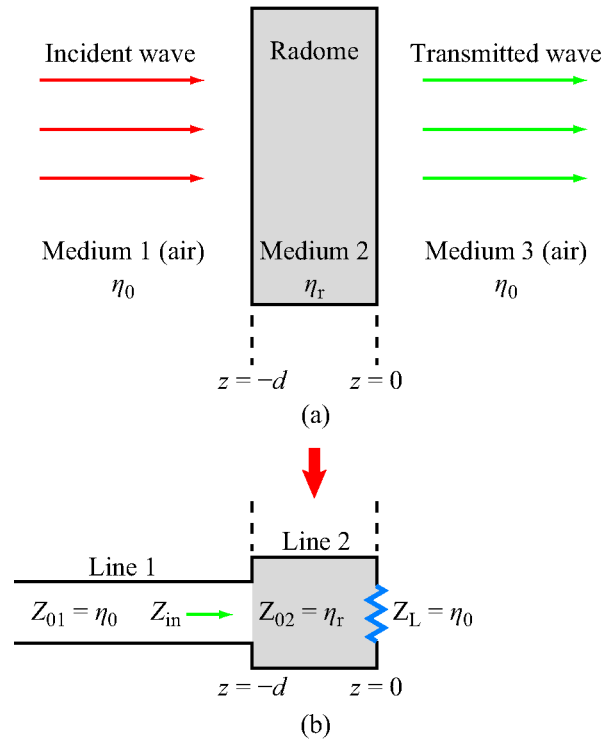
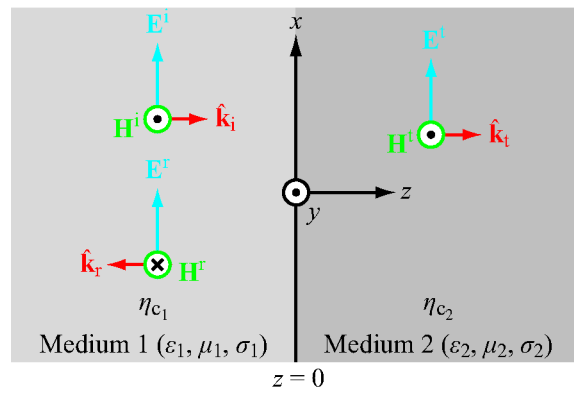
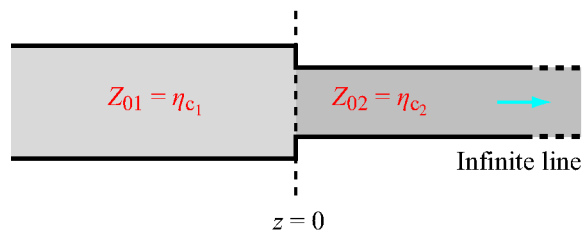


**Figure 8-6:** (a) Planar section of the radome of Fig. 8-5 at an expanded scale and (b) its transmission-line equivalent model (Example 8-1).



(a) Boundary between dielectric media



(b) Transmission-line analogue

**Figure 8-7:** Normal incidence at a planar boundary between two lossy media.

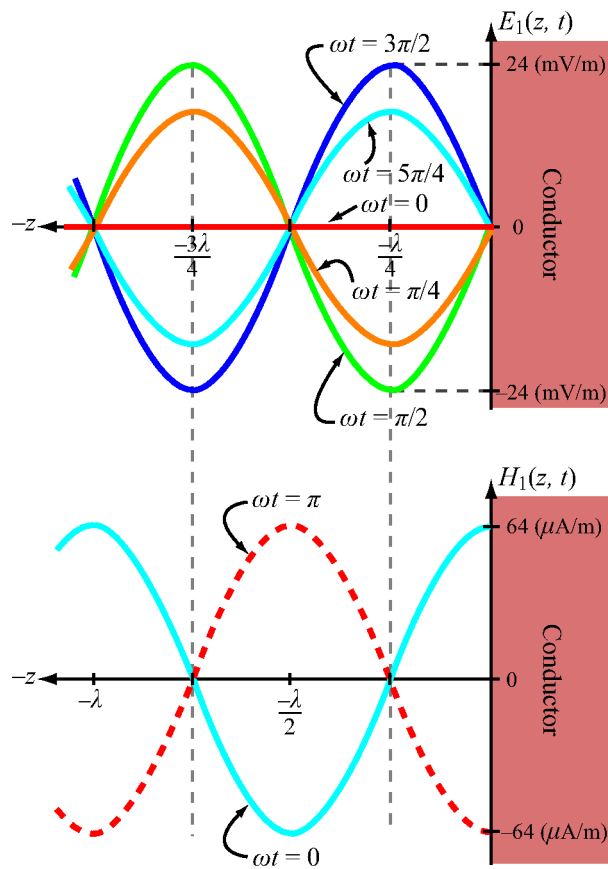


**Figure 8-8:** Wave patterns for fields  $E_1(z, t)$  and  $H_1(z, t)$  of Example 8-3.

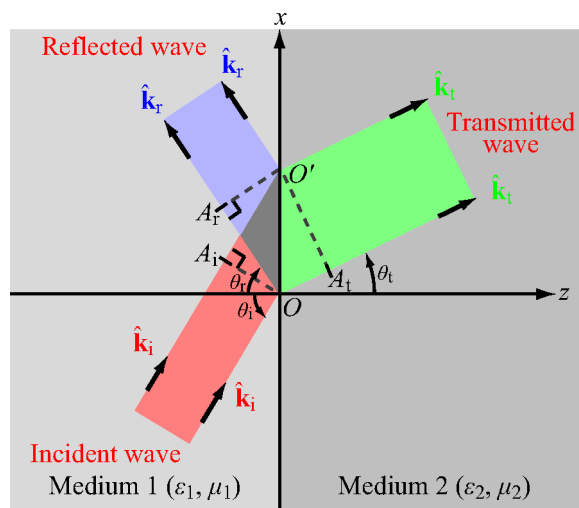


**Figure 8-9:** Wave reflection and refraction at a planar boundary between different media.

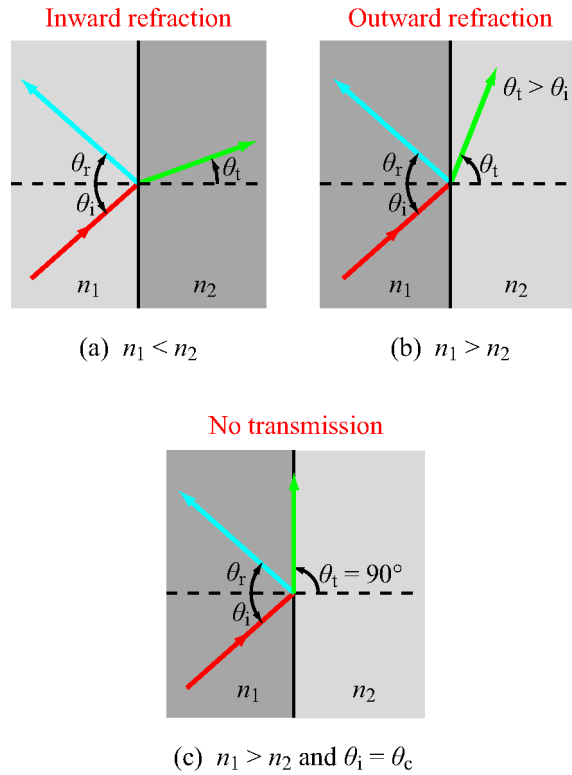


**Figure 8-10:** Snell's laws state that  $\theta_r = \theta_i$  and  $\sin \theta_t = (n_1/n_2) \sin \theta_i$ . Refraction is (a) inward if  $n_1 < n_2$  and (b) outward if  $n_1 > n_2$ ; and (c) the refraction angle is  $90^\circ$  if  $n_1 > n_2$  and  $\theta_i$  is equal to or greater than the critical angle  $\theta_c = \sin^{-1}(n_2/n_1)$ .

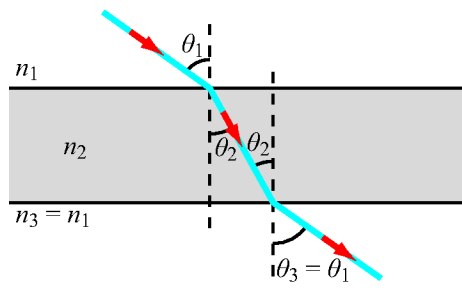


**Figure 8-11:** The exit angle  $\theta_3$  is equal to the incidence angle  $\theta_1$  if the dielectric slab has parallel boundaries and is surrounded by media with the same index of refraction on both sides (Example 8-4).



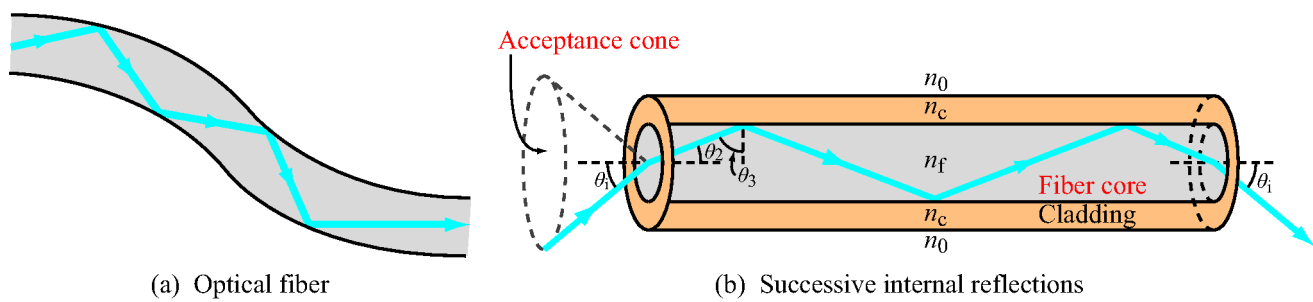


**Figure 8-12:** Waves can be guided along optical fibers as long as the reflection angles exceed the critical angle for total internal reflection.

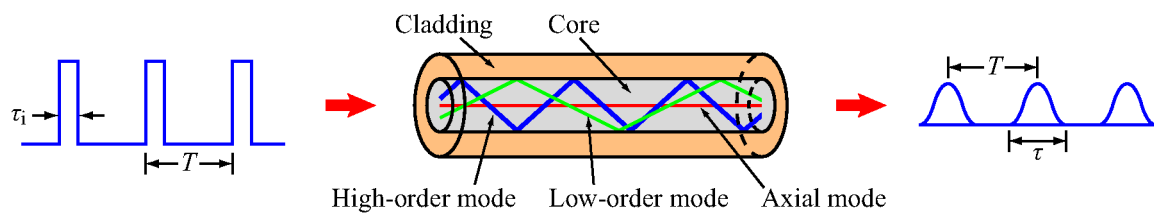
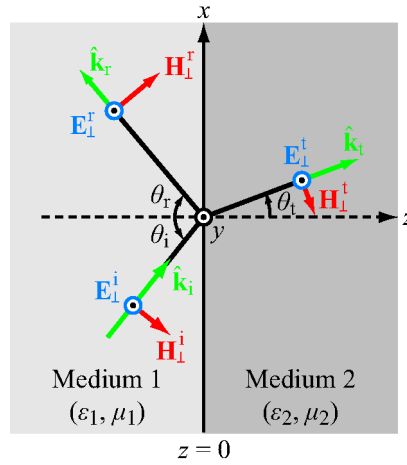
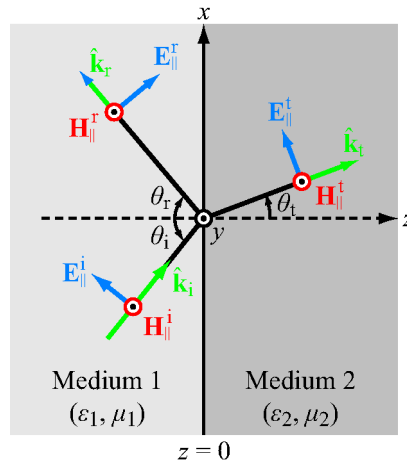


**Figure 8-13:** Distortion of rectangular pulses caused by modal dispersion in optical fibers.



(a) Perpendicular polarization



(b) Parallel polarization

**Figure 8-14:** The plane of incidence is the plane containing the direction of wave travel,  $\hat{k}_i$ , and the surface normal to the boundary. In the present case the plane of incidence containing  $\hat{k}_i$  and  $\hat{z}$  coincides with the plane of the paper. A wave is (a) perpendicularly polarized when its electric field vector is perpendicular to the plane of incidence and (b) parallel polarized when its electric field vector lies in the plane of incidence.

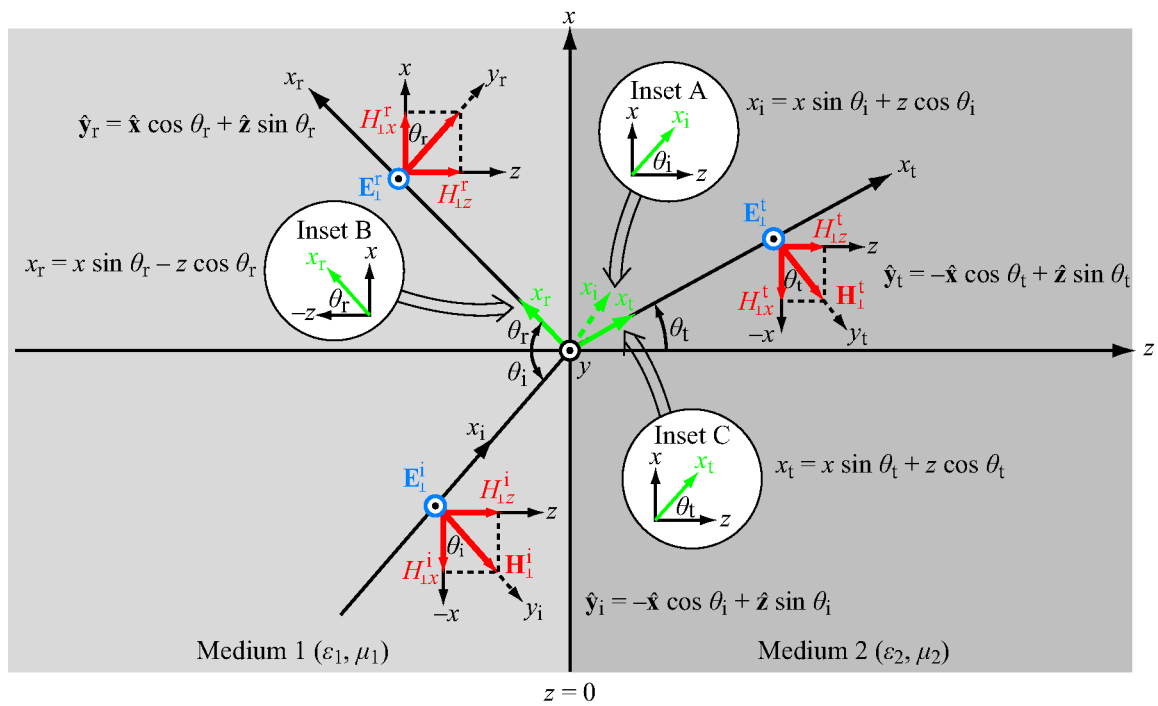


**Figure 8-15:** Perpendicularly polarized plane wave incident at an angle  $\theta_i$  upon a planar boundary.

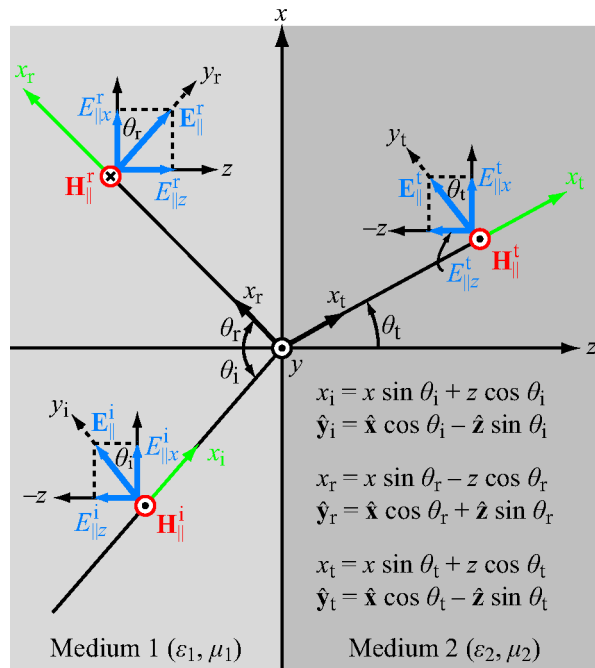


**Figure 8-16:** Parallel polarized plane wave incident at an angle  $\theta_i$  upon a planar boundary.

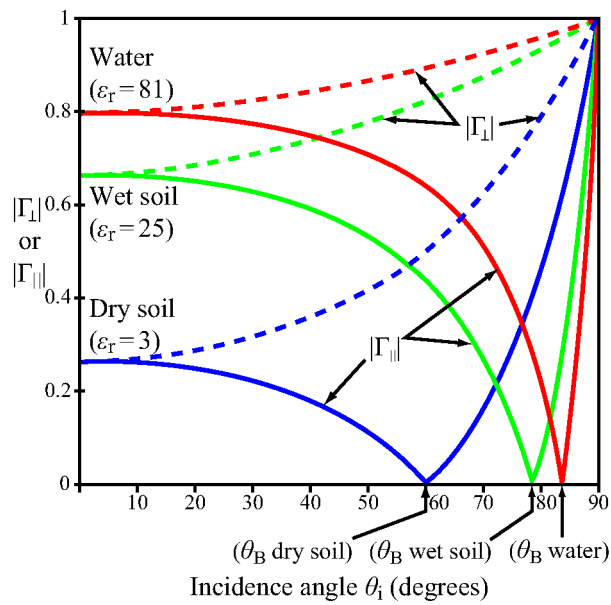


**Figure 8-17:** Plots for  $|\Gamma_{\perp}|$  and  $|\Gamma_{\parallel}|$  as a function of  $\theta_i$  for a dry soil surface, a wet-soil surface, and a water surface. For each surface,  $|\Gamma_{\parallel}| = 0$  at the Brewster angle.

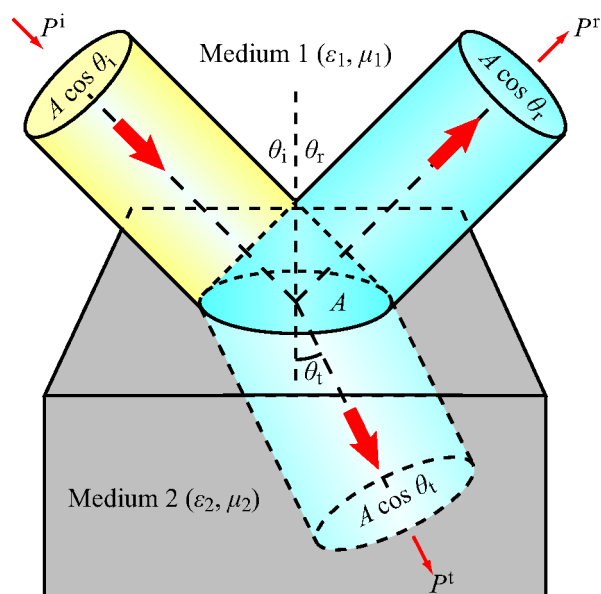


**Figure 8-18:** Reflection and transmission of an incident circular beam illuminating a spot of size  $A$  on the interface.

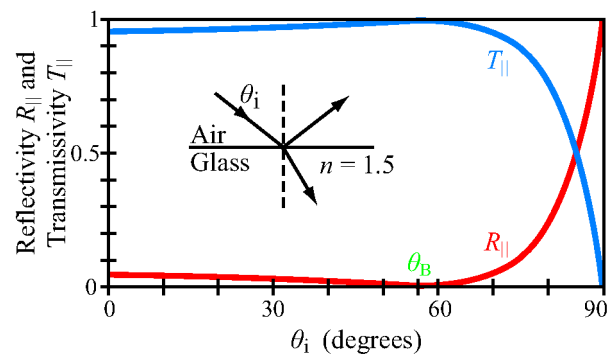
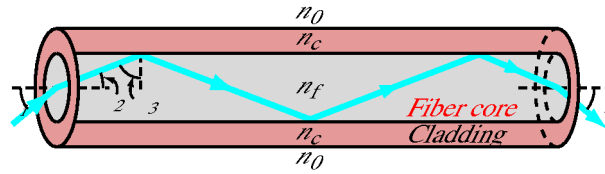
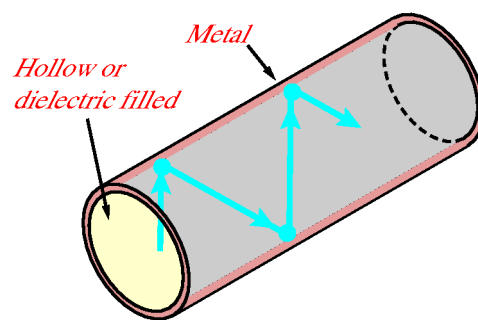


**Figure 8-19:** Angular plots for  $(R_{||}, T_{||})$  for an air-glass interface.

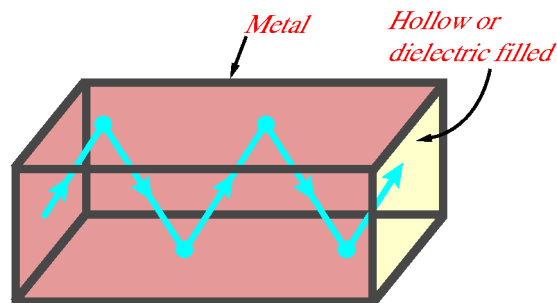




(a) Optical fiber

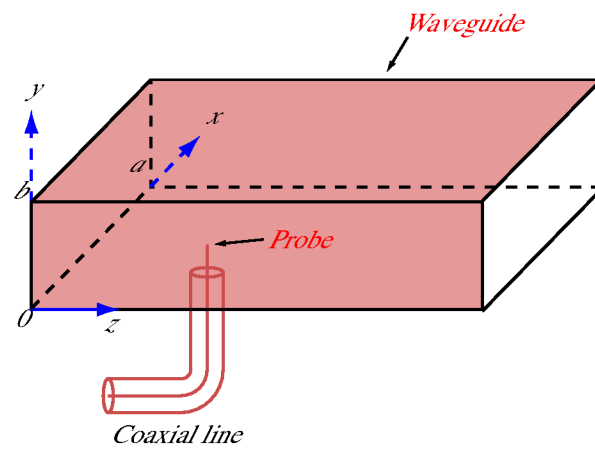


(b) Circular waveguide

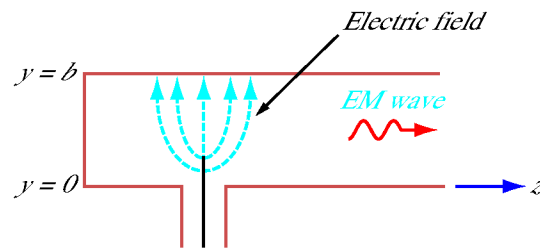


(c) Rectangular waveguide

**Figure 8-20:** Wave travel by successive reflections in (a) an optical fiber, (b) a circular metal waveguide, and (c) a rectangular metal waveguide.



(a) Coax-to-waveguide coupler



(b) Cross-sectional view at  $x = a/2$

**Figure 8-21:** The inner conductor of a coaxial cable can excite an EM wave in the waveguide.

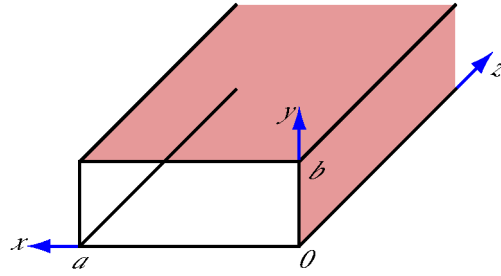


**Figure 8-22:** Waveguide coordinate system.

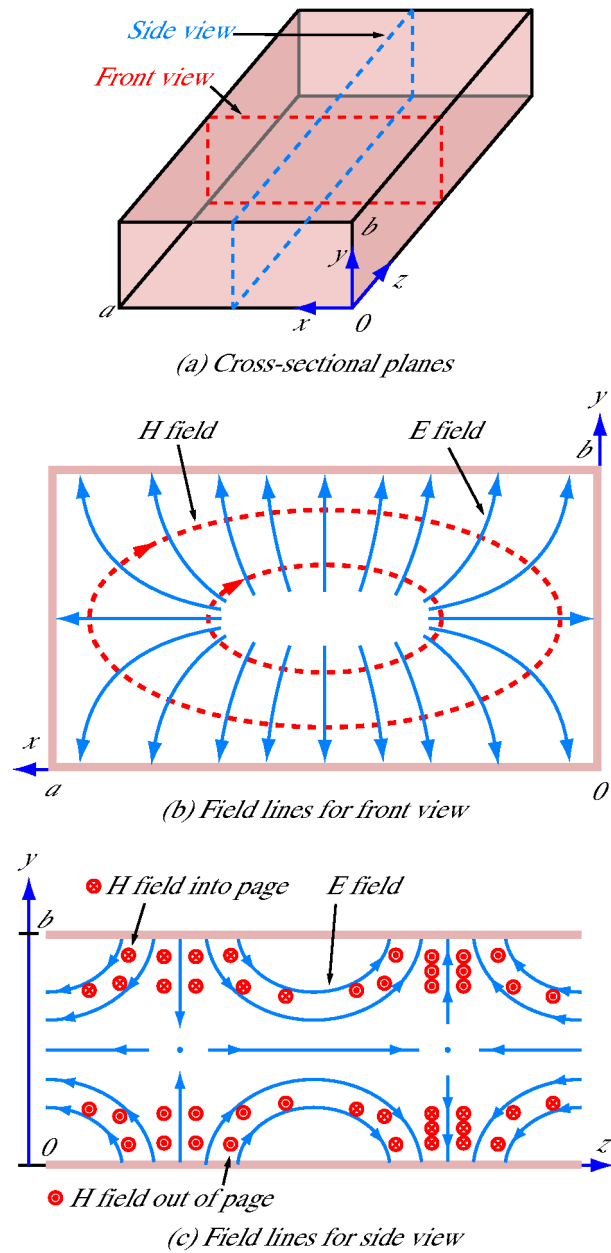


**Figure 8-23:**  $TM_{11}$  electric and magnetic field lines across two cross-sectional planes.

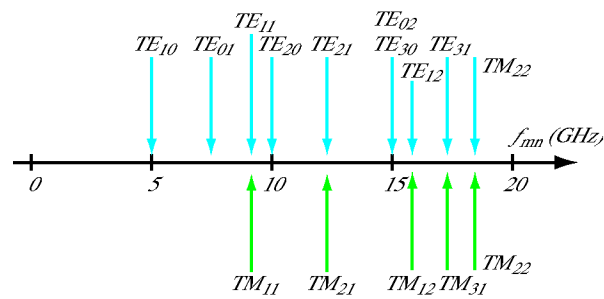


**Figure 8-24:** Cutoff frequencies for TE and TM modes in a hollow rectangular waveguide with  $a = 3$  cm and  $b = 2$  cm (Example 8-9).

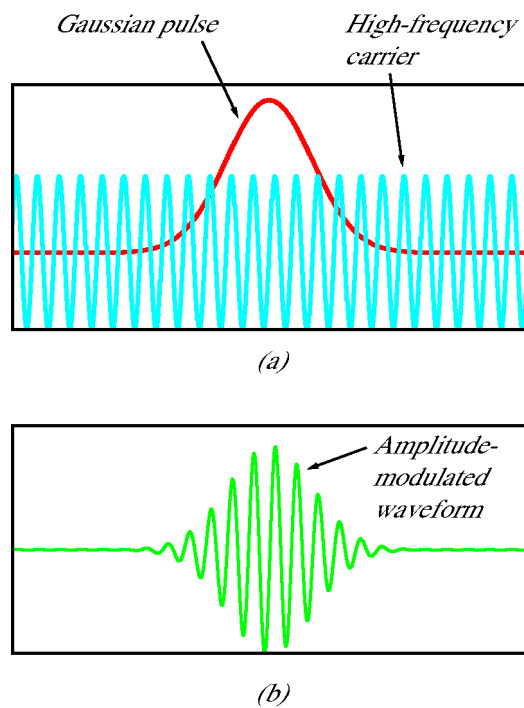


**Figure 8-25:** The amplitude-modulated high-frequency waveform in (b) is the product of the Gaussian-shaped pulse with the sinusoidal high-frequency carrier in (a).

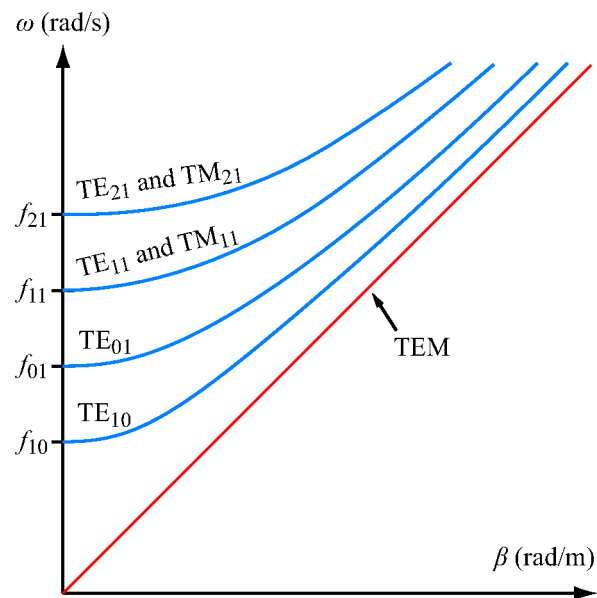
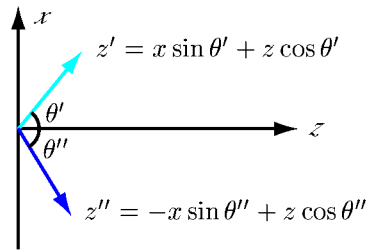


**Figure 8-26:**  $\omega$ - $\beta$  diagram for TE and TM modes in a hollow rectangular waveguide. The straight line pertains to propagation in an unbounded medium or on a TEM transmission line.



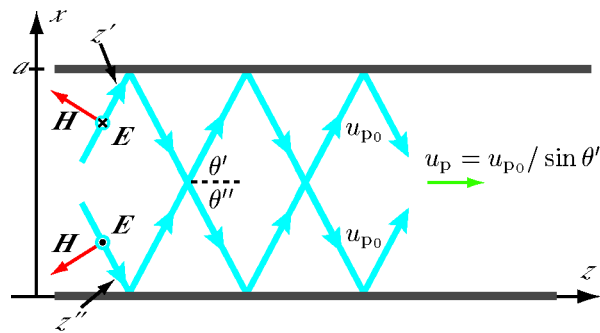
From Eq. (8.118a),  $z' = \frac{\pi x}{\beta a} + z$ .

Hence,  $\theta' = \tan^{-1}(\pi/\beta a)$ .

From Eq. (8.118b),  $z'' = -\frac{\pi x}{\beta a} + z$ .

Hence,  $\theta'' = -\tan^{-1}(\pi/\beta a)$ .

(a)  $z'$  and  $z''$  propagation directions



(b) TEM waves

**Figure 8-27:** The  $TE_{10}$  mode can be constructed as the sum of two TEM waves.



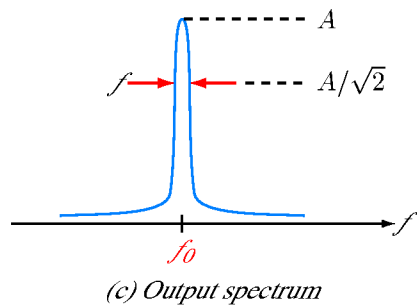
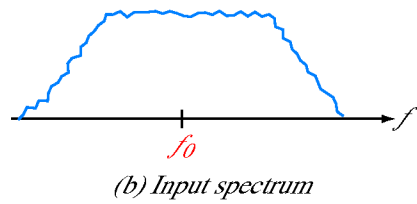
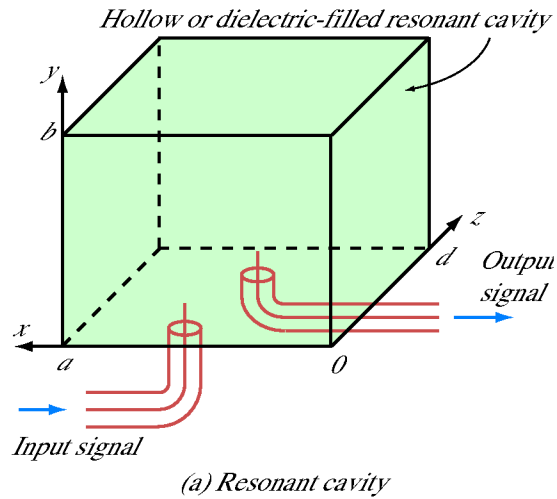


**Figure 8-28:** A resonant cavity supports a very narrow bandwidth around its resonant frequency  $f_0$ .

## Chapter 9 Figures

**Figure 9-1** Antenna as a transducer between a guided electromagnetic wave and a free-space wave, for both transmission and reception.

**Figure 9-2** Various types of antennas.

**Figure 9-3** Far-field plane-wave approximation.

**Figure 9-4** Short dipole placed at the origin of a spherical coordinate system.

**Figure 9-5** Spherical coordinate system.

**Figure 9-6** Electric field lines surrounding an oscillating dipole at a given instant.

**Figure 9-7** Radiation patterns of a short dipole.

**Figure 9-8** Definition of solid angle  $d\Omega = \sin \theta \, d\theta \, d\phi$ .

**Figure 9-9** Three-dimensional pattern of a narrow-beam antenna.

**Figure 9-10** Representative plots of the normalized radiation pattern of a microwave antenna in (a) polar form and (b) rectangular form.

**Figure 9-11** The pattern solid angle  $\Omega_p$  defines an equivalent cone over which all the radiation of the actual antenna is concentrated with uniform intensity equal to the maximum of the actual pattern.

**Figure 9-12** The solid angle of a unidirectional radiation pattern is approximately equal to the product of the half-power beamwidths in the two principal planes; that is,  $\Omega_p \simeq \beta_{xz}\beta_{yz}$ .

**Figure 9-13** Polar plot of  $F(\theta) = \cos^2 \theta$ .

**Figure 9-14** Center-fed half-wave dipole.

**Figure 9-15** A quarter-wave monopole above a conducting plane is equivalent to a full half-wave dipole in free space.

**Figure 9-16** Current distribution for three center-fed dipoles.

**Figure 9-17** Radiation patterns of dipoles with lengths of  $\lambda/2$ ,  $\lambda$ , and  $3\lambda/2$ .

**Figure 9-18** Receiving antenna represented by an equivalent circuit.

**Figure 9-19** Transmitter–receiver configuration.

**Figure 9-20** A horn antenna with aperture field distribution  $E_a(x_a, y_a)$ .

**Figure 9-21** Radiation by apertures: (a) an opening in an opaque screen illuminated by a light source through a collimating lens and (b) a parabolic dish reflector illuminated by a small horn antenna.

**Figure 9-22** Radiation by an aperture in the  $x_a$ – $y_a$  plane at  $z = 0$ .

**Figure 9-23** Normalized radiation pattern of a uniformly illuminated rectangular aperture in the  $x$ – $z$  plane ( $\phi = 0$ ).

**Figure 9-24** Radiation patterns of (a) a circular reflector and (b) a cylindrical reflector (side lobes not shown).

**Figure 9-25** The AN/FPS-85 Phased Array Radar Facility in the Florida panhandle, near the city of Freeport. A several-mile no-fly zone surrounds the radar installation as a safety concern for electroexplosive devices, such as ejection seats and munitions, carried on military aircraft.

**Figure 9-26** Linear-array configuration and geometry.

**Figure 9-27** The rays between the elements and a faraway observation point are approximately parallel lines. Hence, the distance  $R_i \simeq R_0 - id \cos \theta$ .

**Figure 9-28** Two half-wave dipole array of Example 9-5.

**Figure 9-29** (a) Two vertical dipoles separated by a distance  $d$  along the  $z$ -axis; (b) normalized array pattern in the  $y$ – $z$  plane for  $a_0 = a_1 = 1$ ,  $\psi_1 = \psi_0 = -\pi$ , and  $d = \lambda/2$ .

**Figure 9-30** Normalized array pattern of a uniformly excited six-element array with interelement spacing  $d = \lambda/2$ .

**Figure 9-31** Normalized array pattern of a two-element array with spacing  $d = 7\lambda/2$ .

**Figure 9-32** The application of linear phase.

**Figure 9-33** Normalized array pattern of a 10-element array with  $\lambda/2$  spacing between adjacent elements. All elements are excited with equal amplitude. Through the application of linear phase across the array, the main beam can be steered from the broadside direction ( $\theta_0 = 90^\circ$ ) to any scan angle  $\theta_0$ . Equiphase excitation corresponds to  $\theta_0 = 90^\circ$ .

**Figure 9-34** An example of a feeding arrangement for frequency-scanned arrays.

**Figure 9-35** Steerable six-element array (Example 9-8).

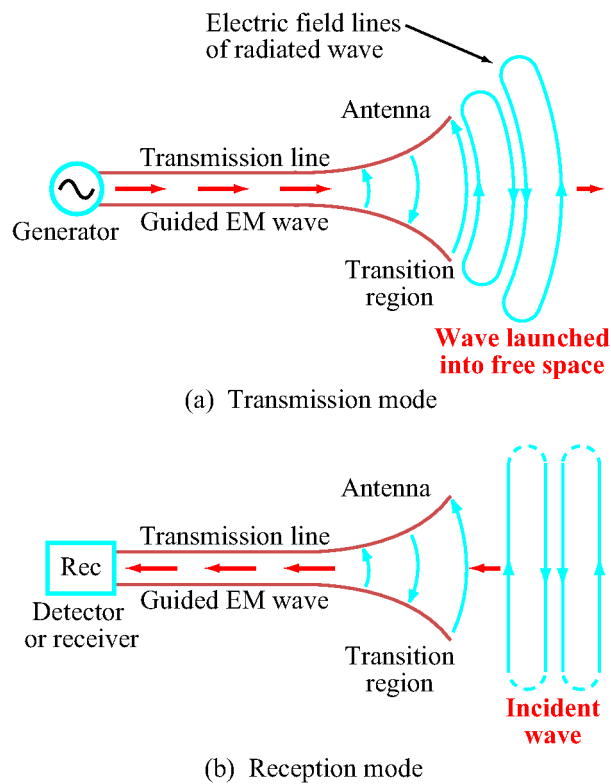


**Figure 9-1:** Antenna as a transducer between a guided electromagnetic wave and a free-space wave, for both transmission and reception.

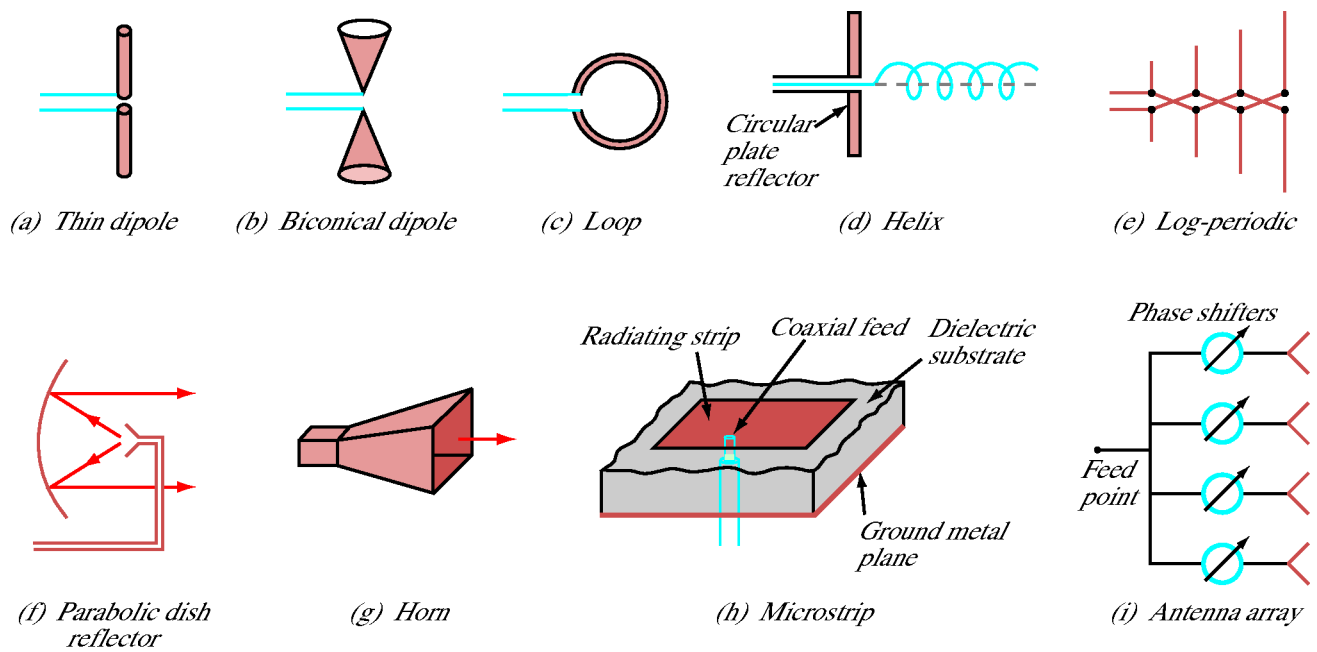


**Figure 9-2:** Various types of antennas.

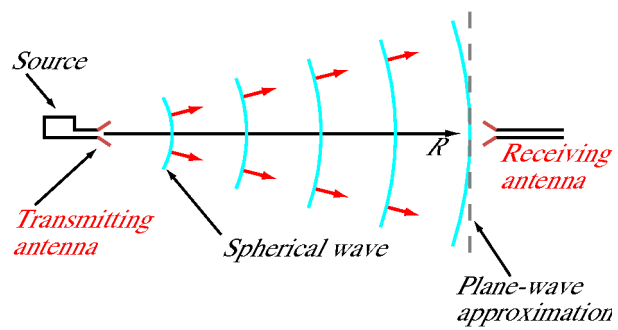


**Figure 9-3:** Far-field plane-wave approximation.

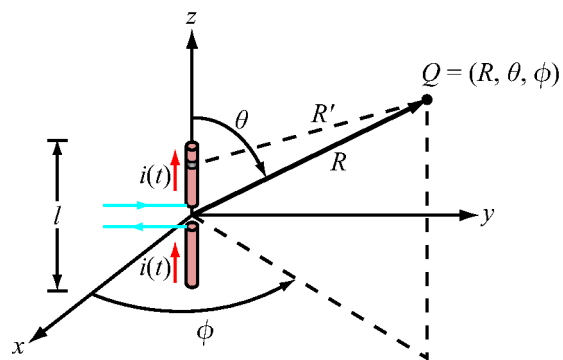


**Figure 9-4:** Short dipole placed at the origin of a spherical coordinate system.



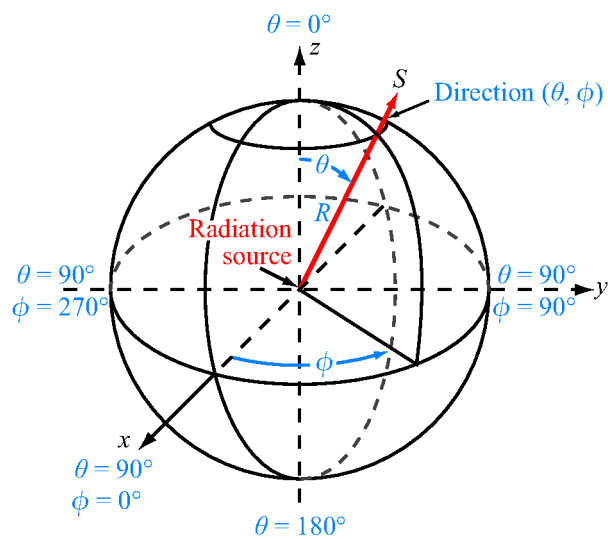


**Figure 9-5:** Spherical coordinate system.

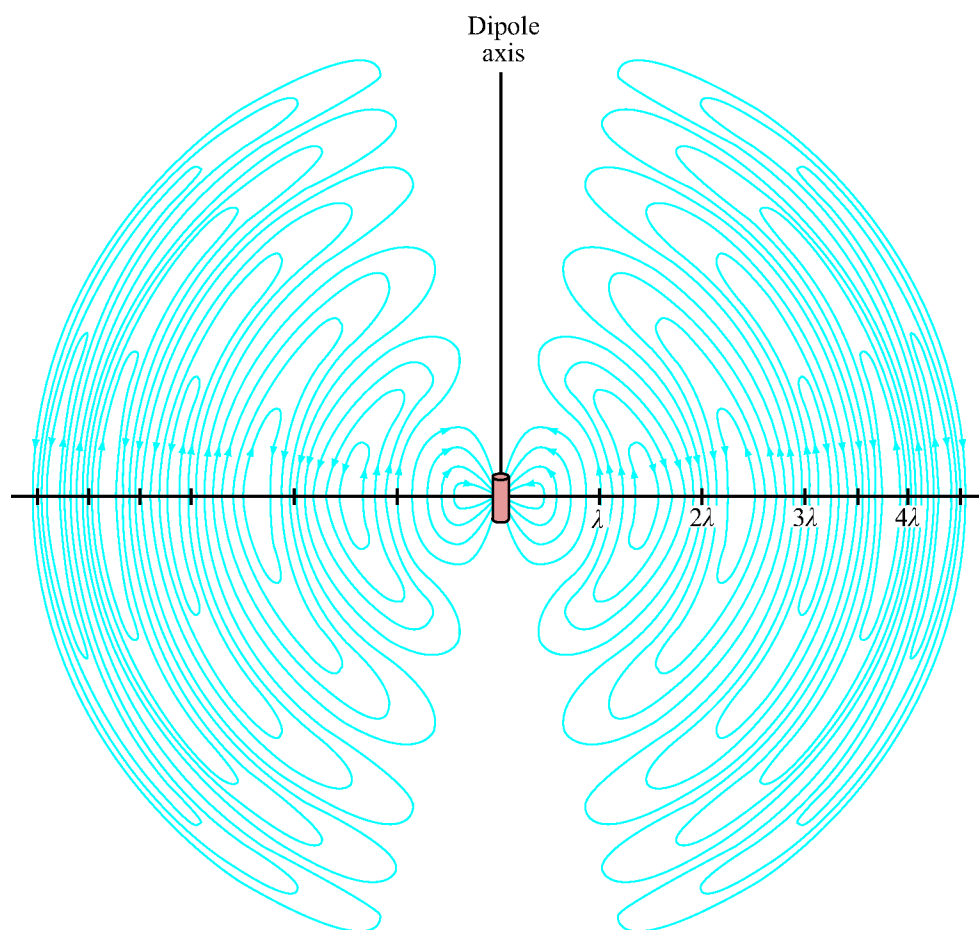


**Figure 9-6:** Electric field lines surrounding an oscillating dipole at a given instant.

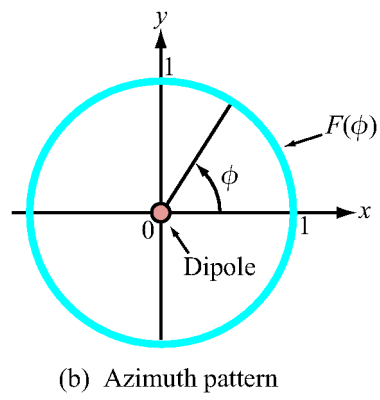
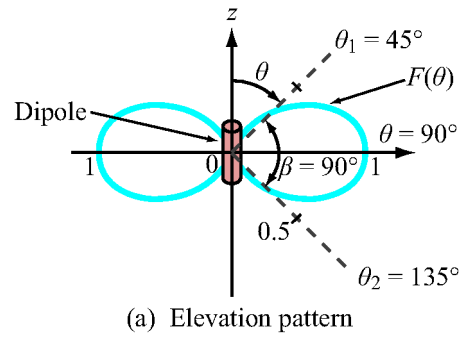


**Figure 9-7:** Radiation patterns of a short dipole.

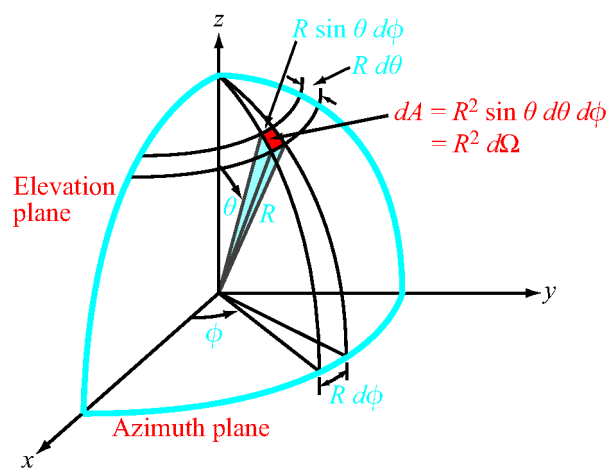


**Figure 9-8:** Definition of solid angle  $d\Omega = \sin \theta d\theta d\phi$ .

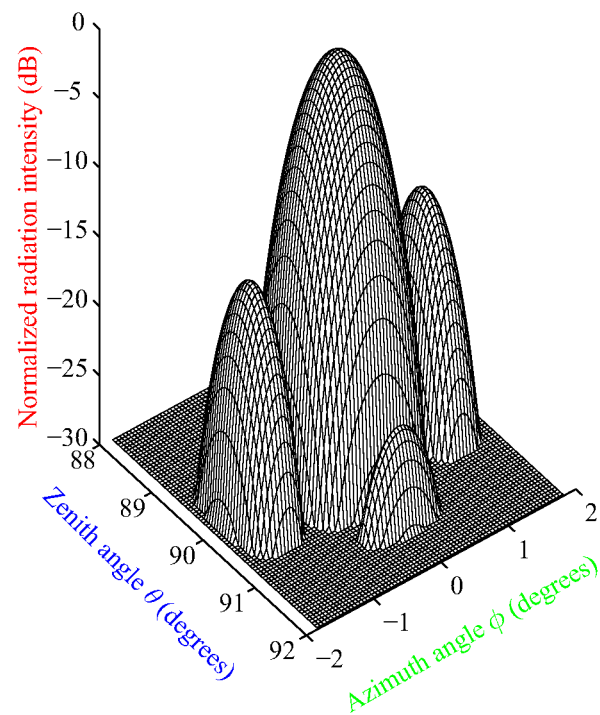
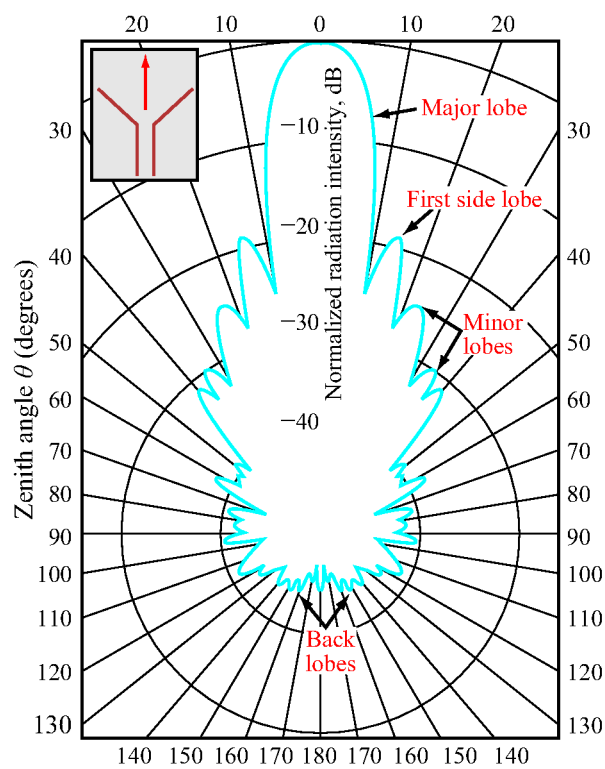
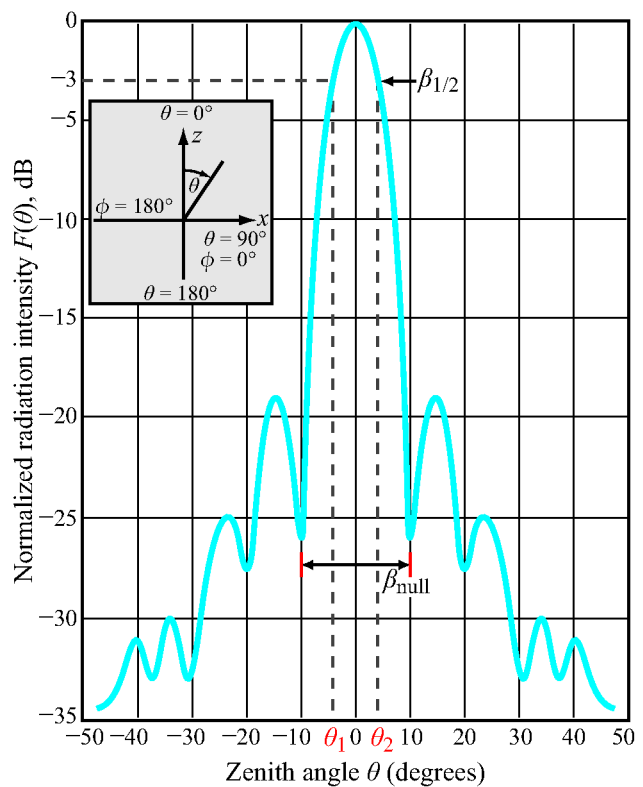


**Figure 9-9:** Three-dimensional pattern of a narrow-beam antenna.



(a) Polar diagram



(b) Rectangular plot

**Figure 9-10:** Representative plots of the normalized radiation pattern of a microwave antenna in (a) polar form and (b) rectangular form.

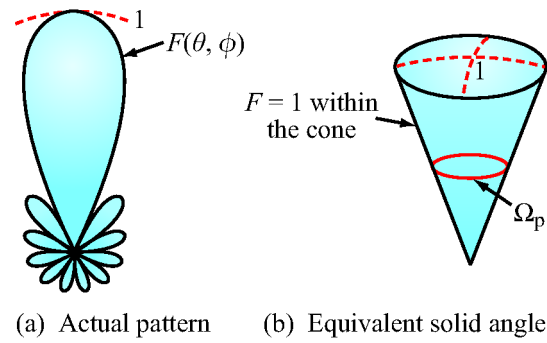


**Figure 9-11:** The pattern solid angle  $\Omega_p$  defines an equivalent cone over which all the radiation of the actual antenna is concentrated with uniform intensity equal to the maximum of the actual pattern.

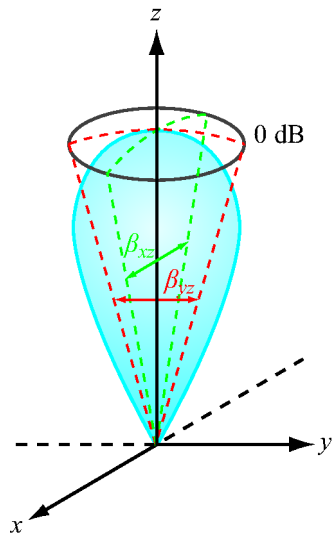


**Figure 9-12:** The solid angle of a unidirectional radiation pattern is approximately equal to the product of the half-power beamwidths in the two principal planes; that is,  $\Omega_p \simeq \beta_{xz}\beta_{yz}$ .



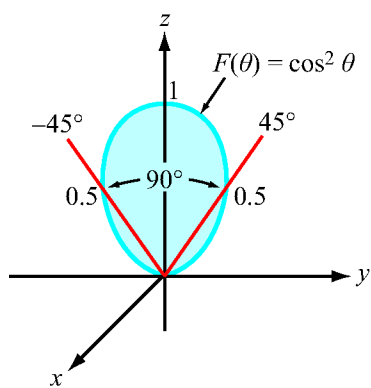


**Figure 9-13:** Polar plot of  $F(\theta) = \cos^2 \theta$ .

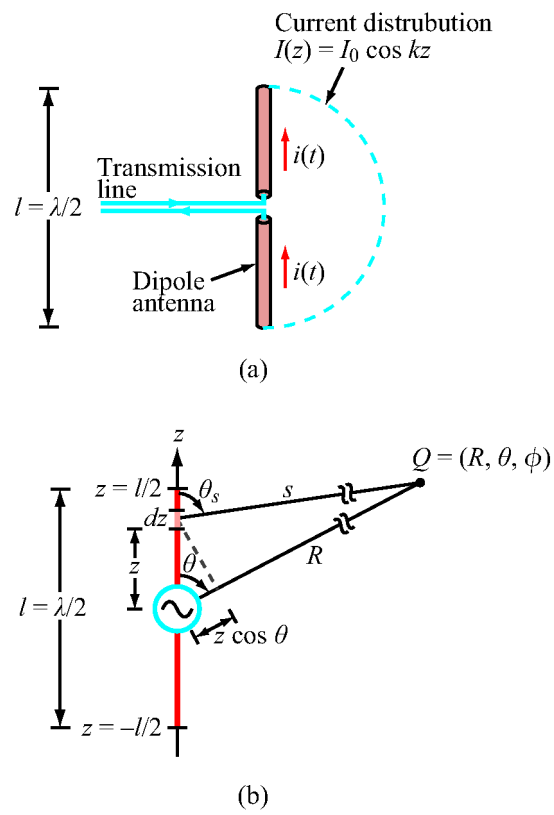


**Figure 9-14:** Center-fed half-wave dipole.

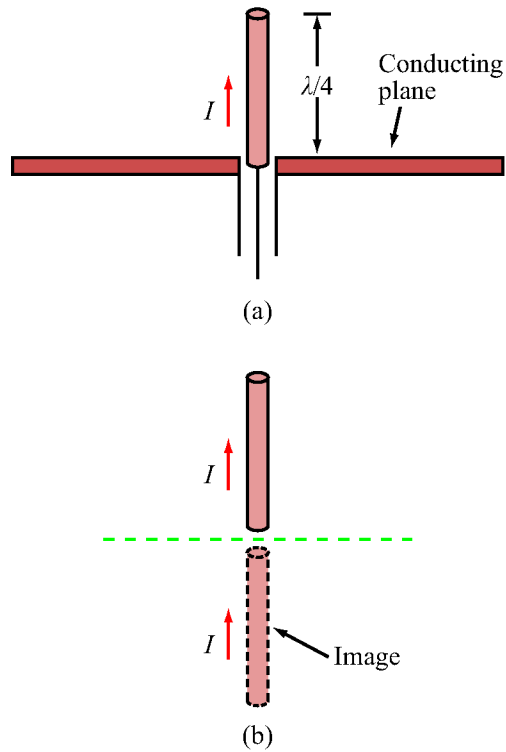


**Figure 9-15:** A quarter-wave monopole above a conducting plane is equivalent to a full half-wave dipole in free space.

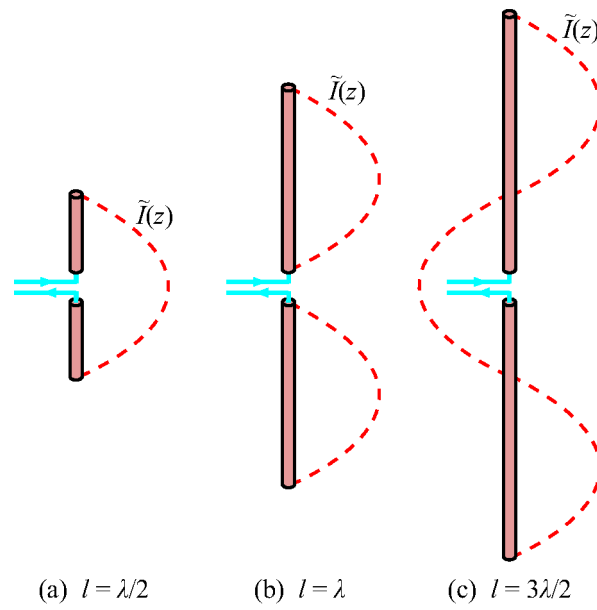
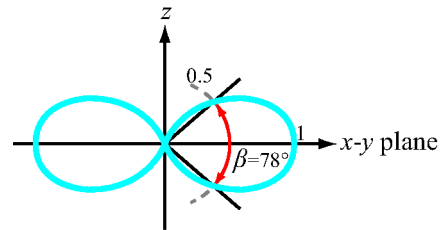
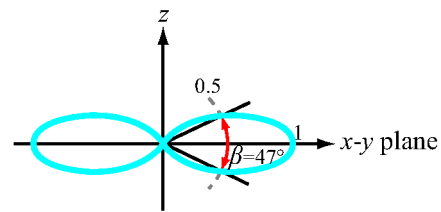


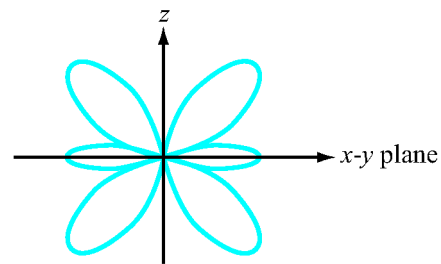
**Figure 9-16:** Current distribution for three center-fed dipoles.



(a)  $l = \lambda/2$



(b)  $l = \lambda$



(c)  $l = 3\lambda/2$

**Figure 9-17:** Radiation patterns of dipoles with lengths of  $\lambda/2$ ,  $\lambda$ , and  $3\lambda/2$ .

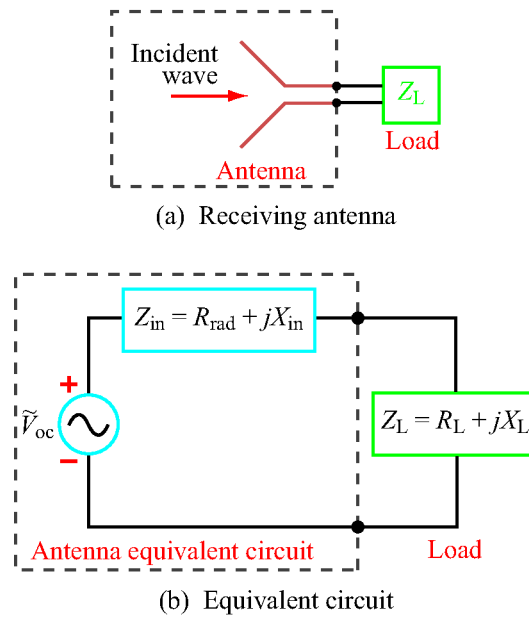


**Figure 9-18:** Receiving antenna represented by an equivalent circuit.

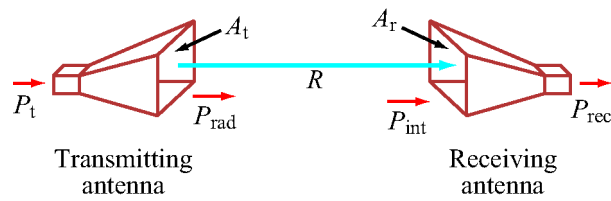


**Figure 9-19:** Transmitter–receiver configuration.

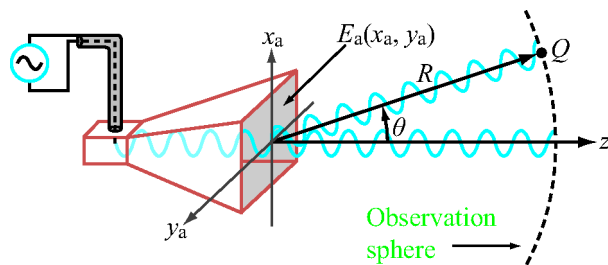
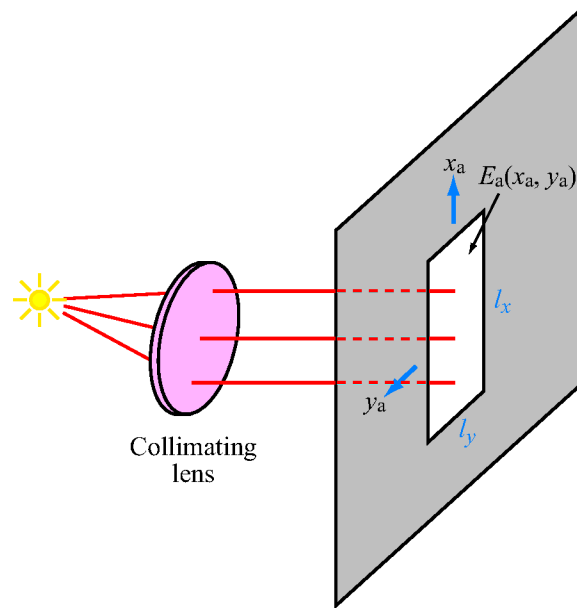
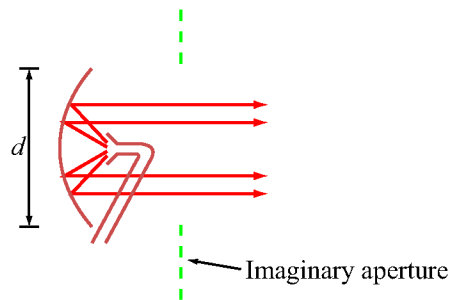


**Figure 9-20:** A horn antenna with aperture field distribution  $E_a(x_a, y_a)$ .





(a) Opening in an opaque screen



(b) Parabolic reflector antenna

**Figure 9-21:** Radiation by apertures: (a) an opening in an opaque screen illuminated by a light source through a collimating lens and (b) a parabolic dish reflector illuminated by a small horn antenna.

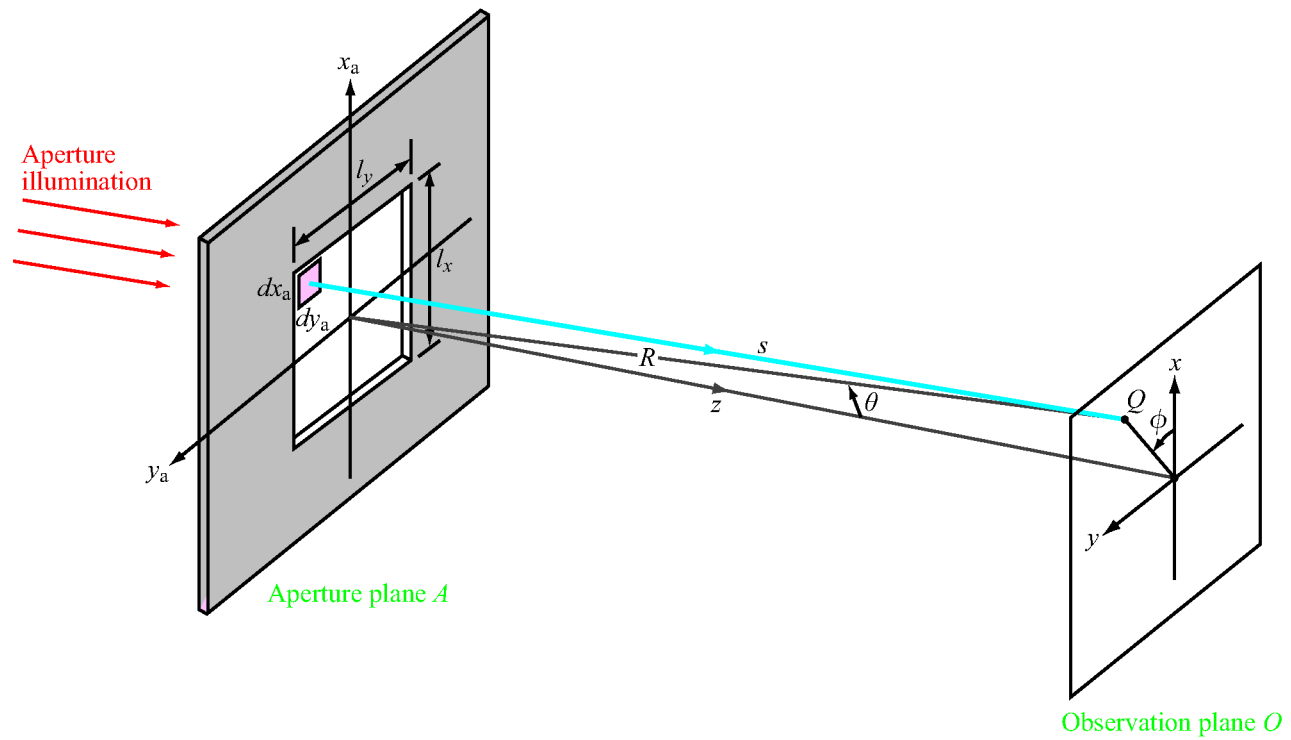


**Figure 9-22:** Radiation by an aperture in the  $x_a$ - $y_a$  plane at  $z=0$ .

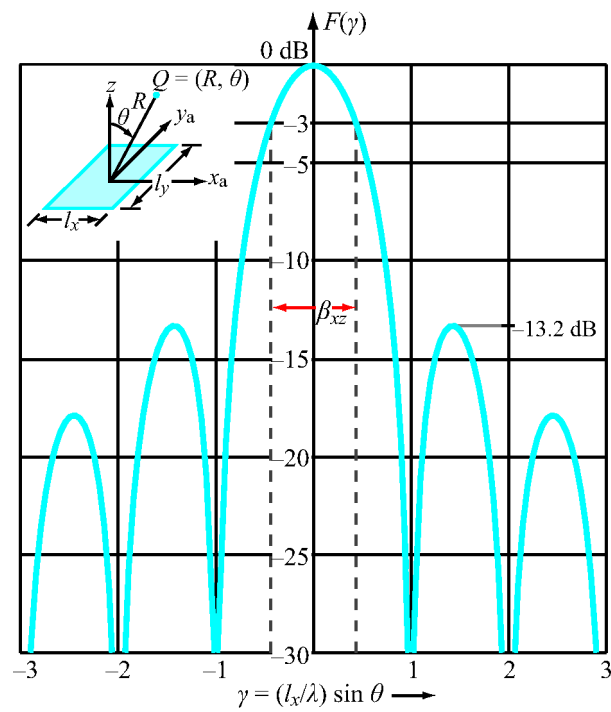
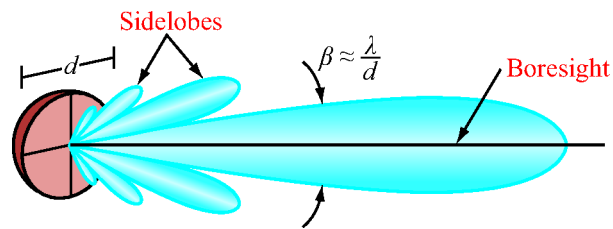
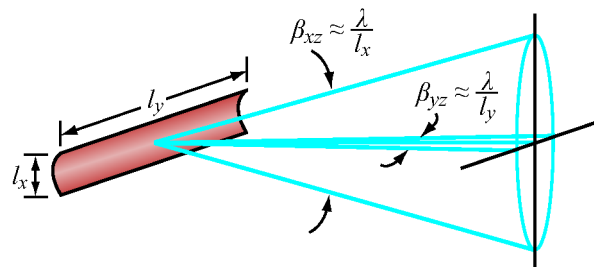


**Figure 9-23:** Normalized radiation pattern of a uniformly illuminated rectangular aperture in the  $x$ - $z$  plane ( $\phi = 0$ ).



(a) Pencil beam

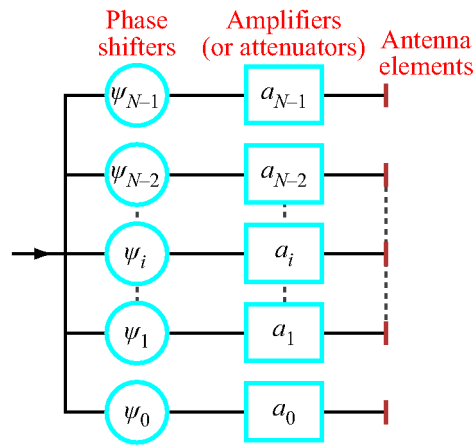


(b) Fan beam

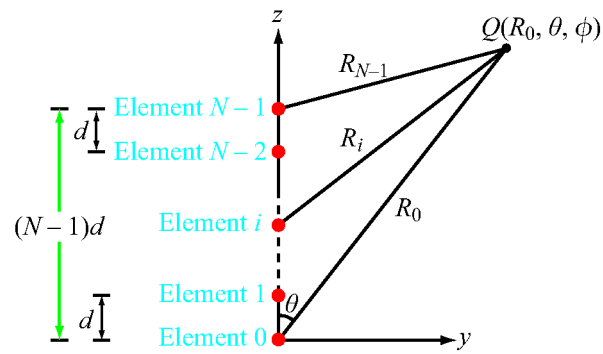
**Figure 9-24:** Radiation patterns of (a) a circular reflector and (b) a cylindrical reflector (side lobes not shown).



**Figure 9-25:** The AN/FPS-85 Phased Array Radar Facility in the Florida panhandle, near the city of Freeport. A several-mile no-fly zone surrounds the radar installation as a safety concern for electroexplosive devices, such as ejection seats and munitions, carried on military aircraft.



(a) Array elements with individual amplitude and phase control



(b) Array geometry relative to observation point

**Figure 9-26:** Linear-array configuration and geometry.

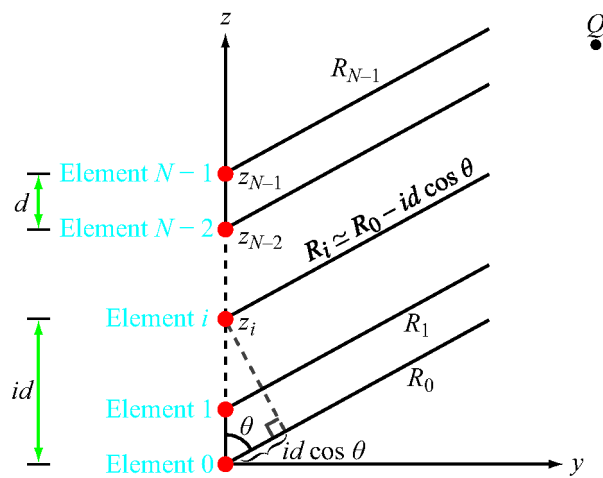


**Figure 9-27:** The rays between the elements and a faraway observation point are approximately parallel lines. Hence, the distance  $R_i \simeq R_0 - id \cos \theta$ .

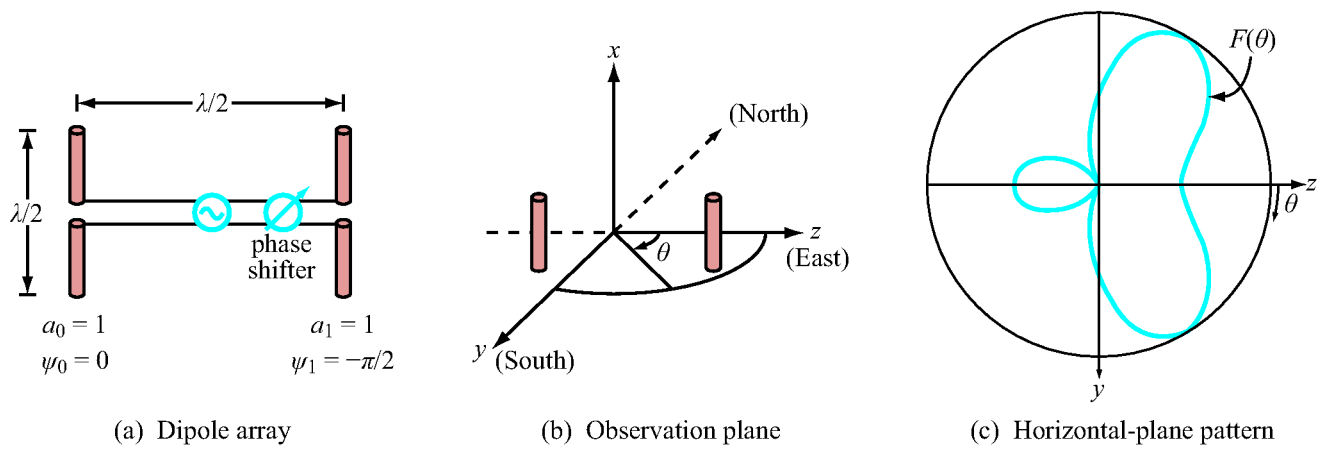
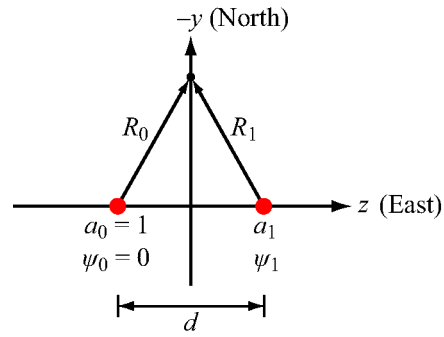
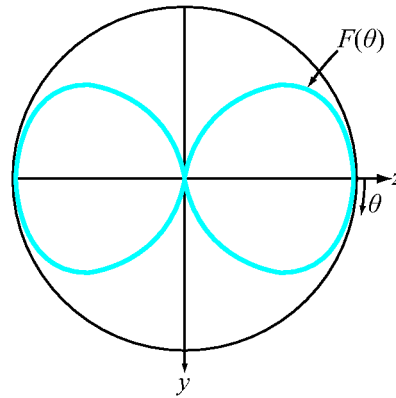


**Figure 9-28:** Two half-wave dipole array of Example 9-5.





(a) Array arrangement



(b) Array pattern

**Figure 9-29:** (a) Two vertical dipoles separated by a distance  $d$  along the  $z$ -axis; (b) normalized array pattern in the  $y$ - $z$  plane for  $a_0 = a_1 = 1$ ,  $\psi_1 = \psi_0 = -\pi$ , and  $d = \lambda/2$ .

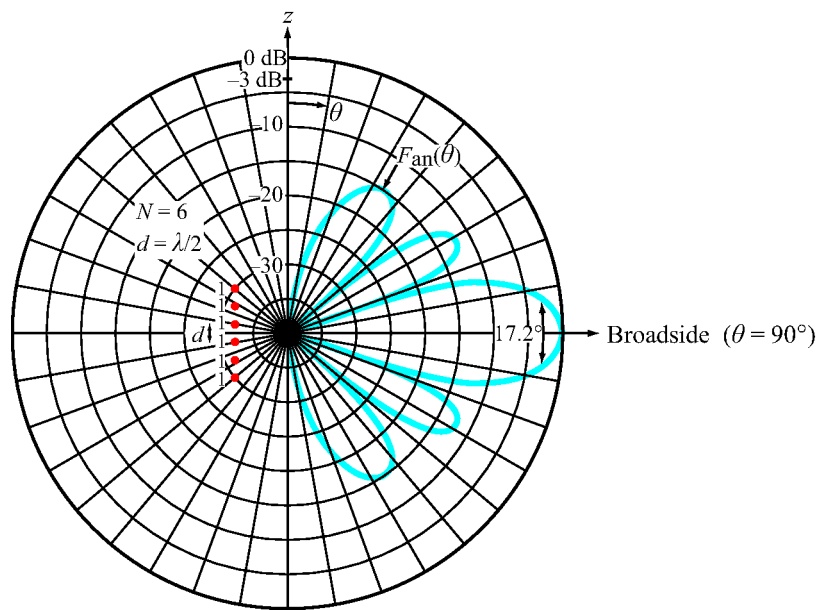


**Figure 9-30:** Normalized array pattern of a uniformly excited six-element array with interelement spacing  $d = \lambda/2$ .

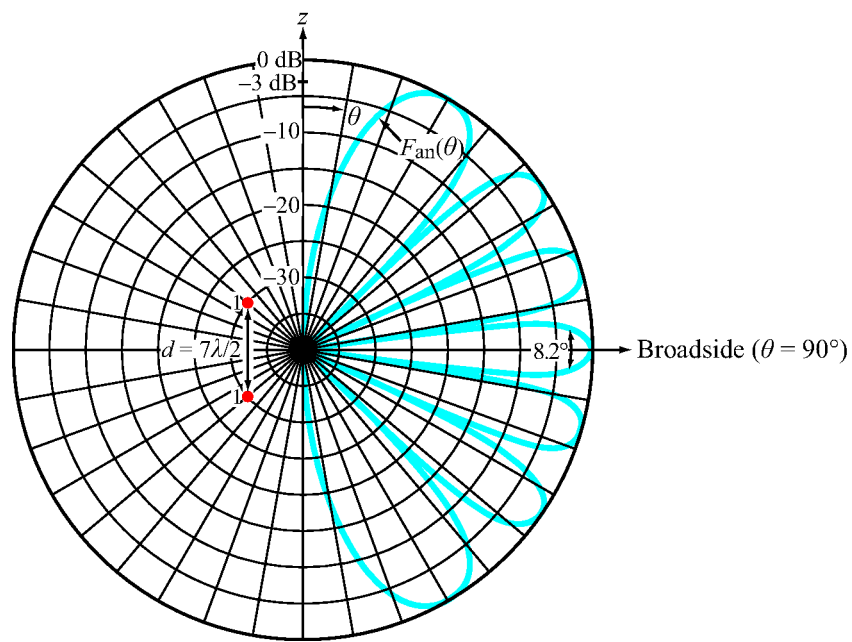


**Figure 9-31:** Normalized array pattern of a two-element array with spacing  $d = 7\lambda/2$ .

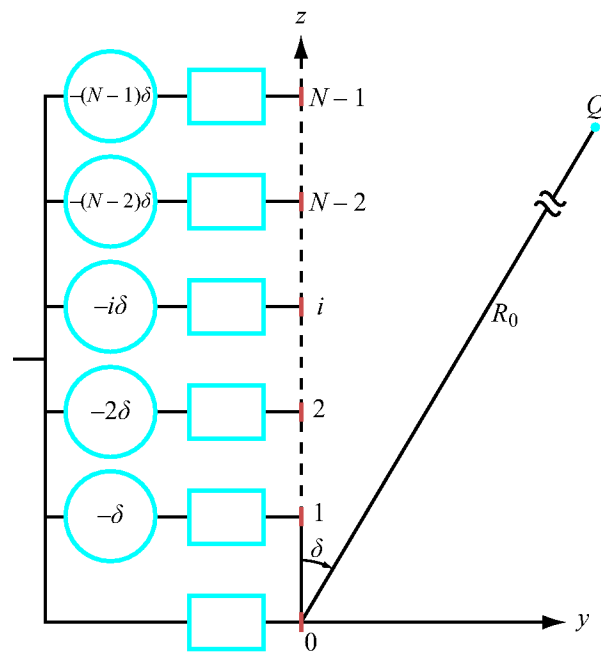


**Figure 9-32:** The application of linear phase.

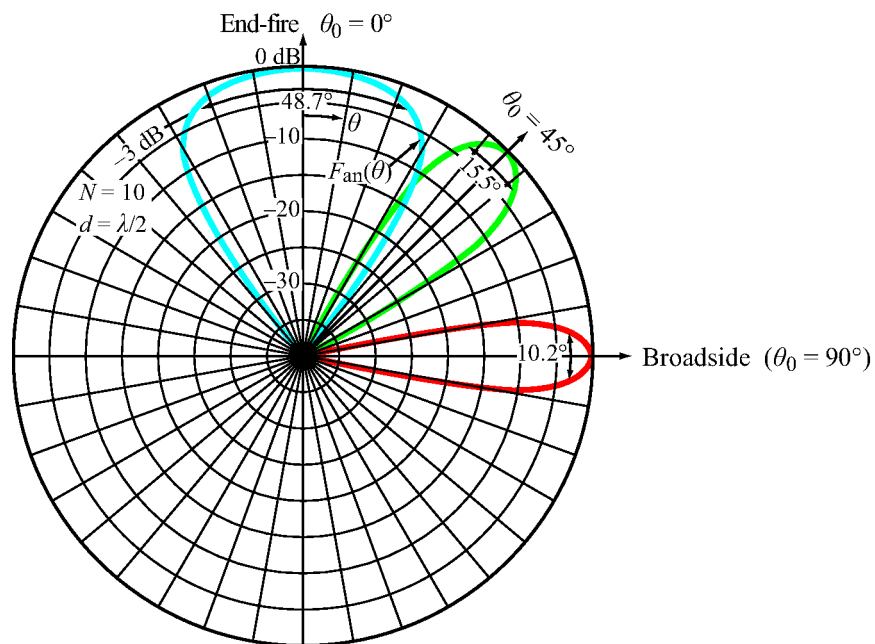


**Figure 9-33:** Normalized array pattern of a 10-element array with  $\lambda/2$  spacing between adjacent elements. All elements are excited with equal amplitude. Through the application of linear phase across the array, the main beam can be steered from the broadside direction ( $\theta_0 = 90^\circ$ ) to any scan angle  $\theta_0$ . Equiphasic excitation corresponds to  $\theta_0 = 90^\circ$ .

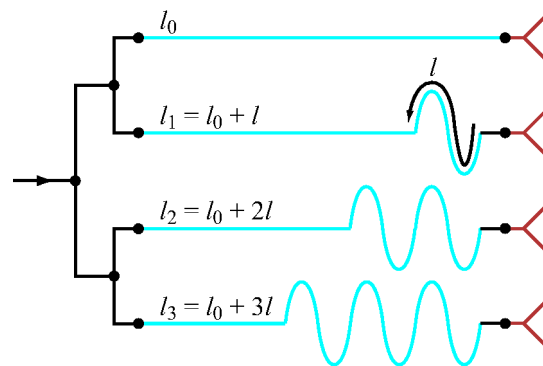


**Figure 9-34:** An example of a feeding arrangement for frequency-scanned arrays.

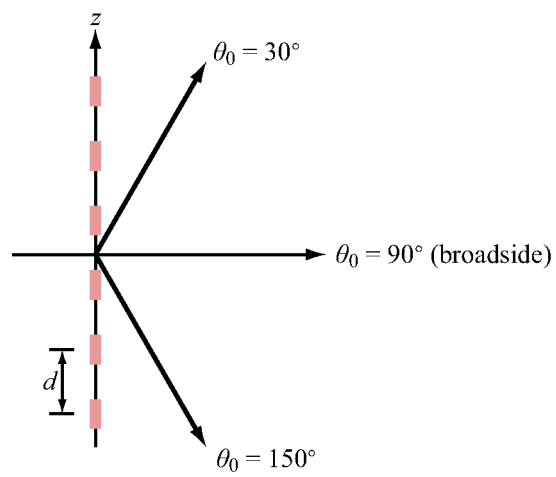


**Figure 9-35:** Steerable six-element array (Example 9-8).

## Chapter 10 Figures

**Figure 10-1** Elements of a satellite communication network.

**Figure 10-2** Orbits of geostationary satellites.

**Figure 10-3** Satellite of mass  $m_s$  in orbit around Earth. For the orbit to be geostationary, the distance  $R_0$  between the satellite and Earth's center should be 42,164 km. At the equator, this corresponds to an altitude of 35,786 km above Earth's surface.

**Figure 10-4** Elements of a 12-channel (transponder) communications system.

**Figure 10-5** Basic operation of a ferrite circulator.

**Figure 10-6** Polarization diversity is used to increase the number of channels from 12 to 24.

**Figure 10-7** Satellite transponder.

**Figure 10-8** Spot and multi-beam satellite antenna systems for coverage of defined areas on Earth's surface.

**Figure 10-9** Basic block diagram of a radar system.

**Figure 10-10** A pulse radar transmits a continuous train of RF pulses at a repetition frequency  $f_p$ .

**Figure 10-11** Radar beam viewing two targets at ranges  $R_1$  and  $R_2$ .

**Figure 10-12** The azimuth resolution  $\Delta x$  at a range  $R$  is equal to  $\beta R$ .

**Figure 10-13** The output of a radar receiver as a function of time.

**Figure 10-14** Bistatic radar system viewing a target with radar cross section (RCS)  $\sigma_t$ .

**Figure 10-15** A wave radiated from a point source when (a) stationary and (b) moving. The wave is compressed in the direction of motion, spread out in the opposite direction, and unaffected in the direction normal to motion.

**Figure 10-16** Transmitter with radial velocity  $u_r$  approaching a stationary receiver.

**Figure 10-17** The Doppler frequency shift is negative for a receding target ( $0 \leq \theta \leq 90^\circ$ ), as in (a), and positive for an approaching target ( $90^\circ \leq \theta \leq 180^\circ$ ), as in (b).



**Figure 10-18** Antenna feeding arrangement for an amplitude-comparison monopulse radar: (a) feed horns and (b) connection to phasing network.

**Figure 10-19** A target observed by two overlapping beams of a monopulse radar.

**Figure 10-20** Functionality of the phasing network in (a) the transmit mode and (b) the receive mode for the elevation-difference channel.

**Figure 10-21** Monopulse antenna (a) sum pattern, (b) elevation-difference pattern, and (c) angle error signal.

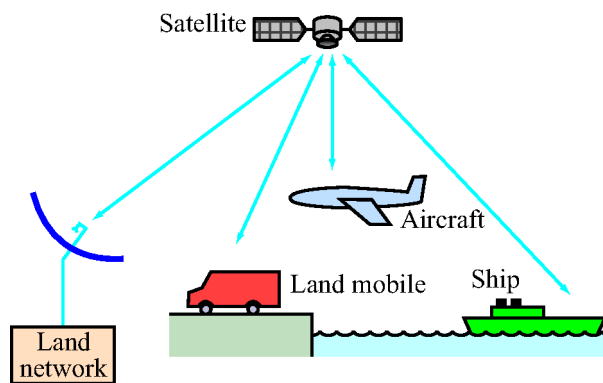
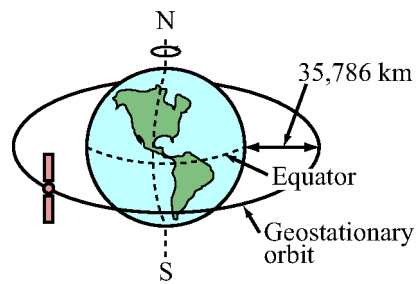
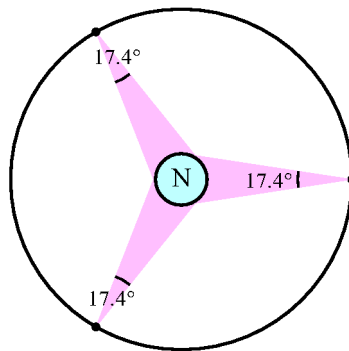


**Figure 10-1:** Elements of a satellite communication network.



(a) Geostationary satellite orbit



(b) Worldwide coverage by three satellites spaced 120° apart

**Figure 10-2:** Orbits of geostationary satellites.

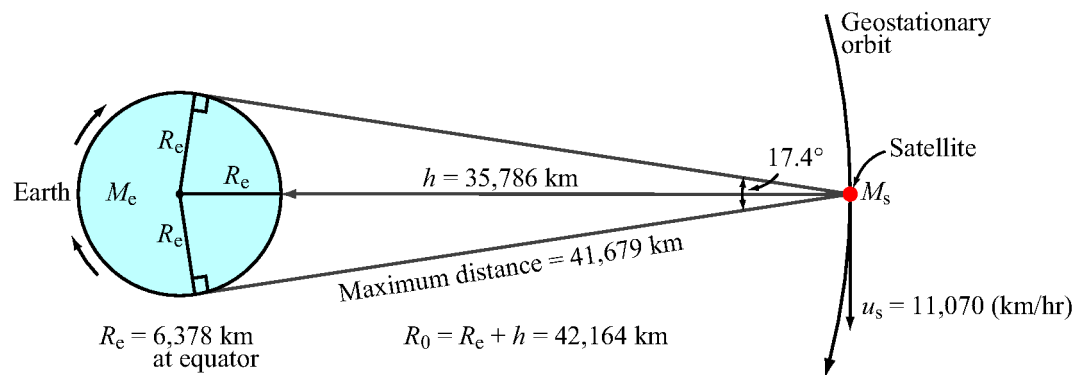


**Figure 10-3:** Satellite of mass  $m_s$  in orbit around Earth. For the orbit to be geostationary, the distance  $R_0$  between the satellite and Earth's center should be 42,164 km. At the equator, this corresponds to an altitude of 35,786 km above Earth's surface.

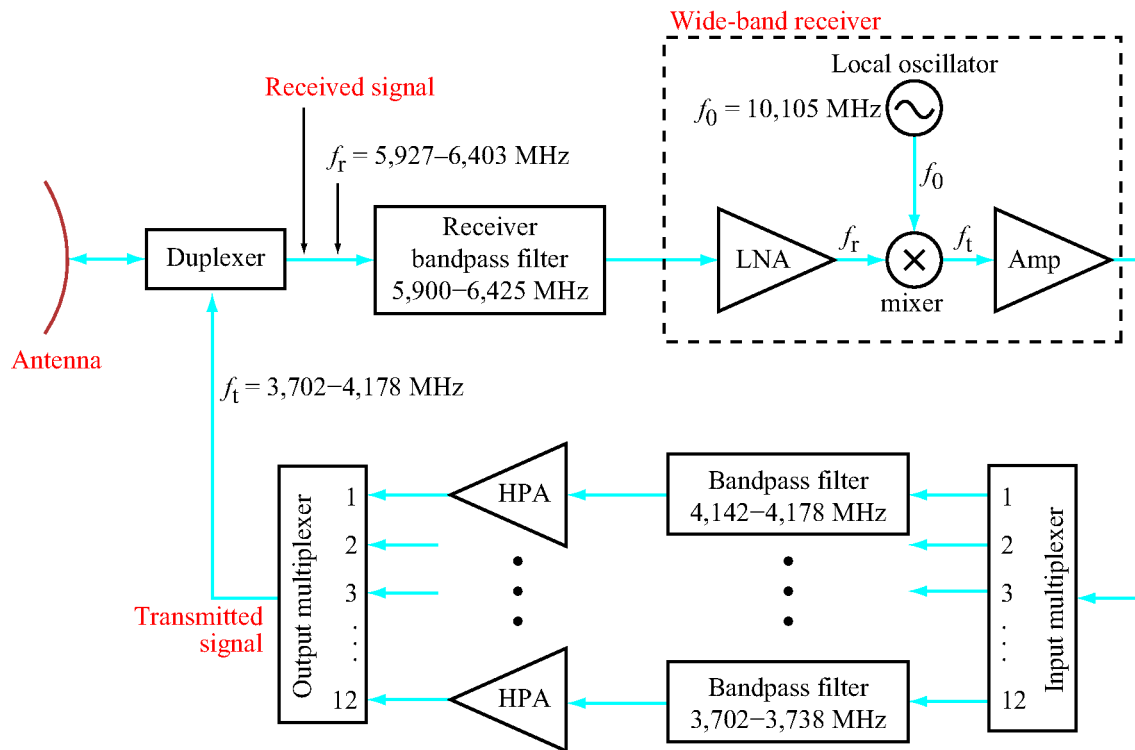


**Figure 10-4:** Elements of a 12-channel (transponder) communications system.

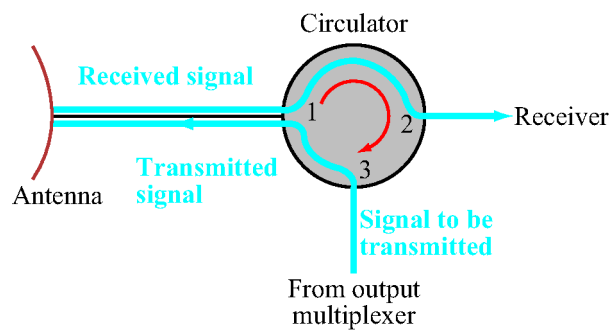


**Figure 10-5:** Basic operation of a ferrite circulator.

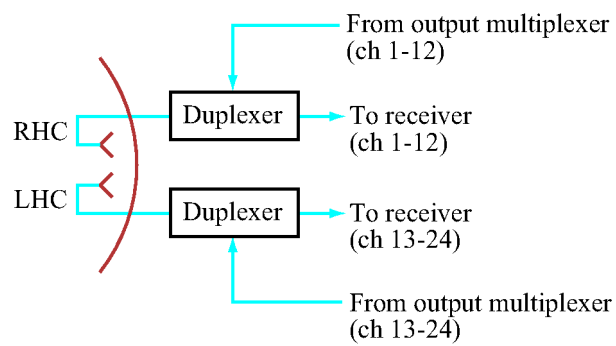


**Figure 10-6:** Polarization diversity is used to increase the number of channels from 12 to 24.

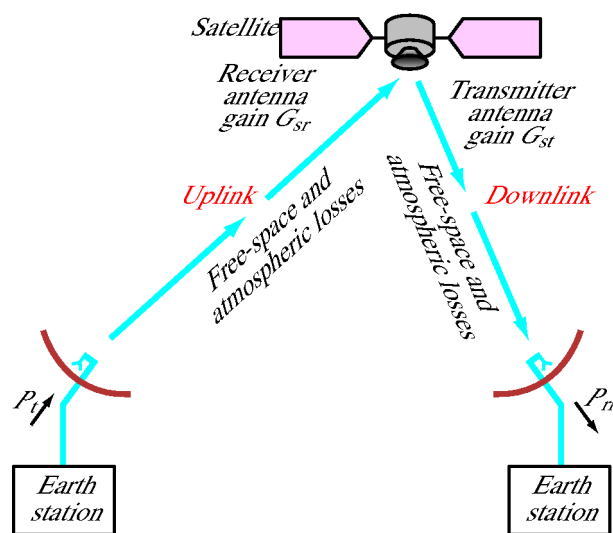


**Figure 10-7:** Satellite transponder.



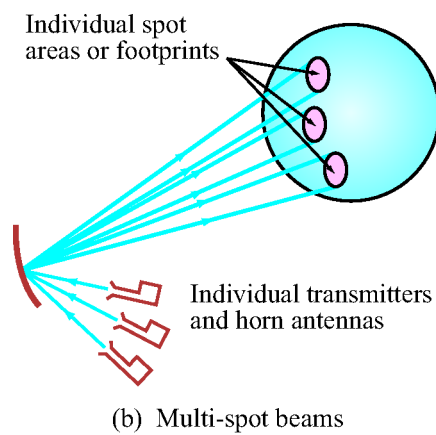
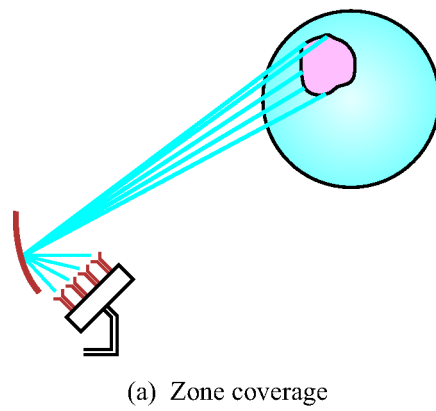


**Figure 10-8:** Spot and multi-beam satellite antenna systems for coverage of defined areas on Earth's surface.

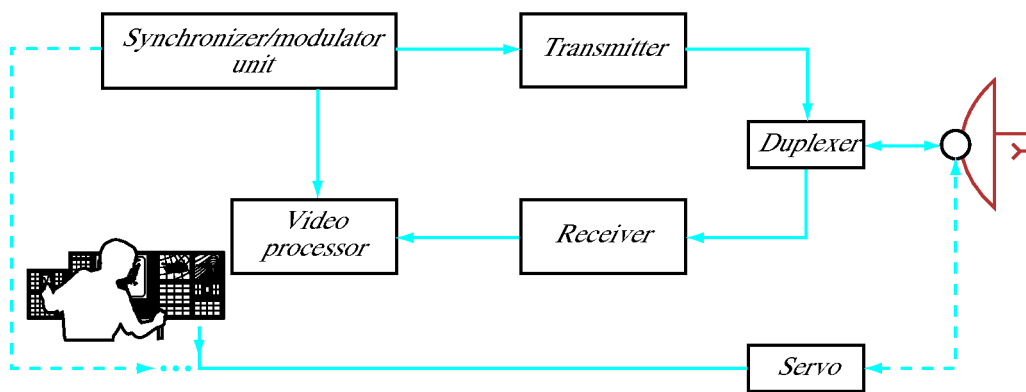


**Figure 10-9:** Basic block diagram of a radar system.

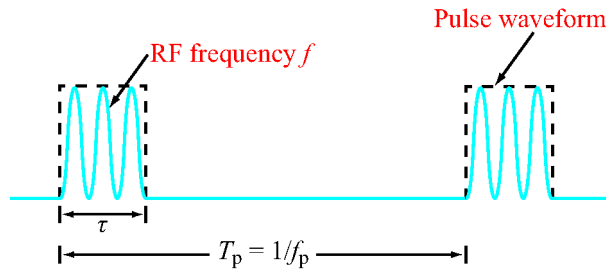


**Figure 10-10:** A pulse radar transmits a continuous train of RF pulses at a repetition frequency  $f_p$ .

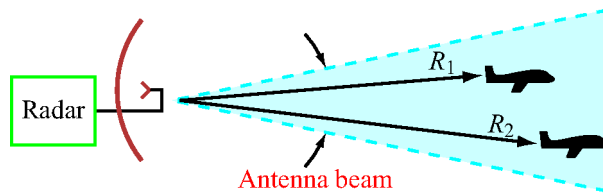


**Figure 10-11:** Radar beam viewing two targets at ranges  $R_1$  and  $R_2$ .

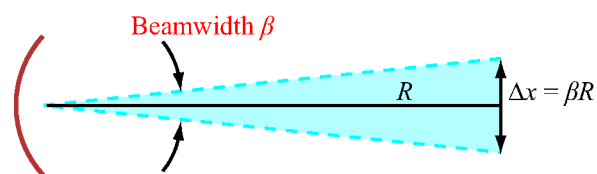


**Figure 10-12:** The azimuth resolution  $\Delta x$  at a range  $R$  is equal to  $\beta R$ .

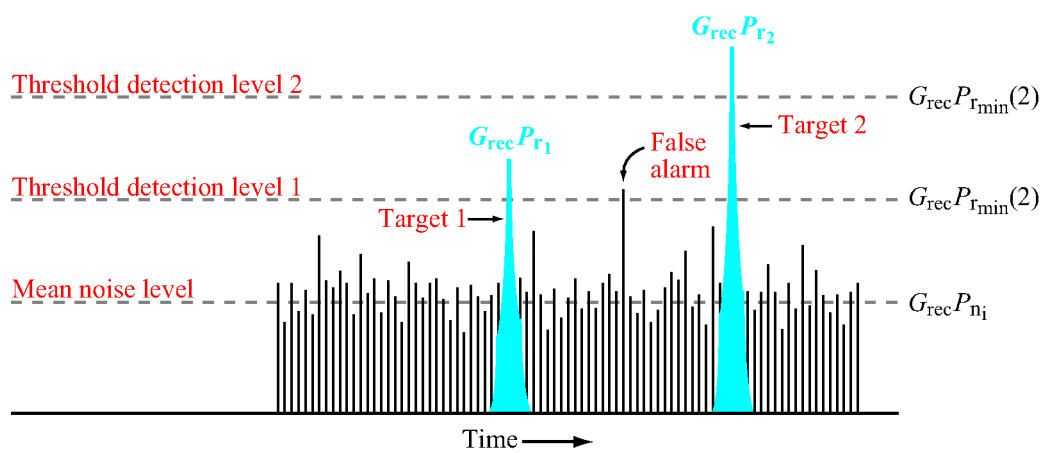


**Figure 10-13:** The output of a radar receiver as a function of time.

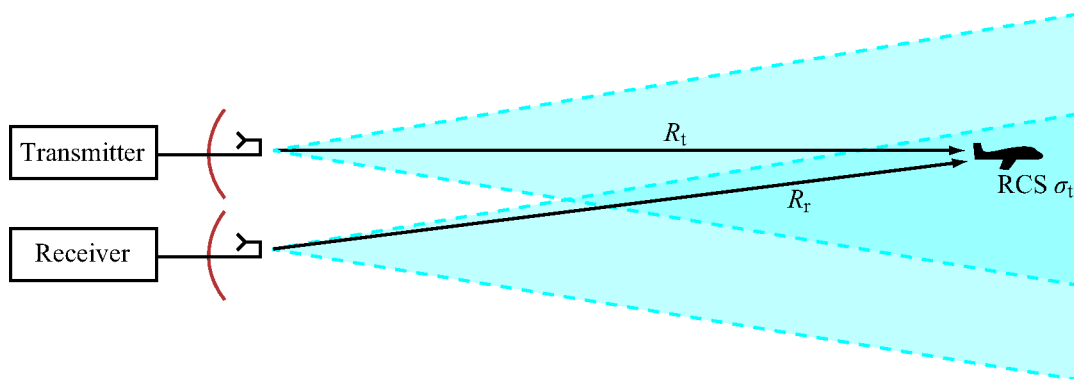
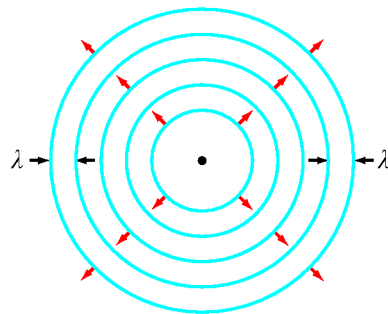
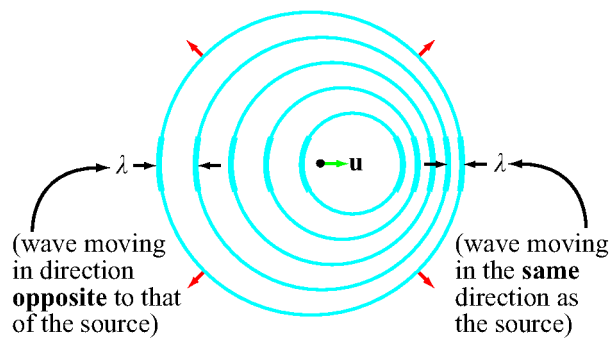


**Figure 10-14:** Bistatic radar system viewing a target with radar cross section (RCS)  $\sigma_t$ .



(a) Stationary source



(b) Moving source

**Figure 10-15:** A wave radiated from a point source when (a) stationary and (b) moving. The wave is compressed in the direction of motion, spread out in the opposite direction, and unaffected in the direction normal to motion.



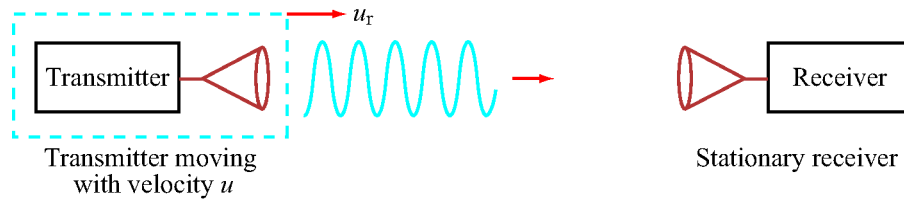


**Figure 10-16:** Transmitter with radial velocity  $u_r$  approaching a stationary receiver.

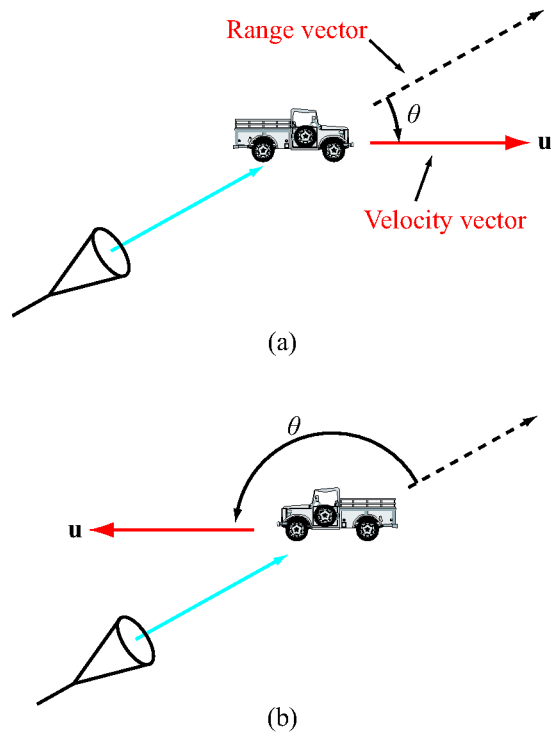


**Figure 10-17:** The Doppler frequency shift is negative for a receding target ( $0 \leq \theta \leq 90^\circ$ ), as in (a), and positive for an approaching target ( $90^\circ \leq \theta \leq 180^\circ$ ), as in (b).

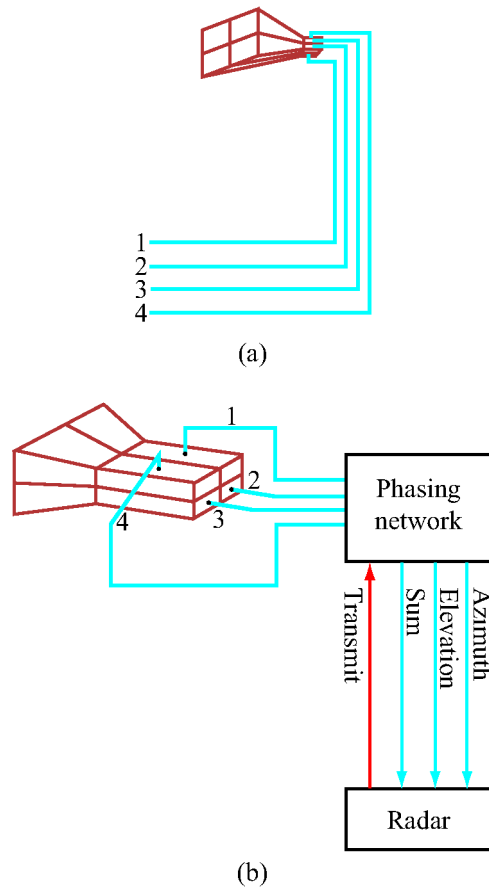


**Figure 10-18:** Antenna feeding arrangement for an amplitude-comparison monopulse radar: (a) feed horns and (b) connection to phasing network.

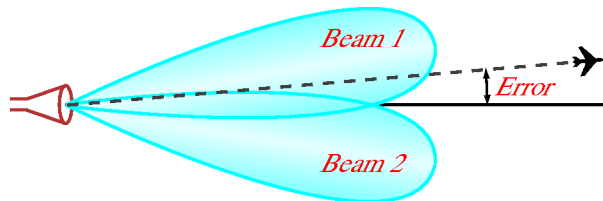


**Figure 10-19:** A target observed by two overlapping beams of a monopulse radar.

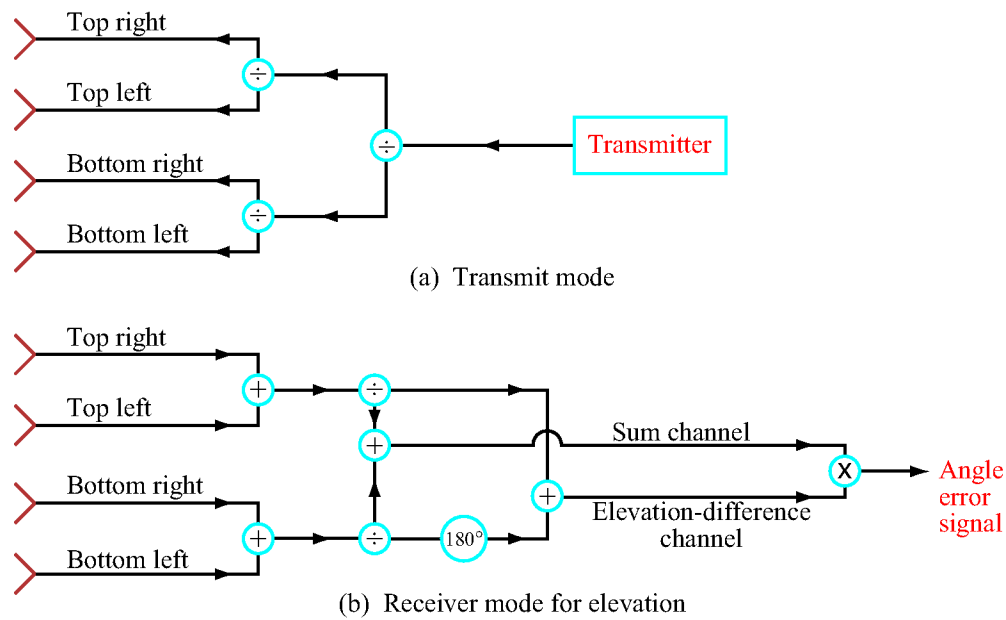
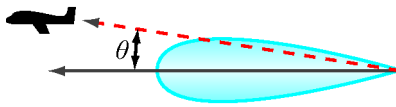
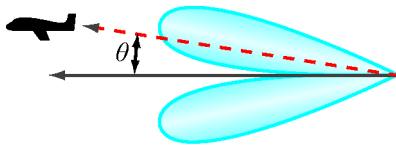


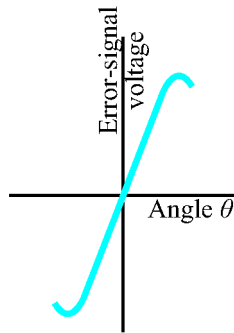
**Figure 10-20:** Functionality of the phasing network in (a) the transmit mode and (b) the receive mode for the elevation-difference channel.



(a) Sum pattern



(b) Elevation-difference pattern



(c) Angle error signal

**Figure 10-21:** Monopulse antenna (a) sum pattern, (b) elevation-difference pattern, and (c) angle error signal.